UNIVERSITÉ DU LUXEMBOURG

PhD-FSTM-2023-121
The Faculty of Science, Technology and Medicine

DISSERTATION

Defence held on 02/10/2023 in Esch-sur-Alzette

to obtain the degree of

DOCTEUR DE L'UNIVERSITÉ DU LUXEMBOURG

EN *PHYSIQUE*

by

Poorani GNANASAMBANDAN
Born on 7th April 1991 in Sivagangai, India

HIGH PERFORMANCE TRANSPARENT CONDUCTING MATERIALS FOR SOLAR CELLS

Dissertation defence committee

Dr. Renaud Leturcq, dissertation supervisor
Luxembourg Institute of Science and Technology

Dr. Susanne Siebentritt, Chairman
Professor, Université du Luxembourg

Dr. David Muñoz-Rojas
Laboratoire des Matériaux et du Génie Physique, INP-CNRS, Université Grenoble Alpes

Dr. Jérôme Polesel
Luxembourg Institute of Science and Technology

Dr. Julien Bachmann
Professor, Friedrich-Alexander-Universität Erlangen-Nürnberg

Affidavit

I hereby confirm that the Ph.D. thesis entitled *"Highly transparent conducting materials for solar cells"* has been written independently and without any other sources than cited.

Luxembourg, _____ _____

Name

Abstract

Atomic layer deposition (ALD) has been widely used for the development of buffer layers on copper-indium-gallium-sulfide and copper-indium-gallium-selenide solar cells with appropriate electronic properties; however, still an in-depth understanding of the growth properties of the ternary oxide and their related properties is lacking. In this thesis, we investigate the interface chemistry and mixing of binary ALD processes on the growth and resulting optoelectronic properties by altering the supercycle process parameters (pulse ratio and bilayer period) of the ternary ALD process for zinc magnesium oxide(ZMO) and zinc tin oxide (ZTO). We show that the interplay between ZnO and MgO interfaces in the synthesis of ZMO leads to enhanced growth of the MgO layer by the ZnO surface. Similarly, we validate the inhibited growth of ZnO by SnO_x surface in ALD deposited ZTO films. We propose probing the effect of the bilayer period in growth of ternary oxides by ALD can serve as an effective alternative to QCM in understanding the growth kinetics which can be extended to many other materials.

We show that the optical properties of the ternary films not only depend on the composition but also depend on the bilayer period at a given composition. More specifically, the bandgap at a given composition for both ZMO and ZTO films is high at the smallest bilayer period and starts decreasing with increase in bilayer period, reaching the bandgap value of ZnO for bilayer periods greater than 40. We explore the possible mechanisms for the change in optical properties with bilayer period. We propose bilayer period as an effective parameter alongside composition to tune the bandgap and demonstrate the application of which by depositing ALD grown ZMO buffer layers for chalcopyrite solar cells.

To my grandmothers

Pooranam
(1929-2021)
Krishnammal
(1942-2023)

Popular Science Summary

This thesis deals with transparent conducting materials. Typically, optical transparency and electrical conductivity do not coexist and are contradicting properties by nature. Glass is transparent but it is electrically insulating, while metals are good electrical conductors, but are not transparent. Conducting and semiconducting oxides are a type of metal oxide material that combines both these properties successfully. Thus, allowing the tuning of their electrical conductivity and optical transparency through material design. Transparent conducting materials are used in a wide-variety of applications such as touchscreens, solar cells, smart window coatings, flat panel displays and other transparent electronics. Based on a report by Market Research Future, the value of the transparent conducting film market in 2022 was estimated to be 5.9 billion and is projected to grow to 14 billion by 2032 [1]. Subsequently, the material design of transparent conducting films is highly relevant.

Depending on the application, the transparency and conductivity of the metal oxide materials can be modified by the addition of external impurities (doping or alloying) or external electric field (gating). Most commonly used transparent conducting or semiconducting oxides are indium oxide, zinc oxide, tin oxide and titanium oxide. Usually, the properties of these materials are altered by mixing them together or by addition of other metal impurities (such as aluminium, gallium, fluorine etc.) resulting in various combinations. Tin doped indium oxide (ITO), aluminium doped zinc oxide (AZO) and flouring doped tin oxide (FTO) are popular examples. Although ITO dominates the transparent conducting film market, the availability of indium on the earth's crust is relatively scarce. Inexpensive and abundant alternatives such as zinc oxide are more commercially viable.

In this thesis, I investigate the material design of transparent semiconducting oxides produced by atomic layer deposition. In particular, I focus on the material design of zinc magnesium oxide (ZMO) and zinc tin oxide (ZTO)

to understand how the addition of magnesium and tin alter the optical and electrical properties and their possible applications in solar cells.

Thin film deposition involves creating or coating a thin layer of a material over another material, also known as substrate, much like spray painting a car. While there are several different thin-film deposition techniques, in this thesis, the focus is on a specific technique called atomic layer deposition (ALD), which offers advantages such as composition control, uniform ultrathin films and can be performed at low temperatures (less than 100°C).

ALD as the name suggests involves creating thin films in a layer by layer fashion on an atomic level, using chemical reaction of gases. An ALD process of creating a metal oxide film involves the choice appropriate ingredients, usually an organic or inorganic compound containing the desired metal and water for oxygen are used. The gaseous ingredients are introduced into a chamber sequentially, where each ingredient covers the entire surface of the substrate and reacts to form a single layer of material, similar to the game of *Tetris*. ALD is a sequential process. A two element ALD (usually comprising of metal and oxygen) is called a binary ALD, whereas a multi-metal process is termed as ternary ALD.

While the binary ALD process appears straightforward and easy to manipulate, once we start to mix more than two elements, the process becomes more complex. Obtaining a transparent metal oxide material with desired properties by mixing two different binary ALD process becomes challenging as a result of deviations from the binary processes, intermixing of elements, competition among the ingredients used and so on. The manner in which two binary ALD process are combined together has a significant impact on the material growth and the properties. Depending on the combination of processes, a homogeneous mixture of the material, a nanolaminated(multilayer) material or a doped material is produced. This is analogous to making/layering cakes differently with the same set of ingredients as shown in Fig. 1. Just as baking, mixing matters very much in an ALD process.

Combining materials using ALD is of great interest as it allows control over the composition and tuning of material properties. This is desirable for the production and application of transparent conducting films. Previous research works focus solely on the well-mixed or doped material. I investigate the factors that influence the mixing during an ALD process and how the structure of the material can be changed during deposition. Thus, the goal of the thesis is three-fold:

1. Understand the growth and mixing of atomic layer deposited zinc oxide

based ternary materials.

2. Correlate the ALD processes with the observed material properties.
3. Improve the design of ALD based transparent semiconducting oxide material to suit desired applications.

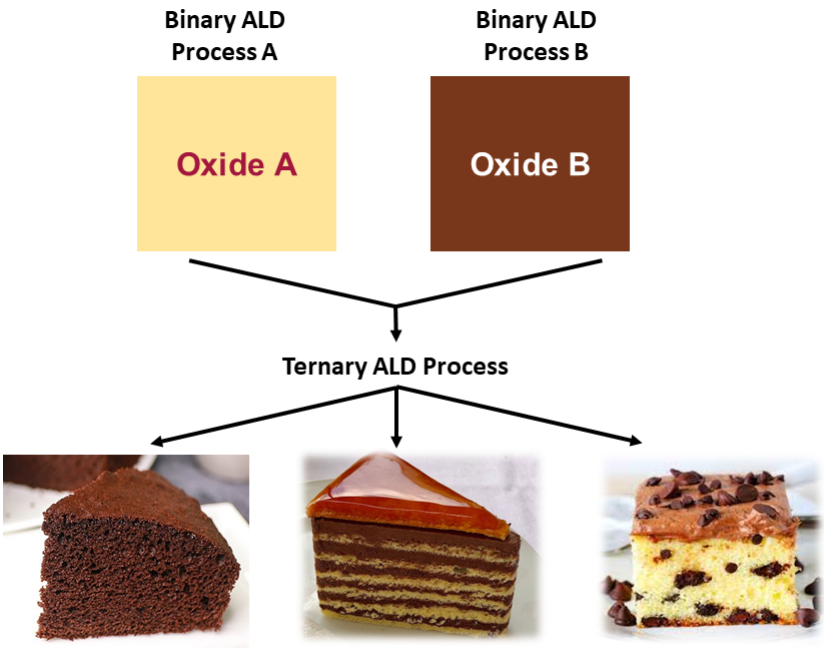

Figure 1: Combining two different binary ALD processes into a ternary ALD process produces different kinds of thin films depending on the mixing, the chocolate sponge cake represents a well-mixed material. The layered chocolate cake represents a nanolaminated thin film and the chocolate chip cake signifies a doped material.

Acknowledgements

செய்வினை செய்வான் செயன்முறை அவ்வினை
உள்ளறிவான் உள்ளம் கொளல்

குறள் எண்:677

When thou start a task anew
Seek to gain from experts' view

I want to express my foremost gratitude to my supervisor, Dr. Renaud Leturcq for giving me this great opportunity and for his unwavering support throughout these past years. I cannot thank you enough for giving me the independence and privilege to experiment, and learn from mistakes, and for patiently guiding me back on track. Your wealth of scientific knowledge and mentoring have shaped me into a scientist. Speaking of shaping me into a good scientist, I like to thank Prof. Susanne Siebentritt for her support and guidance, especially during the early months of my PhD, and her scientific inputs. I am deeply grateful for the support of Dr. David Muñoz-Rojas for being part of my CET, his scientific inputs were crucial in shaping up this thesis. I like to extend my sincere gratitude to Dr. Jérôme Polesel and Prof. Julien Bachmann for agreeing to be part of my dissertation defense committee and reviewing this thesis. I also like to thank Prof. Pedro Barquinha for hosting me at CENIMAT for the secondment and am thankful for the knowledge and skills I acquired during.

I want to thank Fonds National de la Recherche (FNR) for funding my PhD studies under the PACE project (PRIDE17/12246511/PACE), Luxembourg Institute of Science and Technology (LIST) for providing the incredible infrastructure and support to conduct most of the experiments presented in this thesis, the University of Luxembourg for maintaining a fostering atmosphere to expand my potential personally and scientifically. I like to thank Prof. Phillip Dale for organizing the PACE project, the seminars and giving an opportunity to organize an amazing conference and develop our interper-

sonal skills. I like to thank Dr. Emanuele Barborini for his support and encouraging words.

On my scientific growth, I am very grateful to Noureddine Adjeroud for showing me the workings of ALD and helping me deal with it when it did not work as expected (which was often). I like to thank Dr. Stéphanie Girod and Kevin Menguelti for their support in cleanroom and device fabrication. Although the device fabrication did not go as planned, I am still optimistic about it and will keep my fingers crossed. I want to thank Dr. Didier Arl and Dr. Vincent Roge for helping me battle FIB-SEM. I like to express my gratitude to Dr. Jérôme Guillot, Dr. Nathalie Valle and Dr. Adrian-Marie Philippe for their aid and expertise in characterizing my samples which led to interesting results and insights in this work. Special thanks to Dr. Petru Lunca Popa for always cheering me up, checking in on me and being the highlight of my day especially during those arduous days of experiments. I also like to thank Dr. Yves Fleming and Dr. Jean Luc Biagi.

I feel blessed and immensely grateful to have started this journey alongside Alfredo and Longfei and I wouldn't have wished this any other way. Thank you both for always being there, even during those long gruesome days in clean room, I knew I could count on you guys to be there in the office when I get out no matter how late. Your passions and work ethic motivated me whenever I lost my drive, so thank you for influencing me in becoming the *confident* scientist. (At this moment of finishing up, I am following the structure of your thesis especially the acknowledgments Alf! :P)

I like to thank all the members of the Transparent and Optically Tuneable Electronics group, to which I belong, and the Ferroic Materials for Transducers group, the one which adopted me. I like to thank Mohit for his contribution to this thesis and for being patient and supportive during our collaboration. Thanks to all my fellow PACE PhDs, for the interesting discussions and the teamwork at the YSC conference. My heartfelt thanks to Mauro (that Portuguese one) and Cosme for inviting me in to their social life, I really felt lost during those first few weeks at LIST, so thank you for making me feel included, for all the joyous nightouts, the drinking games and the merrymaking. Special thanks to Monica and Hugo, for being my first office mates, to Nicola Godard for answering my numerous administrative questions when I started and helping me set-up the new office, it would have been a struggle without you. I would have not survived this PhD life and made it out this far, if it wasn't for your love and friendship Samu and Paola, it has given me great strength and courage to get up and keep going.

In no particular order, I like to express my gratitude to Naveen and Ashwath

for the Tamil convos, Youri for being a source of optimism and the Salsa, Carlos, Constance, Veronika, Tina, Natalya, Antoine Dudu, Nik nik, Marco for being a good friend I can rely on, Mauro for the vibes, Barnik, John, Christina, Juliette, Uros for motivating me to do the 10k, Pierre for encouraging my creative side, Benjamin for his humour, Andreas, Diana for her kind friendship, Robert, Raoul, Vasu, Rutuja, Anthony and Julien. Special thanks to Marta and Shiv, for the refreshing hikes during lock-down and your amazing friendships.

I deeply appreciate the friendship and company of Alp, Gustavo, Monica and Shiv for hearing my rants, being my travel buddies and willing to explore different countries with me, you have helped me keep a good balance during the PhD. I am grateful that my path crossed with Emmanuella and Nathasia, for their presence helps me grow and glow. I owe many thanks to Raquel for promptly taking me on coffee breaks and keeping me sane during these past few months of writing. I am thankful to Ioanna, Laura, Laurent & Pedro for the late-night philosophical convos, Diana M, Devika for coming out of the blue to cheer me up (it means a lot), Divia, Physics Sam, Andreas, Sayantan, Minty, my Edulix fam and Marianne. To all of my friends and family, I am running out of time and energy to mention you all by name, so thank you really.

I have been waiting from the very first day of my PhD for this moment, for your thesis has been sitting at my desk since, and now it is my time to thank you Damiano for serving as a great motivator and I even made a popular science summary following in your footsteps. Jai, thank you for the consistent support, serving as my bank the first couple of months when I moved to Luxembourg and your precious friendship. I am grateful that you are only a phone call away Guru, for willing to listen, to share a laugh or some tears, your friendship is invaluable to me. Katya, you have been part of my Luxembourgish journey since day one, through highs and lows and challenging times, I cherish the memories we have made and I hope we continue to do so.

None of this would be possible without my parents, I am forever indebted to my parents for their unfailing support, encouragement and positive words throughout my entire education. I want to thank them for giving me the strength and courage to pursue my dreams, for guarding me from discouraging words and raising me to persevere. I fondly remember the many rides I took with my dad from school to home, home to tutors and back, my mom always taking care of my domestic needs amid her career. They have instilled in me the tools much needed in life - discipline (although my dad would ar-

gue I am still lazy), consistency and good work ethics, and I am incredibly thankful for that.

Contents

List of Figures

List of Tables

List of Acronyms

Often used acronyms

ALD - Atomic layer deposition

AZO - Aluminium doped zinc oxide

BP - Bilayer Period

CBO - Condction band offset

CBM - Conduction band minimum

CIGSe - Copper indium gallium selenide

CIGSu - Copper indium gallium sulphide

DEZ - Diethyl zinc

FET - Field-effect transistor

GPC - Growth per cycle

PCE - Power conversion efficiency

PR - Pulse ratio

QFLS - Quasi-Fermi level splitting

SEM - Scanning electron microscopy

SIMS - Secondary ion mass spectrometry

TCM - Transparent conducting materials

TCO - Transparent conducting oxides

TDMASn - Tetrakis(dimethylamino)tin(IV)

TEM - Transmission electron microscopy

TFT - Thin-film transistors

TOS - Transparent oxide semiconductors

UV - Ultra violet

VBM - Valence band maximum

WBG - Widebangap semiconductor

XPS - X-ray photoelectron spectroscopy

XRD - X-ray Diffraction

XRR - X-ray Reflectrometry

ZMO - Zinc magnesium oxide

ZTO - Zinc tin oxide

List of Publications

The thesis is based on the following publications.

1. **Role of ZnO and MgO interfaces on the growth and optoelectronic properties of atomic layer deposited $Zn_{1-x}Mg_xO$ films**
   Poorani Gnanasambandan, Noureddine Adjeroud and Renaud Leturcq
   Journal of Vacuum Science and Technology A-x 40.6 (2022)

2. **Electrical barriers and their elimination by tuning (Zn, Mg) O buffer composition in Cu (In, Ga) S2 solar cells: systematic approach to achieve over 14% power conversion efficiency.**
   Mohit Sood3, Poorani Gnanasambandan, Damilola Adeleye, Sudhanshu Shukla, Noureddine Adjeroud, Renaud Leturcq and Susanne Siebentritt
   Journal of Physics: Energy 4.4 (2022): 045005

3. **Correlating the growth characteristics with the optical and structural properties of atomic layer deposited zinc tin oxide**
   Poorani Gnanasambandan, Noureddine Adjeroud and Renaud Leturcq
   Submitted

4. **Structural transitions in atomic layer deposited zinc magnesium oxide**
   Poorani Gnanasambandan, Adrian-Marie Philippe, Noureddine Adjeroud, Jérôme Guillot, Nathalie Valle and Renaud Leturcq
   Manuscript In Preparation

Chapter 1

Introduction

Transparent conducting materials are used in a variety of everyday applications such as touchscreens, displays, smart windows, solar cells, sensors and in wide array of optoelectronic devices. As the name suggests, these materials combine the contrasting properties of electrical conductivity and optical transparency, and allow the tuning of the same. Typical transparent conducting materials are conductive and semiconductive oxides whose conductivity and transparency can be altered through addition of external impurities (doping) or electric field (gating) [2] [31]. While there are many deposition techniques, atomic layer deposition (ALD) has become very popular in developing doped and compound semiconducting metal oxides due its distinct advantages such as accurate control of the composition which is a given requirement for doping, low-temperature processing, ability to deposit ultra-thin films, uniformity and conformality [31].

Specifically, the self-limiting and sequential characteristic of ALD is what enables excellent control over composition, leading to an accurate control of doping levels and profiles of the semiconducting metal oxides. Synthesis of a multi-component/ternary material by ALD usually involves alternating two binary ALD process in a sequence termed as supercycle, where simply altering the relative number of binary processes within each supercycle can alter the composition. Thus, ALD provides the key to design materials to suit specific device applications. However, challenges arise in the synthesis of ternary oxides by ALD due to non-ideal behaviour resulting in deviations from the targeted properties [22]. Therefore, understanding and mitigating nonidealities arising in ternary ALD processes will not only lead to the synthesis of high-quality thin films but also pave new ways to target additional functionalities. This thesis, thus, involves the investigation and improvement

of the material properties and design of ternary oxides synthesized by ALD.

Zinc magnesium oxide (ZMO) and zinc tin oxide (ZTO) are the multicomponent transparent metal oxides of choice for investigation in this thesis. Both are wide bandgap semiconductors consisting of non-toxic, inexpensive and earth-abundant elements and are employed in a variety of optoelectronic applications. ZMO is commonly used in UV light emitting diodes, UV photodetectors and in thin-film photovoltaics [28, 32, 33]; ZTO finds application as gas sensors, channel layers in thin-film transistors and in thin-film photovoltaics[34]. In particular the ALD deposited ZMO and ZTO thin films have gained a lot of attention as buffer layers in copper indium gallium selenide (CIGS) solar cells owing to their tuneable optical properties [11] [35].

Most of the existing literature on the ALD growth of ZMO and ZTO are centered either around their device application or on the thin film characterization, few studies focused on the growth kinetics and even fewer correlated the growth kinetics with the material properties in detail [36] [26] [37]. The interplay between the binary ALD processes, their surface chemistries on the growth kinetics of the ternary ALD process remains unexplored. Furthermore, it becomes quintessential to consistently correlate the ALD mixing kinetics in a ternary process with the material properties observed to achieve accurate control over doping or alloying (doping when a small amount of material is mixed, alloying when the mixture involves more than 10%). To this effect, the thesis aims to address the following research challenges,

1. **Understand growth and mixing kinetics**: Involves understanding the interplay between the binary ALD processes (ZnO and MgO, ZnO and SnO_x) and role of their interface chemistries over the ALD growth of the ternary ZMO and ZTO thin films. Mixing kinetics focuses on the influence of the total number of ALD reaction cycles within a supercycle also known as the bilayer peirod over the growth kinetics. Investigating the optimal mixing to achieve effective doping of one material into another.

2. **Correlate growth kinetics and the material properties** Examining the material properties to understand the effect of doping or alloying of one metal oxide with other and establishing process-structure-property relationships with the ALD grown ZMO and ZTO thin films. Understanding the transitions of ternary material from well-mixed to a nanolaminated material with the ALD process.

3. **Application of ALD grown ternary transparent metal oxides** By developing reliable and reproducible ALD process, improve material

design of ALD based transparent semiconducting oxide material to suit desired applications. Tuning of optical properties of ALD grown ZMO and ZTO to serve as buffer layers in thin-film solar cells.

The thesis is structured as follows, while the current chapter provides a general introduction, Chapter 2 details the scientific background necessary to comprehend the nature of transparent metal oxide semiconductors and the concept of doping in semiconductors their unique electronic band structure and optical properties. Chapter 2 includes discussion on the application of transparent semiconducting oxides in solar cells and thin-film transistor with focus on zinc oxide based ternary materials, zinc magnesium oxide and zinc tin oxide owing to their popularity in these applications. The latter part of the chapter includes an overview of atomic layer deposition, the synthesis method on focus in this thesis, followed by a discussion over the existing literature on atomic layer deposited zinc magnesium oxide and zinc tin oxide films and the research questions that remain unaddressed which defines the scope of this thesis. Chapter 3 details the experimental methods from synthesis by atomic layer deposition to the various thin-film characterizations performed during the course of this study.

Chapter 4 features the main outcome of the synthesis of zinc magnesium oxide by atomic layer deposition and addresses all the major objectives. We gather new insights into the growth kinetics of the ALD grown ternary zinc magnesium oxide and the effect of ZnO and MgO interfaces. We conclude that bilayer period can serve as an effective way to understand growth kinetics in ternary material synthesis by ALD, providing an alternative to in-situ quartz crystal microbalance analysis. Chapter 4 establishes a process-structure-property relationship of ALD grown ZMO and also briefly summarizes the results of ALD deposited ZMO buffer layers in chalcopyrite solar cells.

Complementing Chapter 4, Chapter 5 focuses on the structural transitions in the ALD grown zinc magnesium oxide detailing growth regimes that lead to the formation of either a mixed, nanolaminated or intermediate confined material structures. In particular, chapter 5 compares the structural analysis through different techniques namely, XPS, SIMS and TEM. These intermediate structures might pave way towards the realization of polycrystalline-amorphous superlattices using atomic layer deposition.

Chapter 6 is concerned with the synthesis of zinc tin oxide by ALD addressing the major research challenges of the thesis similar to chapter 4. We conclude that bilayer period provides an additional knob in the tuning of material properties of ALD grown ternary materials. The application of ALD based zinc tin oxide films as channel layers in TFT is ongoing.

A concluding chapter 7 summarizes the outcomes and provides outlook for future research.

Chapter 2

Transparent Conducting Materials & Applications

Transparent conducting materials or TCMs, as the name suggests are highly transparent and electrically conducting materials employed in a wide-range of everyday applications from touchscreens, flat panel displays, solar cells to smart windows etc. Out of those, oxides make the most popular transparent conducting materials, hence the term transparent conducting oxides or simply TCOs. Cadmium oxide (CdO) combining optical transparency with good electrical conductivity first opened the doors to the discipline of TCOs in 1907 [38], followed by tin dioxide (SnO_2) 30 years later, then zinc oxide (ZnO), indium oxide (In_2O_3) and so on. Recently ultra-wide band gap TCO - gallium oxide (Ga_2O_3) has gained a lot of attention in the field of power electronics [39]. Nonoxide transparent conducting materials include the widely studied boron phosphide (BP) and copper iodide (CuI), chalcopyrite ($CuAlS_2$), Cu-alloyed zinc sulfide ($Cu_xZn_{1-x}S$) , oxy-chalcogenides etc. [40].

2.1 Transparent Oxide Semiconductors

TCOs are a unique class of materials as they combine optical transparency and electrical conductivity which are conflicting properties by nature. Glasses are highly transparent insulators while metals are highly conducting reflectors/mirrors; to achieve a highly transparent conducting material, one needs to make either the former more conducting or the latter more optically transparent. Transparent semiconductors are promising candidates as they offer transparency akin to insulators and moderate conductivity which can be im-

proved simply through doping. The electronic band structure becomes highly relevant to understand and distinguish the nature of these various classes of materials.

2.1.1 Electronic Band structure

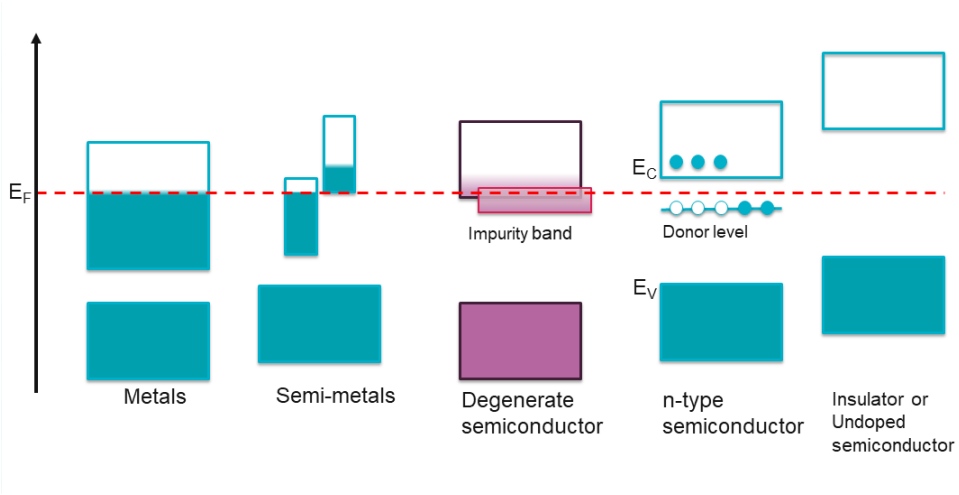

Figure 2.1: Band structure

In the band theory of solids, atoms in a periodic structure(a lattice) are said to form a continuum of energy states called energy bands rather than discrete energy states or levels due to overlapping atomic orbitals. These energy bands have finite widths depending on the overlapping parent orbitals hence there appears gaps in the continuum, known as band gaps. Classification of a material into a metal, semiconductor or insulator depends on how these energy bands are filled with electrons, especially the last or upper bands. The energy bands are filled with electrons from the bottom; the density of states of an energy band gives the number of states available within the band for electrons to occupy, the Fermi-Dirac distribution gives the probability of a state being occupied and the Fermi level E_F denotes the total chemical potential of the electrons occupying the energy bands. When the last energy band is partially filled, as is the case in metals, electrons can move freely to conduct electricity. Semi-metals have partially filled overlapping energy bands in place of a partially filled energy band. If the last band however, is completely filled, the electrons are no longer free to conduct resulting in an insulator or semiconductor and the band gap becomes very relevant in these materials. The Fermi level (E_F) gives the highest energy that an electron can occupy at absolute zero, thus in metals and semi-metals, E_F

falls within the partially filled band as shown in Fig. 2.1. Likewise bands and band gaps around the Fermi level are of main concern in semiconductors and insulators, interestingly E_F in these materials falls above the completely filled band inside the band gap. This *band-gap* becomes a defining feature of these materials and the size of this band-gap or energy gap distinguishes a semiconductor from an insulator (from here on terms bandgap, band-gap, band gap refers to this defining parameter). The completely occupied band in these systems is called the valence band (of energy E_V below E_F) as shown in Fig. 2.1, and the conduction band is the next available energy band that an electron can occupy above the band-gap which is empty at absolute zero. Not only are semiconductors and insulators differentiated by the size of the energy gap but also by their tendency to generate free electrons easily into the conduction band. As there are no available energy levels inside the gap, an electron requires an energy equivalent to the gap to be excited from the valence band into the conduction band. In an intrinsic or pure semiconductor such as Si or Ge, at temperatures above absolute zero, few electrons from the valence band are excited into the conduction band across the band-gap, resulting in electrical conduction. The conductivity is small owing to the small number of free electrons available as compared to metals hence the term - *semiconducting material*. With increasing temperature, more electrons are excited into the conduction band resulting in increased conductivity. In insulators, the thermal energy available at room temperature is not sufficient enough to excite a few electrons from the valence band across their large sizeable band-gap, therefore they remain poor conductors even with increasing temperatures. Wide-bandgap semidconductors (WBGs) have band-gaps in-between the conventional semiconductors with narrow band-gap and insulators with a large band-gap. This makes them suitable to operate at high temperatures as the thermal energy required to excite the electrons across the gap would be higher, making their normal operating temperature to be higher than conventional semiconductors. Wide-bandgap metal oxide semiconductors have an energy gap of $\geq$ 3 eV making them suitable for various high voltage, high frequency applications.

Conductivity in n-type semiconductors is due electrons, the presence of shallow donor or impurity states close to the conduction band introduced either by oxygen vacancies (in oxides) or metal interstitials or by extrinsic dopant atoms. These impurities readily undergo thermal ionization, generating carriers and in turn conduction; Fig.2.1 depicts the electrons being excited into the conduction band from the donor level of an n-type semiconductor. In a p-type semiconductor, conductivity is due to empty states or holes in the valence band and the impurities are acceptor states close to valence band.

The doping concentration, electrons in n-type and holes in p-type, helps to understand the behaviour of the semiconductors which can be further differentiated into non-degenerate and degenerate semiconductors depending on the level of doping. TCMs are formed by doping transparent semiconductors, they exhibit high conductivity when degenerately doped. With transparent wide-bandgap metal oxide semiconductors, a non-degenerate doping leads to a transparent semiconducting oxide (TOS or Transparent oxide semiconductors) while degenerate doping results in transparent conducting oxide (TCO).

Intrinsic semiconductor

In an n-type semiconductor, the concentration of electrons present in a conduction band can be determined from the number of states of electrons and the Fermi distribution function which gives the probability of occupied states as,

$$n = \int_{E_C}^{\infty} N(E)F(E)\,dE \quad \text{with} \quad F(E) = \frac{1}{1+\exp[(E-E_F)/kT]}. \tag{2.1}$$

The density of states near the bottom of the conduction band, assuming a parabolic energy dispersion, can be approximated to $N_C = 2\left(\frac{m_e^* kT}{2\pi\hbar^2}\right)$, with the electron effective mass m_e^*, boltzmann constant k and temperature T. Then above equation can be written as

$$n = N_c \frac{2}{\sqrt{\pi}} F_{1/2}\left(\frac{E_F - E_C}{kT}\right) \tag{2.2}$$

where $F_{1/2}$ is the Fermi-Dirac integral with E_C - the energy at bottom of the conduction band [41]. In a non-degenerate semiconductor, the doping concentration is lower than N_C and the Fermi level lies well below the conduction band minimum ($E_C - E_F >> kT$), then Boltzmann statistics can be applied and the Fermi-Dirac integral reduces as $F_{1/2}(\eta) = \frac{\sqrt{\pi}}{2}\exp\eta$ making equation (2.2) to become

$$n = N_C \exp\left(\frac{E_F - E_C}{kT}\right) \quad \text{or} \quad E_C - E_F = kT\ln\left(\frac{N_C}{n}\right). \tag{2.3}$$

Similarly, the hole concentration for an intrinsic p-type semiconductor can be written as

$$p = N_V \exp\left(\frac{E_V - E_F}{kT}\right) \quad \text{or} \quad E_F - E_V = kT\ln\left(\frac{N_V}{p}\right), \tag{2.4}$$

with N_V being the effective density of states of the valence band and E_V is the energy at valence band maximum. In an undoped semiconductor, the intrinsic carrier concentration $n_i = n = p$ as a result of charge neutrality and by equating the above equations for n and p, one can find that the Fermi level lies close to the middle of the energy gap.

Doped semiconductor

In a doped semiconductor, when donor atoms are introduced into a semiconductor material, donor energy levels are introduced inside the energy gap. A donor level filled with an electron is neutral and the amount of energy required to excite an electron from the donor level (E_D) into the conduction band i.e, the ionization energy of donor impurity can be calculated based on a simple hydrogen atom model. The ionization energy of a hydrogen atom in vacuum and the distance between the hydrogen nucleus and the electron in ground state (Bohr radius) are given as,

$$E_H = \frac{m_0 q^4}{32\pi^2 \epsilon_0^2 \hbar^2} \quad \text{and} \quad r_H = \frac{4\pi\epsilon_0\hbar^2}{m_0 q^2} \tag{2.5}$$

As the donor impurity is embedded inside the semiconductor and not in vacuum, taking into account of the effective mass of electrons (m_e^*) and the permittivity of the semiconductor (ϵ_s), the energy required to overcome the coulombic attraction between the donor electron and its nucleus can be computed as,

$$E_C - E_D = \frac{E_H}{\epsilon_s^2}\frac{m_e^*}{m_0} \quad \text{and} \quad r_H = \frac{\epsilon_s m_0}{m_e^*} r_H \tag{2.6}$$

where E_H=13.6 eV and r_H=0.053 nm. The calculation of ionization energy of acceptors in case of p-type semiconductors follows the same as donors. For most semiconductors the above energy is found to be $\lesssim$0.1 eV comparable to thermal energy kT putting the donor levels close to conduction band edge and also resulting in complete ionization at room temperature. Now the concentration of donor electrons that have been ionized can be determined similar to equation (2.1) as

$$N_D^+ = N_D \frac{1}{1 + 2\exp[(E_F - E_D)/kT]} \tag{2.7}$$

where the factor 2 arises out of donor site ground-state degeneracy and N_D is the total donor concentration. In an n-type semiconductor, at moderate temperatures, all the donor impurities are ionized; charge neutrality means the electron concentration $n \simeq N_D^+$, therefore equating the above equation

with (2.3), the Fermi level can be found to lie in-between the conduction band and donor level as portrayed in Fig 2.1. In a non-degenerate semiconductor, temperature plays a huge role in electron concentration, at low temperatures almost no thermalization from donor level takes place $n << N_D$ and at very high temperatures, the semiconductor becomes intrinsic as there is enough energy available for transition from valence band to conduction band $n \simeq n_i >> N_D$.

Degenerate semiconductor

A degenerate semiconductor is one with heavy doping with a doping concentration more than the effective density of states ($\geq N_C$). The Boltzmann approximation no longer applies and the Fermi-Dirac integral in equation (2.2) is evaluated numerically. With heavy doping, the large electron concentration thus generated lead to many-body effects such as screening effect at the impurity sites which reduces the ionization energy almost to zero [42]. The several shallow donor states introduced by heavy doping combine to form an impurity band which overlaps into the conduction band and the Fermi level moves outside the gap into the conduction band similar to metals. Fig 2.1 shows the band structure of a degenerately doped n-type semiconductor. With almost to nil ionization energy, the carrier concentration and thus conductivity is independent of temperature in a degenerately doped semiconductor but limited by ionized impurity scattering beyond a carrier concentration of 10^{20}cm^{-3} [43]. Ternary oxide materials are often used for transparent electronics because their electronic band structure can be tuned by controlling the composition.

Electrical conductivity

Conductivity for n-doped semiconductor σ not only depends on the electron concentration but also on the carrier mobility. And the mobility μ depends on the effective mass of carriers, in the case of n-type material

$$\sigma = ne\mu \quad \text{and} \quad \mu_e = e\tau/m_e^*, \tag{2.8}$$

where τ is the relaxation time. From this relation, a map of classification of different materials can be obtained with the n_c-μ diagram (see Fig. 2.2) by plotting the carrier concentration vs mobility. *Metals* are located at the top-center with very high carrier concentration and in turn very high conductivity (note that bismuth on the top-left is a semimetal). *Semiconductors* on the bottom-right with a low carrier concentration but high mobility show good conductivity. The conductivity of the semiconductors could always

be increased by doping, however heavy doping becomes counteractive as it causes more ionized-impurity scattering decreasing the mobility. Wide band-gap metal oxide semiconductors ($\geq$ 3 eV) show conductivity up to an order of 10^4S/cm due to intrinsic (oxygen vacancies or interstitials) or extrinsic doping. While the non-degenerately doped TOS is used for its semiconducting properties, degenerately doped TCOs are used as transparent electrodes. Carrier concentration in the former case (TOS) is in the intermediate range and does not exceed beyond 10^{18}cm^{-3} while for TCOs it is limited to several 10^{21}cm^{-3}. Popular TCOs are obtained by doping the binary transparent semiconductors such as doping indium oxide with tin (ITO), doping tin dioxide with fluorine (FTO) and zinc oxide with aluminium (AZO) etc. Most importantly doping governs whether a transparent oxide remains electrically semiconducting or electrically metallic.

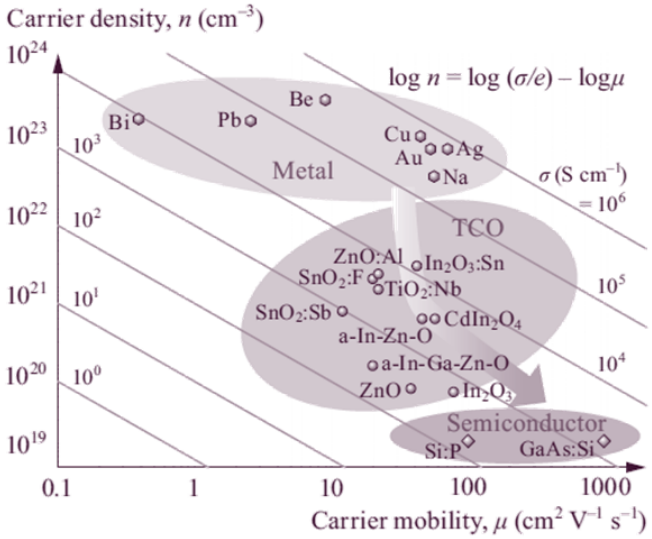

Figure 2.2: Carrier mobility vs density [2], Metals at the tpo-center, semiconductors at the bottom-right and TCOs in between.

2.1.2 Band Structure of TOS

While carrier concentration can be controlled via doping, mobility is a material-dependent parameter, a smaller effective mass corresponds to larger mobility and the effective mass is deduced from the curvature of the energy bands in the energy diagram as a function of crystal momentum k, $\frac{1}{m^*} \propto \frac{d^2E}{dk^2}$. The

larger the curvature of the conduction band, the smaller is the electron effective mass and higher is the mobility. In a metal oxide semiconductor, the conduction band consists of empty ns^0 orbitals of the metal cation M^{2+} and the valence band is made of occupied O^{2-} oxygen $2p^6$ orbitals. The metal Ms orbitals with their spherical symmetry make a large overlap with neighbouring Ms orbitals and Op orbitals resulting in a large conduction band dispersion leading to small electron effective masses. Atomic orbitals in metal oxides overlap as largely as in metals because the intercationic distances in metal oxides are very similar to the interatomic distances in metals. Fig. 2.3 depicts the large curvature of the conduction band of a wurzite

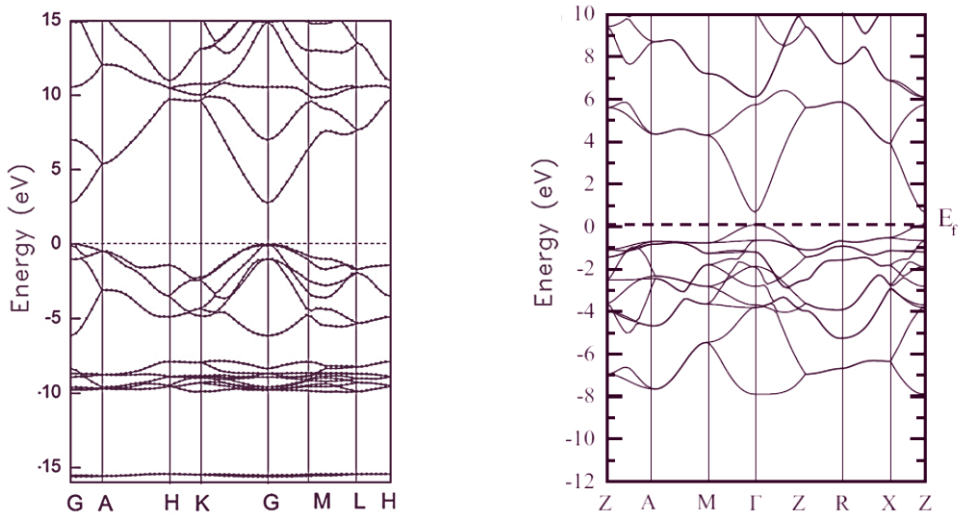

(a) ZnO (b) SnO_2

Figure 2.3: Band structure of pure ZnO [3] and pure SnO_2 [4]

structure ZnO and pure rutile SnO_2 which arises due to large overlap of the orbitals causing large energy dispersion. The valence band maximum and E_F is set to zero energy which lies below the conduction band minimum denoting an n-type material; also SnO_2 shows much flatter valence band than ZnO. Additionally, the symmetry makes this Ms-Op-Ms network insensitive to structural variations rendering similar mobilities to polycrystalline and amorphous counterparts of the crystalline material. Thus metals with d^10s^2 electronic configuration make up most of the conventional TOS ans TCOs. Smaller effective mass ensures higher mobility, but carrier scattering limits mobility. Carrier scattering occurs as electrons collide with lattice ion, defects, impurities and other electrons. The average time between two

consecutive scattering events during which an electron can move freely is the relaxation time τ. When carrier scattering increases, τ reduces and decreases the mobility (see 2.8). Scattering mechanisms thus play a crucial role in shaping the electrical properties of a material. The scattering mechanisms of main concern in transparent oxide semiconductors are phonon scattering, impurity scattering and grain-boundary scattering. Phonons are the elementary excitation of lattice vibrations in a crystal; interaction of electrons with phonons results in electron-phonon scattering. In monocrystalline ZnO for example, mobility is limited by optical phonon scattering yielding a maximum of 220cm^2/Vs [44]. In polycrystalline materials, the existence of grain boundaries act as scattering centers causes grain boundary scattering and decreasing the mobility, hence grain size becomes relevant. In TCOs, mobility is limited by ionized-impurity scattering as doping increases impurities i.e, dopant atoms.

2.1.3 Optical transparency

The wide band-gap oxide semiconductors are transparent in the visible range up to 10 μm, as shown in Fig.2.4, where the transparency window of conventional semiconductors are limited to the infrared region. The absorption edge in the far infrared region is governed by the lattice vibrations between 10 to 200 μm and the absorption edge in the ultraviolet region is due to the fundamental absoprtion or inter-band absorption.

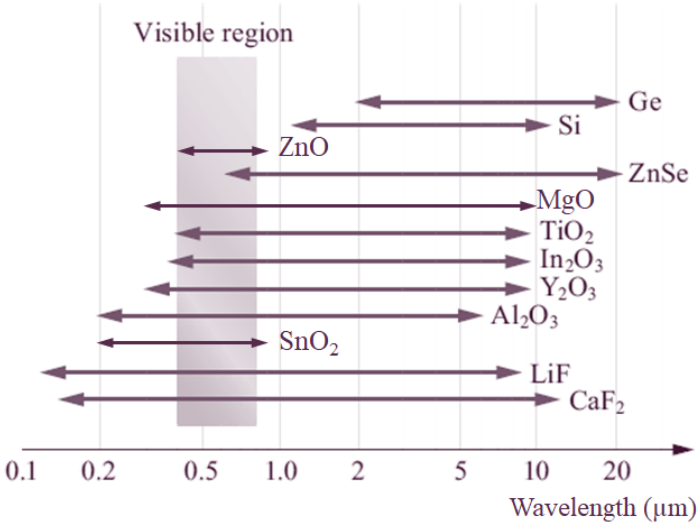

Figure 2.4: Transparent materials vs wavelength[2].

Inter-band absorption

This fundamental absorption is due to the electronic transition across the bandgap E_g when light is incident on the material imparting enough energy for an electron from the valence band to be excited into the conduction band. A transition involving photon only is a direct band-to-band transition whereas a if it involves both a photon and a phonon, the absorption is known as an indirect transition. Direct bandgap transitions occur when the valence band maximum and conduction band minimum appear at the same point in the momentum space (k-space) as depicted in Fig. 2.5. Indirect transitions dominate optical absorption when the extrema of valence band and conduction band occur at different point in the momentum space requiring a phonon-mediated transition to satisfy conservation of momentum. Only

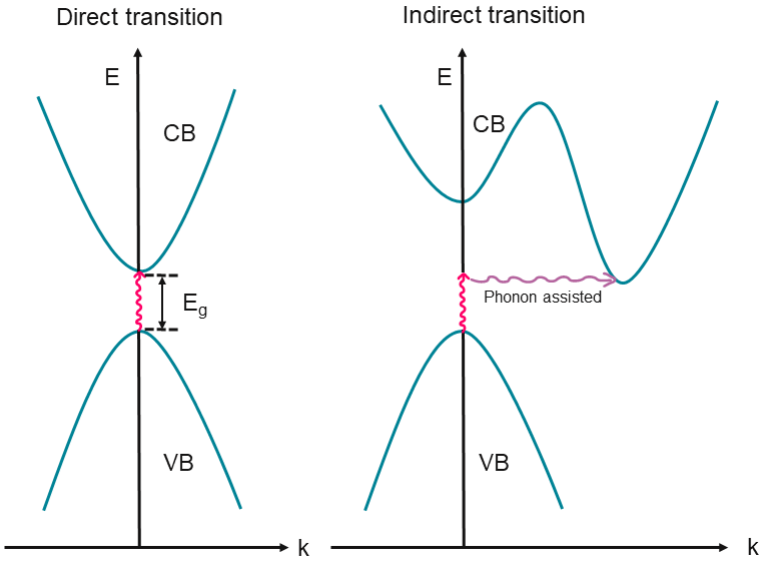

Figure 2.5: Schematic of direct and indirect transitions. CB and VB stand for conduction band and valence band respectively. In direct transition extrema of CB and VB occur at k=0 while in the indirect transition, the minimum of CB and maximum of VB are at different values of k requiring phonon assisted transition across the forbidden energy gap. Pink lines indicate photon and purple line phonon.

the photons of energy equivalent or higher than the bandgap are absorbed. Photons of lower energies are not absorbed and simply transmitted through the material. Hence the transparency window or the apparent colour of the semiconductor is due to the fundamental absorption edge of the material. For the wide-bandgap metal oxides as the absorption edge moves towards

the ultraviolet region, the transmission becomes colourless as all the visible spectrum are transmitted. The transmission window of a TCO/TOS should span UV-VIS-NIR region, however, doping influences these absorption mechanisms. For a detailed summary of absorption processes refer to [25].

In a degenerately doped n-type wide bandgap semiconductor, the Fermi level E_F shifts above the conduction band minimum as can be seen in 2.1, this not only increases the carrier concentration but also widens the optical bandgap E_g. This blue shift of UV absorption edge caused by conduction band filling is called Burstein–Moss shift and the amount of shift in energy gap is given by the relation, $\Delta E_g = n_c^{(2/3)}$ [45] [46] [47].

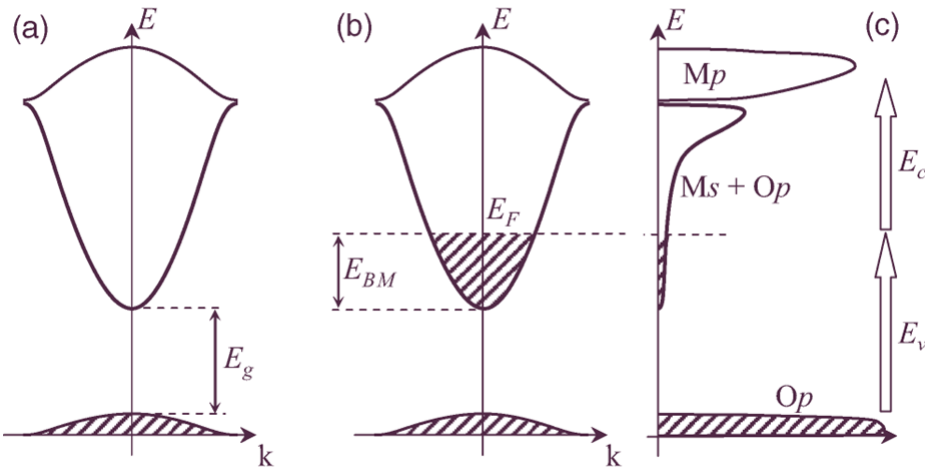

Figure 2.6: Electronic band structure of a) transparent semiconductor b)degenerately doped transparent semiconductor with BM shift c) density of states [5]

The valency of the dopant atom/ion plays a crucial role in determining an effective doping be it replacing the native metal ion M^{2+} or the oxygen O^{2-}. In doping zinc oxide by aluminum, Al^{3+} ion replaces Zn^{2+} ion increasing the free carrier concentration in Al doped ZnO resulting in high conductivity. Similarly in fluorine doped SnO_2 the fluorine ion F^- is expected to generate free carriers by replacing O^{2-}. For an effective donor doping in an n-type material, aliovalent ions are opted to ensure the generation of charge carriers, resulting in a BM shift. However, depending on the applications, specific properties can be optimized by choosing other type of dopant ions. A shift in optical bandgap can also occur due to the broadening of bands above or below

conduction band minimum due to interactions between the dopant states and the host atoms, where the bandgap becomes dependent on composition. For example, the optical properties of ZnO can be tuned by Mg doping. With the valency of dopant Mg^{2+} ion being similar to Zn^{2+}, the Mg *3*s orbitals hybridize with the Zn *4*s orbitals shifting the conduction band minimum and increasing the optical bandgap [48]. The blue shift of the fundamental absorption edge due to Burstein-Moss effect with doping in a Ga:ZnO system is shown in Fig. 2.7 [6].

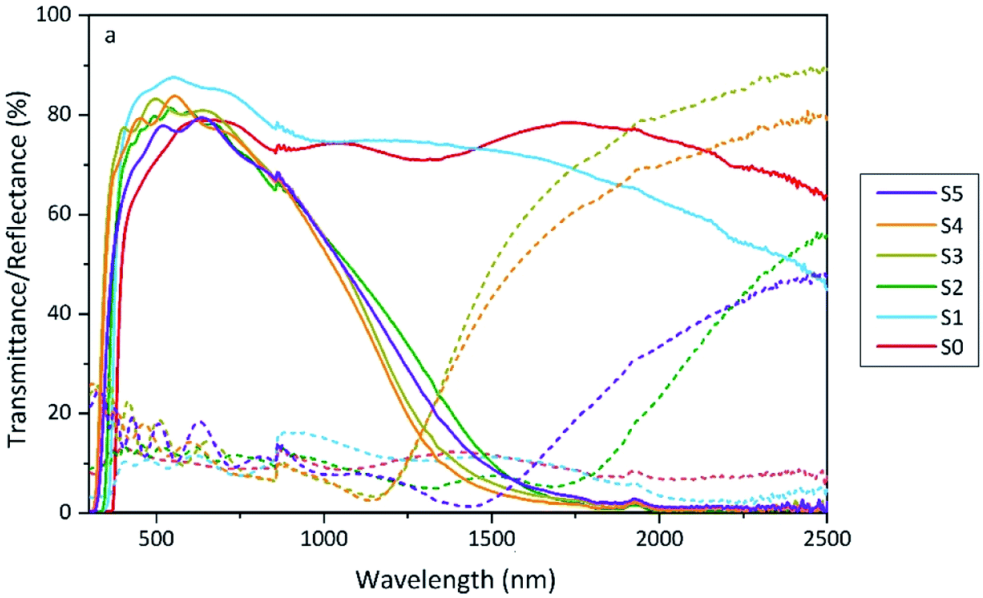

Figure 2.7: Optical Transmission (solid lines) and Reflectance (dashed lines) spectra of Gallium doped ZnO with increasing Ga at % from samples S1 to S5. [6].

Plasmon Resonance

Additionally, the reflection spectra also governs the optical nature of the material. The free electron gas model can quite well describe the optical properties here similar to the electrical conductivity. Combining the frequency dependent AC conductivity and the Maxwell's equations, one arrives at complex dielectric constant $\epsilon(\omega) = 1 - \frac{\omega_p^2}{\omega^2}$, where $\omega_p = n_c e^2/\epsilon_0 m^*$ [49]. The negatively charged conduction electrons balanced by the background positive charge of ions behave as a collective plasma oscillating at a characteristic frequency ω_p called the plasma frequency. If the incident light has a frequency $\omega < \omega_p$, the conduction electrons screen the electric field of the light. On

the other hand, when $\omega > \omega_p$ higher frequency photons pass through as the carriers cannot respond fast enough to screen. From above equation, the condition for non-reflectance in terms of carrier concentration can be given as,

$$n_c < \frac{4\pi^2 \epsilon_0 m^*}{\mu_0 e^2 \lambda^2} \tag{2.9}$$

provided $\frac{2\pi}{\lambda} > \omega_p$. From this relation we can determine that for an effective transmission in the visible range up to 800nm, the carrier concentration cannot exceed 10^{21}cm^{-3}. Moreover, the highly reflective nature of metals becomes evident as the high carrier density puts the plasma frequency in the UV range. Free carrier absorption occurs as the excess of free carriers in a semiconductor act collectively as electron gas or plasma causing an optical absorption at infrared region. The absorption of photon by free carriers results in intraband transition mediated by phonon, electrons moving from a lower energy state to higher energy state within the same conduction band or to higher conduction bands (valence band free-carrier absorption for holes). This free carrier absorption edge can be seen appearing with increasing Ga doping in the IR region in Fig. 2.7 [6]. Not just the conductivity but also the optical window is limited by carrier concentration; consequently doping plays a critical role in tuning the optical and electrical properties of these transparent oxide materials.

Thickness dependent Optical Properties

The optical coefficients refractive index (n) and extinction coefficient (k) govern the optical properties of a material discussed so far - the transmission, absorption and reflection. These intrinsic optical properties depend on the chemical composition and chemical structure of the material. Refractive index describes the propagation of light through the material, while the extinction coefficient describes the attenuation of the light propagation, combined to give the expression for the complex refractive index written as $\mathfrak{n} = \text{n} + \text{ik}$, where n is the real part of refractive index. When it comes to optical properties of thin-films, extrinsic factors such as film thickness, texture and optical properties of the substrate cannot be ignored. When a transparent conducting or semiconducting film is deposited on a substrate, multiple reflections and transmission occurs at the interface between air and the film, the film and substrate interface because of interference, which changes the overall effective refractive index and extinction coefficient. Moreover, the larger the thickness of the films, larger is the interference. Thus refractive indices of each medium, the extinction coefficients and film thickness

strongly influence the optical properties of thin-films. When it comes to texture, roughness introduces thickness variation across the film which affects the optical properties as well.

2.2 Applications of Transparent Oxides

Transparent oxides are used in a wide array of optoelectronic applications such as light emitting diodes - LEDs, OLEDs touchscreens, displays (LCDs), smart windows, solar cells, photocatalysis and optical coatings etc., forming the backbone of transparent electronics. They are an essential component in thin film photovoltaics - chalcopyrite, organic, pervoskite and multi-junction solar cells. Depending on the application a transparent oxide semiconductor can be doped to form a TCO or remain a TOS. In the aforementioned applications, as TCOs they serve as transparent electrodes and as TOS their semiconducting properties can be used in complex device structures. A fundamental understanding of the role a transparent oxide material plays in these optoelectronic devices becomes essential to achieve effective material design. Of the various applications, we focus on thin film photovoltaics (TPV) and thin film transistors (TFT) which form the building block of renewable energy and display technologies respectively. Understanding the role of transparent oxides in these devices is key in material design, synthesis and engineering energy-efficient devices.

2.2.1 Thin film Photovoltaics

Thin film solar cells based on copper indium gallium selenide (CIGS) play a major role towards addressing the current climate and energy crisis. The main advantages are high efficiency, long term stability, low cost in manufacturing, environmentally friendly materials, flexibility in design and lightweight [50, 51, 52]. CIGS based solar cells have achieved a conversion efficiency up to 23.6 [53], to compare the most efficient silicon cells are around 26.7%. Chalcoyprite semiconductors $CuInS_2$, $CuInSe_2$ and $CuGaSe_2$ or an alloy of them are used as absorbers in these thin film solar cells. Another advantage of chalcopyrite solar cells is that they can be incorporated in to a multijunction solar cell. A multijunction solar cell consists of two or more absorbers, each forming an individual solar cell and absorbing different parts of a solar spectrum. This requires bandgap engineering to ensure the bandgap of the multiple semiconductors capture different energies of the solar spectrum and achieve high efficiencies. While the bandgap of $Cu(In, Ga)Se_2$ (CIGSe) varies from 1.0 eV (for $CuInSe_2$) to about 1.7 eV (for $CuGaSe_2$) making it suitable

for a bottom cell, its selenium free sulfide counterpart $Cu(In, Ga)S_2$ (CIGSu) can be used as a top cell with its tunable direct bandgap between 1.54 eV (for $CuInS_2$) and 2.53 eV (for $CuGaS_2$) [54] [55].

CIGS solar cells

A typical chalcopyrite based solar cell is a heterojunction solar cell consisting of a p-n heterojunction developed between the p-type CIGS absorber and n-type region formed by buffer, window and TCO layers [9].

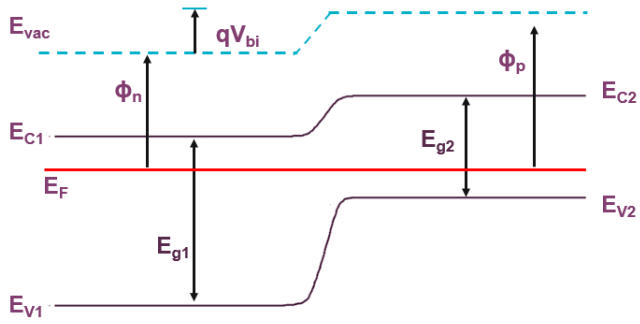

Figure 2.8: A simplified energy band diagram of p-n heterojunction under equilibrium. The p-type material on the right with energy gap E_{g2} and n-type material on the left E_{g1} when brought together form the depletion region causing a built-in voltage V_bi to develop across the junction and band-bending occurs. [7].

In a p-n heterojunction model of a solar cell, a junction is created by bringing together two different materials with different bandgaps. The holes from the p-side and electrons from the n-side diffuse into the other and recombine at the junction. As the junction is depleted of majority carries, it leaves the n-side positively charged and p-side negatively charged creating an electric field (known as built-in potential V_{bi}) at the junction. This electric field causes drift of minority carriers while acting as a barrier to diffusion of majority carrier thus achieving a thermal equilibrium. At this juncture, the Fermi levels on the p-side and n-side are equal and band-bending occurs as shown in Fig.2.8[56].

When the semiconductors absorb light, electron-hole pairs are generated, there exists excess of minority carriers, electrons now on the p-side and vice versa. The electric field across depletion region is enough to separate the

photogenerated carriers from recombining [7]. The light induced excess carrier generation drives the p-n junction out of equilibrium and the Fermi level readjusts splitting into minority and majority quasi Fermi levels on either side to take the charge imbalance into account. This quasi-Fermi level(QFL)

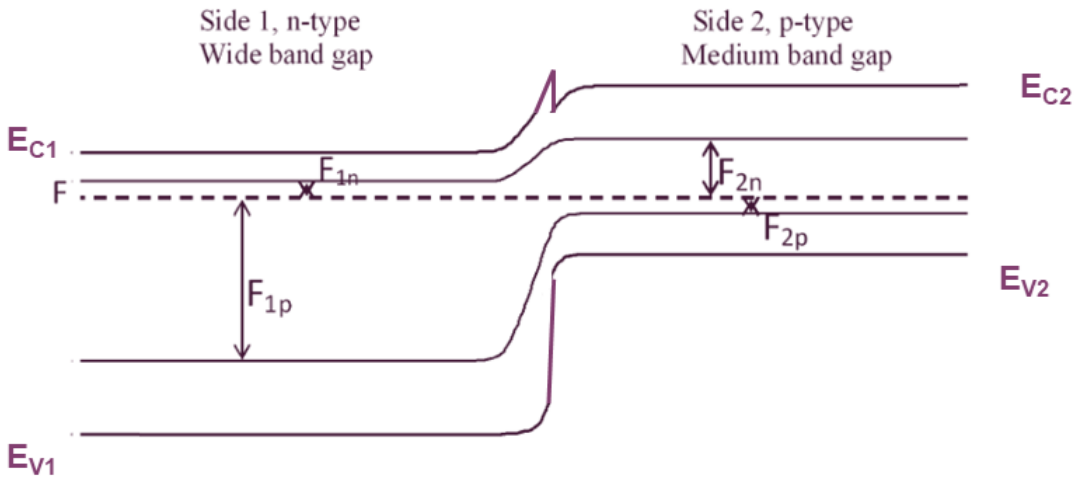

Figure 2.9: A schematic of p-n heterojunction solar cell under illumination. The quasi-Fermi levels splitting on the n-side involves majority electrons and minority holes (F_{1n} and F_{1p}) and on the p-side, majority holes and minority electrons (F_{2p} and F_{2n}). The difference in quasi-Fermi levels $F_{2n} - F_{1n}$ and $F_{1p} - F_{2p}$ contribute to the open-circuit voltage [8].

splitting depicted in Fig.2.9 [8], creates a potential difference among the electron QFL on the n-side and between hole QFL on the p-side contributing together to the open circuit voltage of the solar cell. Open circuit voltage (V_{OC}) is the difference of potential across the p-n junction when there is no load and can be used to generate useful electrical power when connected to a load. The open circuit voltage is the maximum voltage a solar cell can generate/provide.

The layout of a chalcopyrite based solar cell consists of soda lime glass substrate followed by molybdenum back contact and the p-type absorber such that the structure follows SLG/Mo/CIGS/Buffer layer/Window layer/TCO layer [9] as shown in Fig. 2.10.

For light to reach the absorber layer, the buffer layer and window layer need to be transparent. Optically a transparent oxide can be used as a transparent top contact, window layer and buffer layer. Moreover, it is pertinent for a

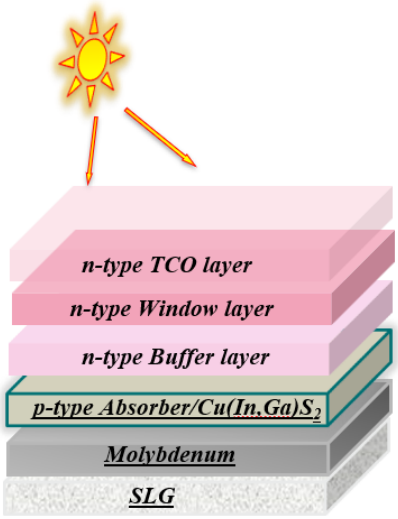

Figure 2.10: Typical stack of a chalcopyrite solar cell [9].

buffer layer to provide good band alignment with the absorber and window layer. Electrically, while a TCO can serve as top electrode, a TOS is better suited to be a buffer layer, since a good semiconducting buffer layer ensures efficient charge separation and transport between the absorber layer and window layer whilst reducing recombination. Recombination of electron-holes is common at interfaces due to the presence of defect states and a favourable band alignment between the different layers assures reduction in interface recombination. In short, in a heterojunction chalcopyrite solar cell, buffer and window layers are quintessential for p-n junction formation and charge separation. Furthermore, a proper formation of conduction band offset (CBO) at the absorber and buffer layer interface is necessary for attaining a high-performance device. Traditionally cadmium sulfide (CdS) is used as a buffer layer in high-efficiency CIGS devices with intrinsic ZnO and AZO serving as window layers ([57] [58]need to list few more references).

In theory the quantities QFL and V_{OC} can be used interchangeably, however, in poorly performing devices the open-circuit voltage is less than the internal quasi-Fermi level splitting(QFLS) termed as QFLS loss. One of the most critical factors in accomplishing a high-performance device and avoiding this QFLS loss is to reduce interface recombination at the buffer/absorber interface. A positive conduction band offset (CBO) occurs when the conduction band minimum of the buffer layer is higher than that of the absorber layer resulting in a formation of spike like interface. And a negative conduction

band offset results in a cliff like interface as the CBM of buffer layer is lower than that of the absorber. The cliff-like structure acts as a barrier to injected electrons from the n-side in forward bias and increases the interface recombination, thus reducing the V_{OC}. Fig. 2.11 shows the schematic of the

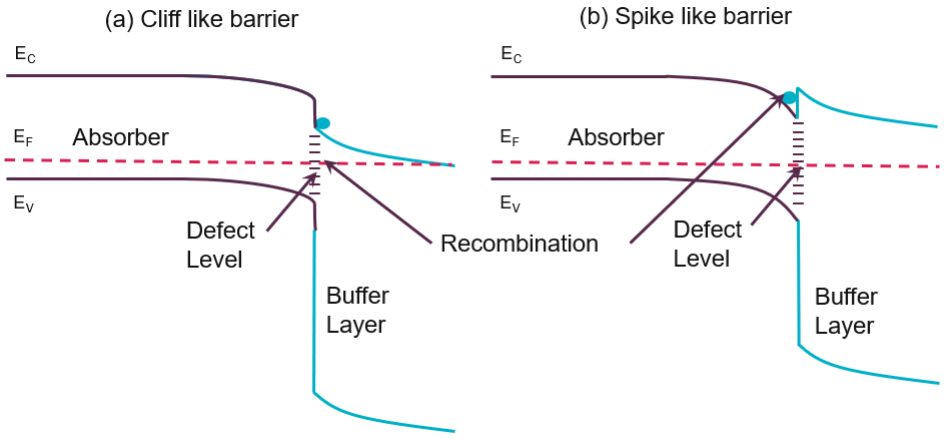

Figure 2.11: Schematic of CBO (a) Cliff formation when CBM of absorber is higher than the buffer layer (negative CBO) (b) Spike like formation when CBM of absorber is lower than the CBM of the buffer layer (positive CBO) [10].

spike and cliff formation and the recombination centers. The cliff formation acts as a recombination center making the activation energy of the dominant recombination less than the bulk bandgap leading to loss of QFL [59]. The spike forms a small electrical barrier but does not impede the transport of the injected electrons nor reduce V_{OC}, provided the offset is less than 0.4 eV [10] [60]. In general, the absorber/buffer interface shows excellent performance when there is a spike formation with positive CBO in the range of 0 to 0.4 eV. Between a CdS buffer and CIGSe absorber, there is low conduction band offset resulting in no barriers at the interfaces aiding in high-efficiency CIGSe devices. However, in the case of high bandgap chalcopyrite CIGSu devices, CdS fails at providing good CBO i.e., results in negative CBO leading to interface recombination (Fig. 2.11 (a)). Therefore, alternatives to CdS for the wide bandgap chalcopyrite absorbers to form positive CBO (Fig. 2.11 (b)) are needed to obtain better performing devices

Transparent Oxides as Buffer Layers

Several Cd-free buffer layers have been investigated over the past decades such as In_2S_3, ZnS, Zn(O,S), $Zn_{1-x}Mg_xO$, ZnSe, ZTO etc. [11] [35] [61]. Trans-

parent oxides with their wide bandgap (≥3.3 eV) make a great choice of buffers for chalcopyrite absorbers, in particular, ternary-zinc-containing oxides are appealing transparent oxide materials for buffer layers with their tunable optical and electrical properties: $Zn_{1-x}Mg_xO$ [62] [36], ZTO [15], ZnTiO [12]. The various Cd-free buffer layers grown over CIGSe solar cells and the maximum power conversion efficiencies observed are shown in Fig. 2.12; it should be noted that the absorber quality across the various reports are very different [11] [12] [13] [14] [15] [16] [17].

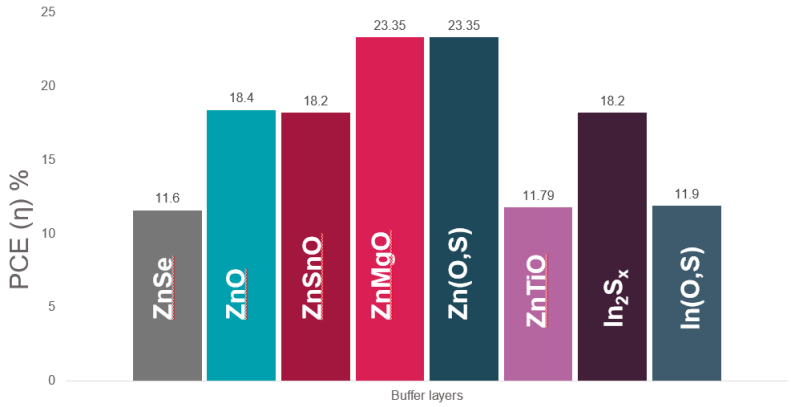

Figure 2.12: Various Cd-free alternative buffer layers grown on CIGSe based thin film solar cells with highest PCEs achieved with them [11] [12] [13] [14] [15] [16] [17].

Various deposition techniques were explored in the use of above materials as buffers for CIGS solar cells such as chemical bath deposition (CBD), atomic layer deposition (ALD), sputtering and evaporation (PVD) etc. [35]. Achieving a buffer layer with small positive conduction band offset requires the ability to fine tune the composition and in turn the position of the conduction band. Among the various techniques, ALD offers an exceptional compositional control of the deposited thin films which is a great advantage to achieve optimal band alignment. In addition, it offers conformal, low-temperature growth which reduces formation of defects at the interface and degradation of the absorber layer during buffer growth. With its layer-by-layer growth kinetics, ALD allows precise control of thickness suitable for deposition of thin buffer layers. Therefore it becomes essential to understand band gap engineering of transparent semiconducting oxides by ALD. Off the above transparent oxides, in this thesis we investigate zinc magnesium oxide and zinc tin oxide.

Zinc Magnesium Oxide

Tinc magnesium oxide (ZMO), $Zn_{1-x}Mg_xO$ is a wide bandgap n-type semiconducting material that shows a tuneable bandgap from 3.3 eV up to ∼4 eV with addition of Mg (up to $x = 0.4$) making it well-suited as buffer layer for wide bandgap chalopyrite absorbers (CIGSu) [28]. The blue shift of the conduction band with addition of Mg provides appropriate band alignment and CBO with CIGSu absorbers accomplishing high efficiencies. X-ray photoelectron spectroscopy study on the small valence band offsets of non-polar ZnO/$Zn_{1-x}Mg_xO$ heterojunctions shows in Fig.2.13 the conduction band minimum shifting linearly upward with increase in Mg content [18]. Initially, Cd-free $Zn_{1-x}Mg_xO$ buffer layers were deposited by sputtering on CIGSe absorbers resulting in efficiencies upto 16%[63]. $Zn_{1-x}Mg_xO$ was commonly used as an intermediate buffer along with Zn(O,S) or CdS or deposited post Cd treatment[64] [65]. Even the record high efficiencies of over 23.35% obtained with CIGSSe solar cells employed a double buffer layer involving Zn(O,S) and $Zn_{1-x}Mg_xO$ [16]. To avoid sputter damage and perform a direct deposition of $Zn_{1-x}Mg_xO$ based buffer layers Torndahl et al. adopted atomic layer deposition, achieving efficiency of 14% [36]. The lower efficiency was attributed to lower V_{OC} and poor fill factor due to positive conduction band offset(≥0.3 eV) resulting in an electrical barrier [66]. Optimized ALD processes improved the efficiencies to ∼16% and it was noted that higher temperature of atomic layer deposition resulted in degradation of the device performance and a ratio of 1:6 Zn:Mg resulted in the best efficiency [36] [67]. Thus, numerous studies investigated the use of $Zn_{1-x}Mg_xO$ buffer layers for CIGSe solar cells [68] [69]. A key advantage of $Zn_{1-x}Mg_xO$ buffer layer is

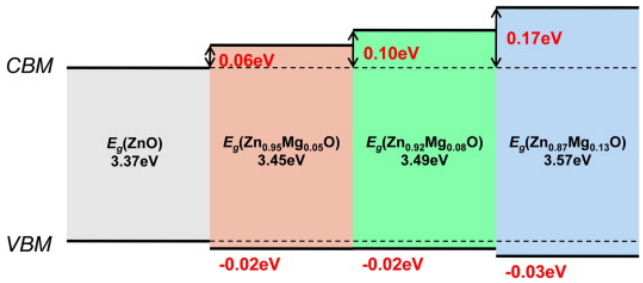

Figure 2.13: Schematic band alignment in non-polarZnO/$Zn_{1-x}Mg_xO$ heterojunctions [18].

that, with its widely tuneable bandgap it is not only suited for CIGSe solar cells but also the high bandgap CIGSu absorbers. However, detailed study of $Zn_{1-x}Mg_xO$ buffers and their band alignment with CIGSu is lacking.

2.2.2 Thin-film Transistors

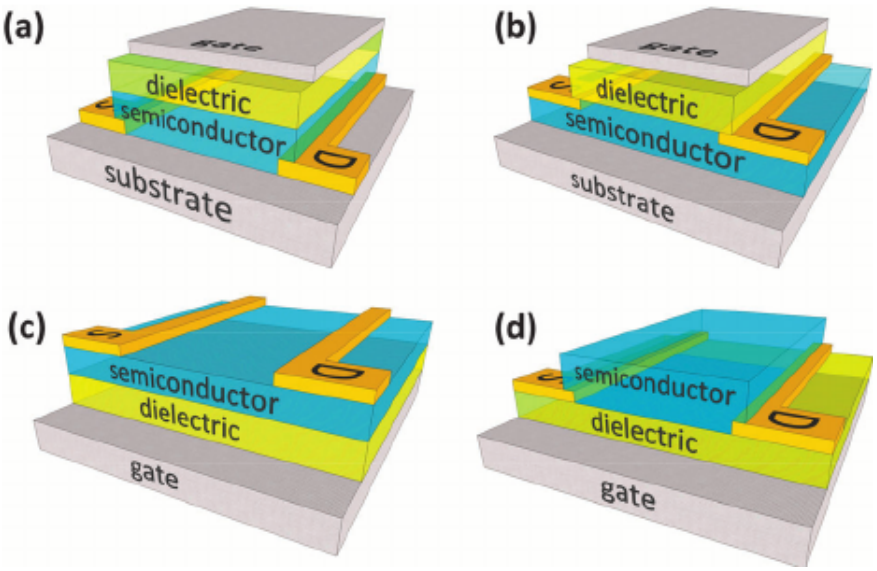

Figure 2.14: (a) Staggered, top-gate TFT; (b) Coplanar, top-gate TFT; (c) Staggered, bottom-gate TFT; and, (d) Coplanar, bottom-gate. [19]

Thin-film transistors or TFTs are a type of field-effect transistor (FET) that form the backbone of display technology and used in modern televisions, computers, mobile and various consumer electronics. The structure of a basic TFT consists of a semiconducting channel layer and a gate electrode separated by an insulating dielectric layer. In addition, two metallic electrodes, the source and drain provide electrical contact with the semiconducting layer. The basic working principle involves controlling the conductivity of the semiconductor layer through the application of an external electric field on the gate electrode. One of the key differences between a TFT and a traditional FET is the thickness of the channel or active layer. In the former, the semiconducting layer is thin, fabricated using thin-film deposition techniques whereas latter FET employs a bulk semiconductor. Another key working difference is that an FET works by creating a channel inside the bulk semiconductor between the source and drain metal contacts when a field is applied through the gate. But in a TFT, the thin semiconducting layer acts as the channel. The various TFT device architectures are shown in figure below.

Zinc Tin Oxide

Transparent semiconductors, especially transparent amorphous semiconductors are becoming popular materials for TFT applications due to their high transparency and amorphous nature. Zinc tin oxide has become a popular alternative to the most extensively investigated amorphous oxide semiconductor for TFT applications is indium gallium zinc oxide or IGZO. There exists numerous studies on zinc tin oxide based TFTs using various deposition methods, however investigations on atomic layer deposited zinc tin oxide as channel layer for TFT is still lacking given the advantages of ALD in controlling the composition of the materials. Only very few papers investigated the use of ALD based ZTO as TFTs so far [70] [71] [72] [73] [74] [75].

2.3 Atomic layer deposition

Atomic layer deposition (ALD) is type of chemical vapour deposition technique developed in the 60s and 70s to fabricate thin-films. It involves the use of gas-phase chemicals called precursors(reactants) which react with each other or with co-reactants such as water, O_2 or N_2 plasma at the surface of the substrate to produce a film. ALD is a sequential deposition technique, that relies on the precursors reacting with the surface in a self-limiting way and cyclic exposure of the surface to the precursors, through which a layer-by-layer linear growth of thin-films is attained. Since the growth depends on the number of cyclic steps rather than the precursor dosage/flux, high degree of conformality and thickness control can be realized with ALD. CMOS technology saw the prevalent use of ALD in the deposition of high-k dielectric metal oxides. Metal oxide binary ALD process have been commonly used in the industry for optical and protective coatings.

A binary ALD process consists of a precursor dose wherein the precursor is pulsed first followed by co-reactant dose. The pulse time of the precursor dose should be sufficient enough for the precursor to be absorbed at the entirety of the substrate surface, see Fig.2.15, and the co-reactant pulse time should be enough for a complete reaction with the precursor. A purge step follows each dose steps to remove excess precursor/reactants. The common co-reactants for metal oxides are H_2O, O_2 plasma and ozone, N_2 plasma and ammonia for metal nitrides and H_2S is employed for metal sulfides. Precursors are the key element in ALD as they govern the self-limitation principle and are required to be volatile and not decomposable thermally during processing. While the precursors can be inorganic or metalorganic, the latter is typically opted. Organometallic compounds including alklys,

alkoxides, cyclopentadienyls etc., containing the desired metal or semimetal that need to be deposited are used as precursors; typical inorganic precursors involve metal halides.

As an example of a binary metal oxide ALD process, we present the case of ZnO ALD process. A typical binary ALD process involved in the growth of zinc oxide films is illustrated in Fig.2.15. Diethyl zinc (DEZ) and H_2O are the precursor and co-reactant used respectively.

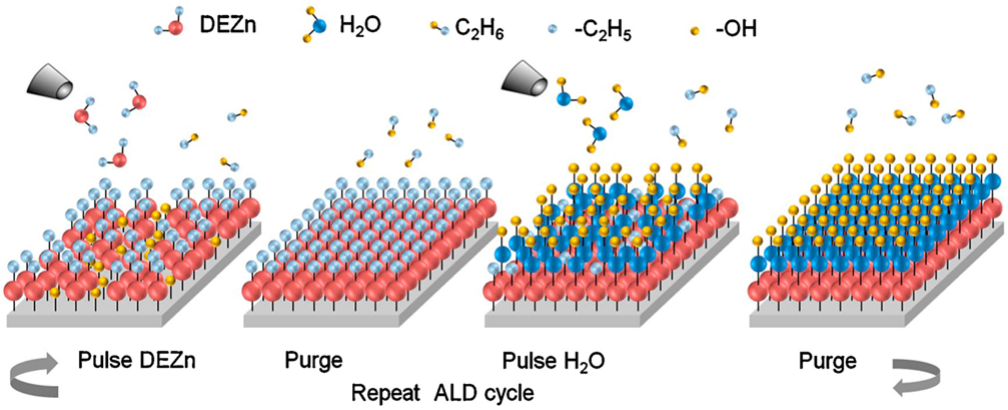

Figure 2.15: A schematic diagram of an atomic layer deposition process reaction cycle to grow ZnO films [20].

The single reaction cycle of ZnO ALD process is described in the following steps

Step 1: **Pulse DEZ - Adsorption**
When the precursor is pulsed, it reacts with the hydroxyls at the substrate surface ($-$OH), diethyl zinc forms monoethyl zinc, releasing ethane. If $|$ indicates the substrate, then
$Zn(C_2H_5)_2 + |{-}OH \rightarrow |{-}O - Zn(C_2H_5) + C_2H_6$

Step 2: **Purge**
Purge step involves passing nitrogen or argon gas to remove unreacted excess DEZ and byproducts.

Step 3: **Pulse Water - Oxidation**
The water pulsed reacts with precursor molecules that have been adsorbed at the substrate surface leaving a ($-$OH) tail which serves

as a adsorption reaction site for the next cycle of reaction.
$|-O-Zn(C_2H_5) + H_2O \rightarrow |-O-Zn-OH + C_2H_6$

Step 4: **Purge**
A purge step again with inert gas removes excess water and reaction byproducts.

Note that the monoethyl zinc may also react with remaining hydroxyl groups to form elemental Zn, these other reactions are minor and negligible. Combining the half-reactions at Steps 1 and 3, the net reaction involved in a single ZnO ALD cycle is thus,

$$Zn(C_2H_5)_2 + H_2O \rightarrow ZnO + 2.C_2H_6 \tag{2.10}$$

From the above steps, it is evident that the presence of surface hydroxyls at the substrate surface is crucial for starting this ALD process as they serve as reaction sites for chemisorption. Irreversible chemisorption is the preferred method of adsorption in ALD otherwise the adsorbed precursor molecules might be desorbed and taken away during purge step. Lack of adequate reaction sites might impact the ALD growth, therefore hydroxylation of the substrate surface should be carried out prior to initiating an ALD process by pre-treating the substrate or by simply exposing the substrate to a water pulse before. The above 4 steps which form a single ALD reaction cycle deposits a small amount of thin-film of the order of few ångstroms on the surface of the substrate which is defined as growth per cycle or GPC. The above reaction cycle (steps 1 til 4) is repeated over and over until growth of the film reaches the thickness desired. GPC usually given in nm/cycle or Å/cycle can be determined as,

$$\text{Growth per cycle, GPC } = \frac{\text{Thickness of film}}{\text{No. of cycles}}. \tag{2.11}$$

The self-limiting characteristic of ALD arises from the availability of finite reaction sites at a given surface for the precursor. While initially, the precursor reacts with the surface of the substrate, in subsequent reaction cycles, the precursor reacts with the surface of the material deposited. Saturation occurs when the surface is saturated with precursor molecules, i.e, the pulse time is sufficient enough for the precursor to be adsorbed at all the available reactive surface sites. This leads to a self-limited reaction as there are no more unreactive sites for further reaction and the GPC reaches steady-state at this juncture. Once saturation is achieved, growth remains unaffected with further increase of the dosage or pulse time. Ideally, in a saturated, self-limited ALD process, one reaction cycle (steps 1 til 4) is expected to

deposit one monolayer of the material onto the substrate. However, it is not often the case and the GPC is restricted to sub-monolayer growth. Knowledge of the growth kinetics of an ALD process becomes highly relevant to understand the factors that limit the growth to less than one monolayer per cycle.

2.3.1 Growth Kinetics of Binary ALD Processes

Self-limited saturated growth, a distinctive temperature window and linearity are three essential characteristics that are hallmarks of a true ALD process. The forthright parameter that influences characteristics of an ALD process is the deposition temperature.

ALD Temperature Window: The deposition temperature has a stark

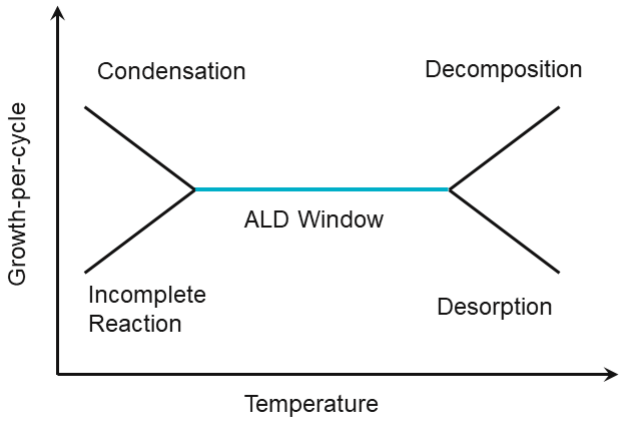

Figure 2.16: Schematic of thermal ALD window: The Growth per cycle (GPC) versus deposition temperature depicts various possible behaviours and regimes.

effect on the growth through the number of reaction sites available at the surface, the way the precursor reacts before and after chemisorption. The deposition temperature range in which self-controlled reaction remains feasible and a consistent growth takes place resulting in uniform thin-film deposition is defined as the *ALD temperature window*. Outside of the temperature window, non-ideal growth behaviour is observed. If the temperature is less than the thermal activation energy of the precursors, then not enough precursors are chemisorbed at the reaction site resulting in poor growth, on the other hand growth might also increase due to condensation of precursors as physisoprtion dominates at lower temperatures. The two regimes are depicted

in Fig. 2.16. Outside of the ALD window, higher temperatures can cause the absorbed precursor species to desorb diminishing the growth. Higher temperatures can also result in a CVD type behaviour, where the adsorbed precursor decomposes and additional precursor species get adsorbed causing a non-linear growth GPC spurt. Moreover, GPC can change through the ALD window, it may increase, decrease or remain constant with temperature correspondingly brought by an increase, decrease or unaffected number of reaction sites at the surface respectively. The number of reaction sites can also become limited due to steric hindrances arising from the ligands of the metalorganic precursors adsorbed at the surface which hide the other available unreacted sites to chemisorption. The larger the precursor ligand, the higher is the steric hindrance effect.

Linearity: Ideally, the GPC should remain constant throughout the ALD process with the thickness of deposited material scaling linearly with respect to the number of sequential cycles. However, while the first ALD reaction cycle occurs at the surface of the substrate, the subsequent reaction cycles occur at the surface of the material deposited onto the substrate and so on. As the nature of the surface vary, the chemical composition, number of reaction sites etc., GPC also varies. Depending on how GPC varies with number of reaction cycles, ALD processes can be categorized into following types as represented in Fig. 2.17,

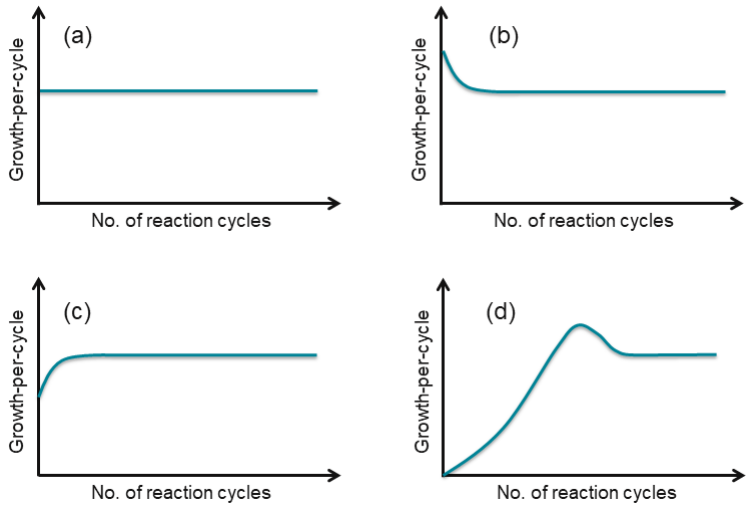

Figure 2.17: Various types of ALD processes (a) Linear growth (b) Substrate-enhanced growth (c) Substrate-inhibited growth Type 1 (d) Substrate-inhibited growth Type 2 [21].

(a) Linear growth: GPC remains constant with number of cycles

(b) Substrate-enhanced growth: GPC is higher initially and settles down to a constant steady-state value which can be attributed to the higher number of reaction sites available at the substrate than the deposited material.

(c) Substrate-inhibited growth: When the opposite to the above happens, here the substrate provides less number of reaction sites and therefore inhibits the growth of material. After subsequent cycles, the deposited material improves the number of reaction sites available bringing the GPC up to a steady-state resulting in a substrate-inhibited growth of Type 1. Another type of this growth involves island growths which causes the GPC to attain a maximum and then arrive at a lower stead-state value (d).

In addition, the manner in which the material grows on the surface can also influence the GPC. For a growth of one monolayer per cycle, a two-dimenstional growth mode is preferred where each half-cycle fills the lowest unreacted or unfilled gap and the material covers the surface of the substrate completely. Conversely island growths or randomized growths can also occur.

Understanding the growth kinetics gets even more interesting and challenging when two or more binary ALD process are involved in material synthesis.

2.3.2 Synthesis of ternary transparent oxides

Atomic layer deposition is a versatile process which facilitates the doping, synthesis of ternary and quaternary materials. Doping and synthesis of transparent metal oxides becomes easier with the compositional tuning offered by ALD. Several different approaches are offered by ALD to grow ternary films such as supercycle approach, co-dosing approach, multicomponent precursor approach and multicomponent co-reactant approach shown in Fig. 2.18. The supercycle approach involves the use of two or more binary ALD processes alternated to achieve the desired material, meanwhile a co-dosing approach involves alternate dosing of precursors simultaneously (b). Multiconstituent or multicomponent precursor approach involves the synthesis of material with fixed composition using precursor molecules that contain multiple metal or non-metal components. Multiconstituent co-reactant approach employs a co-reactant that becomes acts as both a oxygen and metal source for a metal oxide deposition.

Out of the various approaches, the popular and commonly used one is the

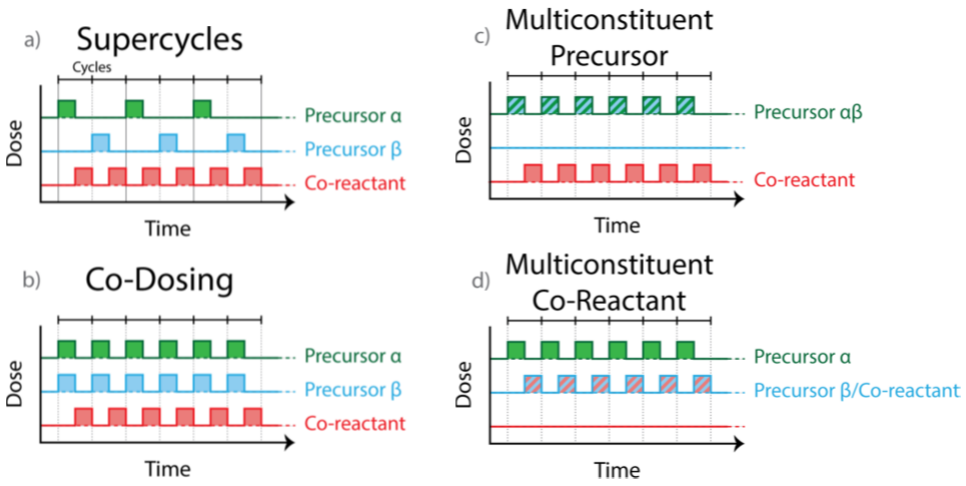

Figure 2.18: Overview of approaches that have been explored for the synthesis of ternary films by ALD. (a) The supercycle approach, (b) Co-dosing, (c) Multiconstituent precursor approach, and (d) a multiconstituent co-reactant approach [22]

supercycle approach, where compositional tuning becomes straightforward. One reaction cycle of a binary process is shown in Fig. 2.15, combining and alternating it with another binary reaction cycle is called *supercycle*. Growing a binary material or metal oxide involves repetition of the reaction cycle, similarly growing a ternary material of desired thickness involves repetition of the supercycle. The two or more binary ALD process combined into a supercycle are expected to use the same co-reactants. The composition and doping can be simply varied by varying the relative number of binary processes within a supercycle. Thus using this approach a homogeneous, multilayer or doped ternary material can be synthesized as illustrated in Fig. 2.19. The relative number or ratio of binary processes is called the cycle ratio or pulse ratio and is key parameter of concern in compositional tuning. If there are Z number of binary metal oxide processes of AO_x and W number of BO_y processes within a supercylce, then a ternary film AB_qO_v is grown with a pulse ratio (PR) written as

$$\mathrm{PR} = \frac{\mathrm{W}}{\mathrm{Z}+\mathrm{W}} \quad \text{and} \quad \mathrm{BP} = \mathrm{Z}+\mathrm{W} \tag{2.12}$$

In addition to the pulse ratio, bilayer period (BP) is another relevant supercycle parameter involved in compositional tuning. It is the total number of reaction cycles within a supercycle. More clearly, the bilayer period is

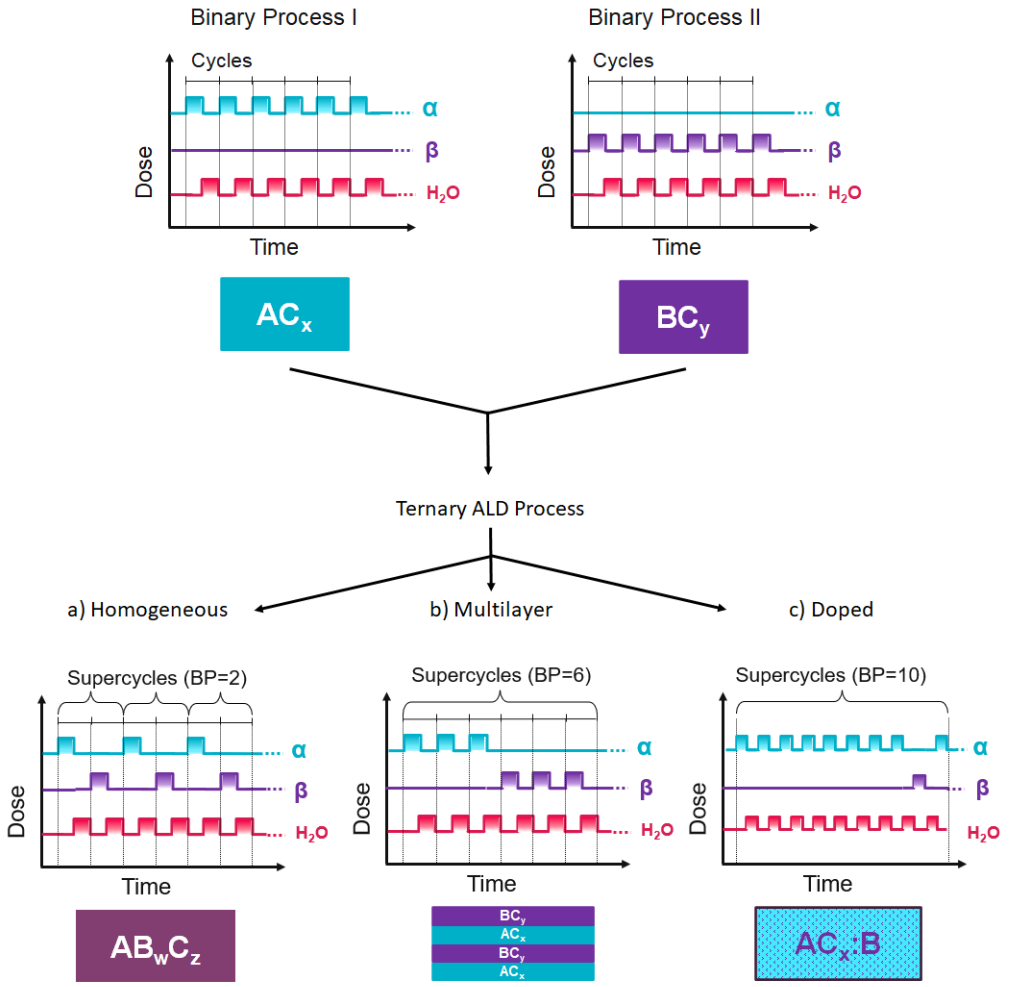

Figure 2.19: The supercycle approach, combining binary process I with precursor α and II with precursor β into a ternary process. H_2O is used as a co-reactant example. (a) Homogeneous material is obtained if bilayer period is small, here BP=2 for 50% mixture. (b) For the same 50% mixture a multilayer is formed for a large bilayer period BP$\geq$2, here the bilayer period is 6. (c) A doped material is deposited if the pulse ratio is $\leq$ 0.1 i.e less than 10% [22].

defined as the average number of individual cycles contained in a supercycle that is repeated to deposit desired thickness of the mixed material, i.e. average number of Z+W.

Depending on the combination of the binary processes AO_x and BO_y, a ho-

mogeneous ternary film or a doped ternary film or a multilayered material can be obtained as illustrated in the figure 2.19. If the pulse ratio is much smaller than 0.1, it results in a doped material, for example introducing a little amount of say 1 cycle of BO_y into the host metal oxide AO_x of 9 cycles one would expect a doped $A_{0.9}B_{0.1}O_x$ film with a pulse ratio of 0.1. Now, whether a homogeneous or multilayer ternary material is obtained depends on the bilayer period, a bilayer period of less than 2 results in the former. Ideally, following the rule of mixtures, the growth rate (GPC) and composition of the ternary material should be a linear combination of the growth rate and composition of the binary processes involved in the supercycle. On the contrary, the composition often deviates from the targeted composition and the growth deviates from that of the binary processes. Nucleation effects, interaction between precursor ligands and interplay between the binary material interfaces are some of the causes of such non-ideal behavior. Therefore, it becomes a very necessity to investigate the growth kinetics of ternary processes in detail to achieve good control of the composition and properties of the material.

For two binary material to be mixed together to form a ternary material, the ALD temperature window of the binary processes must overlap.

Growth Kinetics of Ternary ALD Processes

If g_a and g_b are the growth rates of binary processes a and b that are alternated in a supercycle to grow a ternary metal oxide, then the growth per supercycle would be $g_s = PR_a.g_a + PR_b.g_b$. If Z and W are the number of cycles of processes 1 and 2 respectively within the supercycle, then the growth per cycle of the ternary film is defined as,

$$GPC_{ab} = \frac{g_a.Z + g_b.W}{Z + W} = (1 - PR_b).g_a + PR_b.g_b \tag{2.13}$$

Similarly if ρ_a and ρ_b are the densities of the binary films, then the atomic composition of material B is given as,

$$\frac{[B]}{[A] + [B]} = \frac{\rho_b g_b.W}{\rho_a g_a.Z + \rho_b g_b.W} \tag{2.14}$$

Challenges arise from intermixing of two binary materials such as precursor mismatch, etching effect of precursors, nucleation effects etc., therefore care needs to be taken to understand and address the nature of growth of ternary materials to achieve desirable properties through a reproduceable ternary ALD process.

Case of Ternary ALD: Zinc Magnesium Oxide

Törndhal et al. were the first to establish an atomic layer deposition process for zinc magnesium oxide(ZMO) films in the context of buffer layers for CIGS solar cells, and followed up with a study on the effect of deposition temperature of the ALD grown ZMO buffers [36] [76]. They found a linear increase in composition and bandgap (from 3.3 to 3.8 eV) with respect to pulse ratio and formation of two-phase regions beyond a concentration of 20% [36]. Studies focused either on film characterization or improved solar cell performance. Luka et al. investigated the doping of ZMO films with aluminium to increase the carrier concentration and conductivity; the ratio of Al to Zn was kept constant while Zn to Mg was varied making it Mg doping of AZO [77]. Epitaxial growth of MgO and ZnMgO by ALD was also investigated by using suitable substrates [78]. Only two studies focused on the growth kinetics of the atomic layer deposition of ZMO process, the low energy ion scattering investigation assessed that the incorporation of Mg dramatically reduces the growth rate of ZnO [79]. The study by Peng et al. for the first time established a structure-property-synthesis relationship in the atomic layer deposition of zinc magnesium oxide by performing in-situ quartz crystal microbalance [26]. They found that depending on the deposition temperature, ZnO growth is enhanced or inhibited by MgO at 200 ° and 120 ° respectively. In addition, the lower temperature lead to a two-phase region and the bandgap varied linearly with composition [26]. Still a clear model to tune the bandgap and conductivity of the transparent semiconducting oxide is lacking.

In this thesis, we aim to present clear model to achieve a reprodoceable thermal ALD process, address the optimal way of mixing binary materials to arrive at the ternary material, ZMO - tune its optical and electrical properties at lower temperatures which is essential for photovoltaic applications.

Case of Ternary ALD: Zinc Tin Oxide

Several studies investigated the growth and mixing of ZnO and SnO_x by atomic layer deposition owing to their successful application as buffer layers in CIGS based solar cells. The first atomic layer deposited zinc tin oxide films were successfully grown by Choi et.al at 150 °C [80]. A detailed investigation of their electronic structure was carried out using soft x-ray spectroscopy followed by the evaluation of ALD grown ZTO in metal-oxide solar cells and as buffer layers for CIGS solar cells [81] [82] [83] [84]. Right after, the amorphous oxide thin film transistors saw the use of ALD-grown ZTO as channel layers [70]. The first elaborate investigation of atomic layer deposited ZTO films

were carried out by Mullings et al. [85], which shed light on the relationship between the supercycle parameters and the growth characteristics, and optical properties. Although the study was the first in probing the effect of bilayer period on the growth of ZTO films, it lacked detailed investigation on the effect of bilayer period over the electrical and optical properties of the materials. Mullings et al. reported ZnO growth rates reduced after SnO_x ALD cycle and at higher Sn ratios, mixing small number of ZnO into SnO_x reduced Sn incorporation[85]. Soon, a follow-up study with in-situ QCM by Tanskanen et al., confirmed that indeed a single SnO_x ALD cycle on ZnO was enough to reduce the reaction site density [86]. Lindahl et al. established the effect of deposition temperature on the Sn content to be small and correlated the growth, structure and optical properties of ZTO thin films to the deposition temperature [87]. They attributed the effect of temperature on bandgap to the presence of small ZnO and ZnO(Sn) crystallites during growth [87]. Investigation of growth and intermixing of zinc tin oxide at smaller bilayer periods revealed that ZnO follows a substrate-inhibited growth behaviour on SnO_x [37], additionally, FTIR spectrocopy studies revealed that TDMASn ligands are not eliminated completely after SnO_x ALD cycle causing reduced growth [88]. The most recent study attempted to predict and model the non-linear growth of ZTO by ALD by considering island-type growth behaviour [89]. Although the study predicted growth rates in good agreement with experimental values, it did not treat compositional variations clearly. In addition, several studies explored ALD growth of ZTO with different tin precursors(TET - tetraethyltin), different co-reactants (ozone and hydrogen peroxide) and plasma enhanced ALD [90] [91] [92] [75].While there are quite a few studies focused on the growth kinetics of zinc tin oxide, a comprehensive study on the effect of the process parameters such as supercycle ratio, bilayer period, deposition temperature on the growth, composition and the material properties is still lacking. Most studies paid particular attention to either the growth characteristics or the material properties, the former is very relevant to applications that are process temperature sensitive. Thus, a detailed investigation of the growth kinetics becomes a necessity to establish a reliable and reproduce-able ALD based ZTO process.

In terms of the material properties, previous literature specifically targeted either optical properties relevant for solar cell applications or electrical properties required for TFT devices and none altogether. The first report to look into the optical properties involved soft x-ray absorption and emission spectroscopy studies which found the bandgap to vary from 3.3 eV of ZnO to 2.2 eV of SnO_x [82]. The variation of bandgap was attributed to shift in valence band to higher energies, additionally the non-linear trend ob-

served in the bandgap was ascribed to a moderate shift in conduction band edge which decreases with increase in Sn content [82]. Observation of a non-trivial dependence of bandgap with Sn content and arguments over the bandgap whether to fit using a direct or indirect model were the focus of earlier studies [85] [87]. Lindhal et. al extended their study to deposition temperature induced conduction band changes in CIGS solar cells and found at low deposition temperatures the conduction band minimum is so high it leads to a barrier but with increase in temperature the conduction band minimum lowers resulting in favourable conduction band offset and desirable efficiencies[15]. We infer from the previous study that conduction band edge decreases in energy with increase in deposition temperature. A lot of the reports argued that the non-trivial dependence of bandgap with composition arises out of the microstructural changes in the material and also the issue of the bandgap type as the ALD deposited ZTO thin films were amorphous [87] [93]. Also, XANES studies addressed the amorphous nature of the films and found that both annealing and composition can be used to tune conduction band minimum[94].

Research on ALD deposited ZTO channel layers for TFT focused on the electrical properties, Ahn et al., found that annealing decreases the carrier concentration resulting in a conductor to semiconductor transition. mobilities and were probed aommunity tried to anneal the ZTO films and understand the semiconductor to conductor transition. Lower Sn content and annealing have been established to result in semiconducting properties leading to good field-effect mobility[72].

Therefore, in this thesis we make an effort to address structure-process-property relationship of ZTO by varying deposition temperature, bilayer period, supercycle ratio and understanding their effects on both electrical and optical properties. Bilayer period in particular is an interesting process parameter which is not expected to alter the composition, still can be used to tune the material properties.

Chapter 3

Experimental Methods

3.1 Thin-film Deposition by ALD

Atomic layer deposition of the ternary films $Zn_{1-x}Mg_xO$ and ZTO (ZMO and ZTO, respectively) are carried out in Beneq TFS 500 reactor. 95% Diethylzinc [$Zn(C_5H_5)_2$ or DEZ] is the precursor used for growing ZnO with deionized water acting as a co-reactant. All the ALD processes, ZnO, MgO and SnO_x use H_2O as co-reactant/oxidant. The precursor employed for MgO is bis-cyclopentadienyl magnesium [$Mg(C_2H_5)_2$] or (99.99+%-Mg) PURATREM $MgCp_2$ from STREM chemicals. The precursor used for and SnO_x: Tetrakis(dimethylamino)tin(IV) or (99.99%-Sn) PURATREM from STREM chemicals TDMASn respectively. All the process utilized Argon as carrier gas.

3.1.1 Substrates

For both ZTO and ZMO thin films, the substrates used are: 525 $\pm$ 25 μm thick 4-inch $\langle 100 \rangle$ oriented P/B doped Si wafers and 25x25 cm^2 thick UV-quality optical quartz glass with transmission T$\geq$80%. In addition, for TFT device fabrication, several different substrates are tested: SiO_2 coated doped ($\rho \leq 0.05\Omega$-cm) Si wafers 3-inch, FTO coated glass substrates and heavily doped ($\rho \leq 0.001\Omega$-cm) 4-inch Si wafers.

3.1.2 Atomic layer deposition of ZMO thin films

For the deposition of ZMO, the solid precursor $MgCp_2$ is heated to 80°C in a hot source. With an Argon flow of 250 sccm, the pulse and purge times are

Recipe	Precursor Pulse	Purge	Co-reactant Pulse	Purge
ZnO	200ms DEZ	5s Ar	200ms H_2O	5s Ar
MgO	4s $MgCp_2$	5s Ar	200ms H_2O	5s Ar

Table 3.1: Pulse-purge sequence and optimized times of ZnO and MgO

optimized to achieve a self-limited ALD process and the sequence is detailed in table 3.1. The vapour pressure of the precursor $MgCp_2$ is 0.042 hPa, hence the vapour pressure inside the canister will be insufficient to reach the chamber swiftly. We employ a push gas maneuver to draw the precursor into the reaction chamber by first opening the carrier gas for 0.5s and waiting for 50ms such that the vapour pressure inside the canister increases. After, we simultaneously open precursor valve and carrier gas valve for 4s to let the precursor into the reaction chamber. Care should be taken to avoid cold spots between the hot source precursor valves and the reaction chamber, otherwise condensation occurs resulting in blockage of the precursor lines.

We mix the ZnO and MgO binary processes into a supercycle to grow $Zn_{1-x}Mg_xO$. We vary the pulse ratio from 0 till 0.4 as the ZMO films with lower composition are of more interest for application as buffer layers in solar cells. We synthesize ZMO films at three different deposition temperatures, 130 °C, 150 °C and 180 °C. ZnO ALD window varies from 70 to 250°C [95]. Although the ALD temperature window of MgO has been reported to span from 80 °C to 400 °C [96] [97], we attained saturation and uniform coverage over 12-inch silicon substrate only above 120 °C. Additionally, the composition of ZMO films are also varied using bilayer period (BP) as illustrated in Fig. 3.1 for a pulse ratio of 0.3.

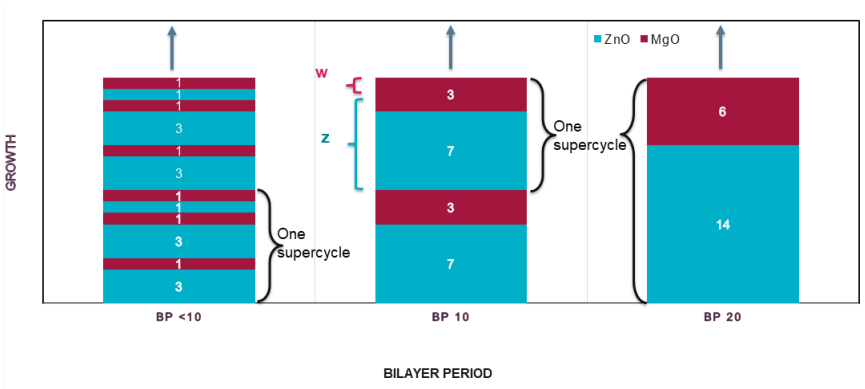

Figure 3.1: Supercycles of $Zn_{1-x}Mg_xO$ for ratio of 0.3 at various bilayer periods from the smallest ($\leq$10) to 20, the arrows point direction of growth.

Pulse Ratio	BP<10	BP = 10	BP = 20	BP = 40	BP = 60
0.1		9 ZnO 1 MgO			
0.2	4 ZnO 1 MgO	8 ZnO 2 MgO	16 ZnO 4 MgO	32 ZnO 8 MgO	44 ZnO 16 MgO
0.25	3 ZnO 1 MgO	6 ZnO 2 MgO	15 ZnO 5 MgO		
0.285		5 ZnO 2 MgO	15 ZnO 6 MgO		
0.3	3 ZnO 1 MgO 3 ZnO 1 MgO 1 ZnO 1 MgO	7 ZnO 3 MgO	14 ZnO 6 MgO	28 ZnO 12 MgO	42 ZnO 18 MgO
0.4	3 ZnO 2 MgO	6 ZnO 4 MgO			

Table 3.2: Ratio of ZnO and MgO mixed into a supercycle for different bilayer periods

The smallest bilayer period ($\leq$10) for the pulse ratio of 0.3 involves the following: 3 ZnO cycles, 1 MgO cycle, 3 ZnO cycles, 1 MgO cycles, 1 ZnO cycle and 1 MgO cycle. This way the MgO cycles are well dispersed into the ZnO cycles and the supercycle is repeated number of times to get desired thickness. The bilayer period of 10 for pulse ratio 0.3 involves 7 consecutive ZnO cycles and 3 MgO cycles into a supercycle. The various combinations of bilayer period for pulse ratios 0.2 and 0.3 are tabulated in 3.2. Note, for the pulse ratio of 0.1, the smallest bilayer period would be 10 as only one MgO cycle is added for every 9 ZnO cycles. The growth per supercycle of ZMO is calculated from (2.13) and the supercycles are repeated enough times to $\sim$100 nm thick ZMO films. All the depositions are carried under high vacuum.

For the deposition of ZMO thin films as buffer layers for$Cu(In, Ga)S_2$ solar cells, the choice of pulse ratio, temperature and bilayer period are made based on the optical properties observed in the ZMO films.

3.1.3 Atomic layer deposition of ZTO thin films

The deposition of ZTO carried out with TDMASn, 1s pulse time. For the recipes at high flow rate of 250 sccm, a push gas recipe similar to the case of Mg precursor is followed with the pulse time of TDMASn being 1s. The vapour pressure of TDMASn is 15 hPa at room temperature. Direct pulsing is opposite to a push gas maneuver and involves just opening of the hot-source precursor valves. The low flow recipe at 50 sccm, push gas and direct pulsing resulted in the same growth rate and is ascribed to the fact that at a lower

Bilayer Period	BP<10	BP = 10	BP = 20	BP = 40	BP = 60
0.1		9 ZnO 1 SnO_x		36 ZnO 4 SnO_x	
0.2		8 ZnO 2 SnO_x		32 ZnO 8 SnO_x	
0.25	3 ZnO 1 SnO_x	6 ZnO 2 SnO_x	15 ZnO 5 SnO_x	30 ZnO 10 SnO_x	60 ZnO 40 SnO_x
0.3	3 ZnO 1 SnO_x 3 ZnO 1 SnO_x 1 ZnO 1 SnO_x	7 ZnO 3 SnO_x	14 ZnO 6 SnO_x	28 ZnO 12 SnO_x	
0.4		6 ZnO 4 SnO_x		24 ZnO 16 SnO_x	

Table 3.3: Ratio of ZnO and SnO_x mixed into a supercycle for different pulse ratios at bilayer period 10 and 40 at 150°C

flow rate, the vapour pressure inside the hot source precursor is sufficient enough to saturate the substrate surface; the optimized pulse time for the Sn precursor remains at 1s. The hot source temperature varied from 55°C to 80°C. ZTO films were grown at deposition temperatures as low as 80°C. ZTO films were grown at four different deposition temperatures ranging from 80°C to 150°C. In the latter ZTO run, we primarily focus on the ZTO films grown at 150°C.

ZTO films are grown at different pulse ratios for two different bilayer periods as described in table 3.3. ZTO films of different bilayer period are grown at PR 0.25 and 0.3. While the bilayer period variation at PR = 0.3 resembles Fig. 3.1, the change in bilayer period for PR = 0.25 is depicted in Fig. 3.2. The ZTO films grown at different deposition temperatures have a PR of 0.25 at BP 40. The same deposition process is followed for their device application in the fabrication of TFTs, only the thickness of the films vary to achieve devices of varying channel layer thicknesses.

3.2 Thin-film Characterization

The first step in the characterization of ALD grown films involves the determination of thickness to assess the growth rate of the films and is estimated using Ellipsometry. The composition is estimated by performing energy dispersive x-ray spectroscopy. The optical properties are determined using UV-Vis spectroscopy. Structural characterisations involve X-ray diffraction and X-ray reflectometry. We perform X-ray photo-electron spectroscopy (XPS), secondary ion mass spectrometry (SIMS), Transmission electron microscopy

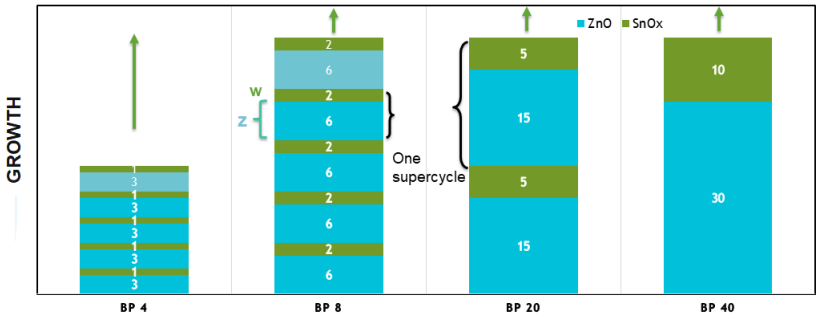

Figure 3.2: Supercycles of ZTO for ratio of 0.25 at various bilayer periods from the smallest 4 to 40, the arrows point toward direction of growth. Process temperature: 150°C

(TEM) for an in-depth analysis of the structure and morphology.

3.2.1 Ellipsometry

Spectroscopic ellipsometry is an optical technique that relies on the polarization of light. This non-invasive, non-contact, model-based approach uses the change in polarization of light as it is transmitted and reflected by thin film or material interface to determine the material properties such as thickness, roughness and optical properties. Light is an electromagnetic wave electric and magnetic fields oscillating perpendicularly to each other. Polarization deals with direction and amplitude of the wave's electric field. If the direction of the electric field is random, then it is called unpolarized light. Linear polarization refers to the oscillation of electric field in a single direction and is obtained by combining orthogonal waves which are in-phase. A linearly polarized light is said to be p-polarized if the electric field is parallel to the plane of incidence (plane normal to the direction of propagation) and s-polarized if the electric field is perpendicular to the direction of propagation. Meanwhile, circular or elliptical polarization involves the rotation of electric field over a plane at a constant rate.

Ellipsometry as the name suggests employs elliptically polarized light which are formed by combining orthogonal waves of arbitrary phase and amplitude. When a linearly polarized light is incident on a thin-film sample, it undergoes reflection resulting in amplitude and phase changes. By breaking the input linear polarized light into its s and p components, the change in phase and

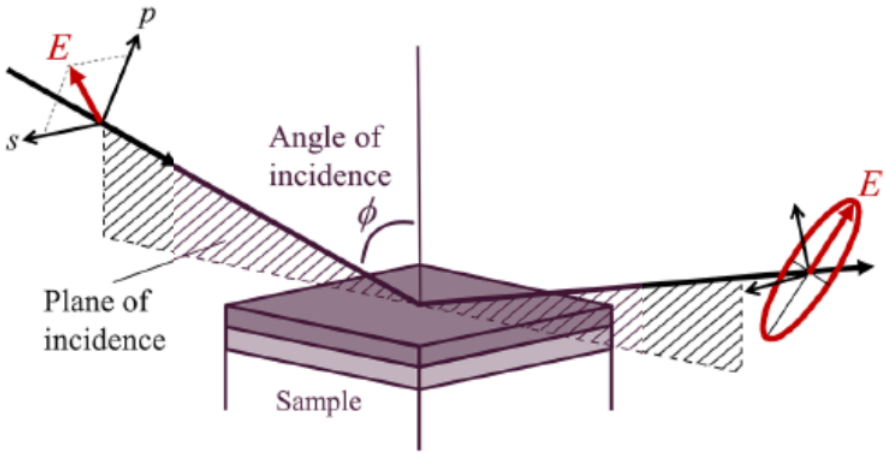

Figure 3.3: Ellipsometry measurement involving incident linearly polarized light with both s and p components. The incident light interacts with the sample and gets reflected leading to a change in amplitude and phase of s- and p-polarizations, producing elliptically polarized light [23].

amplitude between the s and p components upon reflection is determined. The detectors in the ellipsometer thus measure the change in phase, Δ and amplitude, Ψ between the input linearly polarized light and the output elliptically polarization illustrated in Fig. 3.3 [23]. The change in polarization is given by the fundamental equation of ellipsometry as [98],

$$\rho = \tan(\Psi).\Delta = \frac{r_p}{r_s} \tag{3.1}$$

where r_p and r_s are the complex Fresnel reflection coefficients of p and s components respectively [23].

We use J.A Woollam VASE M2000 Ellipsometer to characterize our ALD grown thin films deposited on Si substrates, the measurements are carried out at three different incident angles (55°, 60° and 65°) at wavelengths ranging from 300 nm to 1000 nm. Ellipsometer data analysis involves the following steps,

(1) **Measurement** of the sample deposited on Si (a reflecting substrate is preferable)

(2) **Modeling** of the sample: A model is constructed to represent the sample that has been measured. The polarization changes are calculated using

Fresnel equation of the model describing the sample thickness and optical properties.

(3) **Fitting** of the experimentally measured data and the model-generated data through regression analysis.

(4) **Results**: The unknown material properties are found when the experimental curves match the theoretically predicted response where the mean square error(MSE) is minimal.

In this manner, one can estimate the thicknesses of thin films ranging from few nanometers up to tens of micrometers. We use a general oscillator (GENOSC) model for ZnO, a Sellmeier model for MgO, and a material model for SnO_x. For our ternary films, we use an effective medium approximation (EMA). The EMA model assumes that when two materials are mixed together, the resulting effective medium or the mixed material retains the optical properties of its constituents. We use the Bruggemann EMA model for ZMO and ZTO.

3.2.2 Scanning Electron Microscopy

Scanning electron microscopy(SEM) focuses an electron beam over the sample scanning the surface of the material. The focused electron beam is created by using an electron gun and a combination of electron lenses and apertures to accelerate the electron beam over a column that is kept under high vacuum around 10^{-4} Pa. A control console is used to control the energy of the beam, accelerating voltages vary from few hundred volts up to 20keV. The principle of SEM involves the interaction of electron beam with the material which produces secondary electrons, backscattered electrons, characteristic x-rays, various photons of different energies collected by a detector within the SEM. The surface characteristics, composition etc. of the films can be estimated based on the interaction volume i.e how much volume within the sample the electron beam interacts and the signals generated. The electron-matter interaction is depicted in Fig. 3.4 [24]. Inelastic interaction between the incoming electron beam and the sample produces secondary electrons(SE) which originate at or near the surface(top few nanometers) of the material. Meanwhile elastic collisions between the incoming electrons and the atoms of the material result in backscattered electrons(BSE) arising from the top few hundred nanometers of the material. The energy of SE is less than BSE and it merely provides the topographical information of the material surface, on the other hand, the number of BSE reaching the detector depends on the atomic number and can provide valuable information on the morphology

of the sample. Characteristics X-rays are of great importance here as they are related to the atomic composition and are hence used for the elemental analysis of our films through energy dispersive spectroscopy.

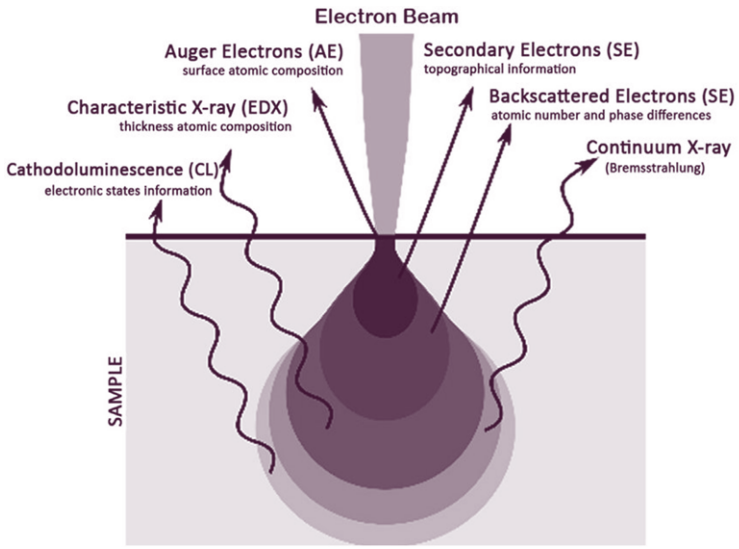

Figure 3.4: Electron-matter interaction volume and the various signals produced [24].

We utilize an Xmax $50mm^2$ EdX detector (Oxford Instruments) attached to Helios NanoLab 650 (FEI, USA) scanning electron microscope (SEM) to perform energy dispersive x-ray spectroscopy to determine the atomistic composition of the ALD grown ternary materials. We use an e-beam of 3keV at $40\mu m$ magnification for our ZMO films, the energy is sufficient enough to detect the K_α of Mg at 1.253 keV. For our ZTO films, the characterization required an e-beam energy of 6keV. All our samples are measured at an acquisition angle of 35°. Data analysis is performed using INCA software.

3.2.3 Optical characterisation

The optical properties of the deposited thin films are determined by measuring the transmission and reflection spectra using a Perkin Elmer Lambda 1050 spectrophotometer with a 150mm integrating sphere in the wavelength range 250-2500nm. The thin films deposited on glass are used for the optical characterisation and the absorption cofficient is determined from the transmittance(T) and reflectance(R) using the following relation [99],

$$T = (1 - R)e^{-\alpha t} \tag{3.2}$$

where t is the thickness of the film. We consider multiple reflections from the back and front surfaces of the films to be negligible. The bandgap of the deposited ternary films is calculated based on the relation :

$$(\alpha h\nu)^{1/r} \sim (h\nu - E_g) \tag{3.3}$$

where r=1/2 for direct transitions and 2 for indirect band transitions see inset of Fig. 3.5 for reference which includes the corresponding phonon dispersion curves. We use the direct fit for both ZTO and ZMO films. Both ZnO and MgO are direct bandgap materials while SnO_x shows both direct and indirect transitions. Although it is common for studies on ZTO thin films to report both direct and indirect bandgaps, we find that in our calculations, the direct bandgap fit works best.

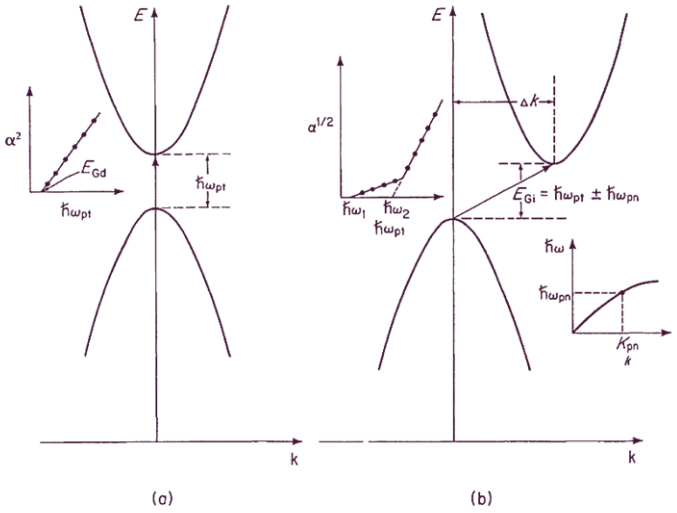

Figure 3.5: (a) Direct transition and (b) In-direct transition. The variation of absorption coefficient α with respect to the phonon energy for each transitions is shown in the inserts. [25].

3.2.4 Electrical characterization

We perform electrical characterization of our films deposited on glass using an in-line four-point-probe system with a probe spacing of 1mm and diameter of 100 μm (Jandel) and determine the sheet resistance as follows,

$$R_S = 4.532\frac{V}{I}\Omega./\square \tag{3.4}$$

through which the bulk resistivity can be determined.

3.2.5 X-ray Diffraction

X-ray diffraction(XRD) is a very powerful tool in extracting structural information of a material such as material phases, crystalline structure, crystallite size, degree of crystallinity, strain, orientation, texture etc. A characteristic X-ray diffraction pattern is obtained due to constructive interference of x-rays which are scattered by atoms in a periodic structure (lattice planes of a crystal). The working principle of XRD involves directing a beam of monochromatic x-rays towards the sample and measuring the direction and intensity of the scattered x-rays. The angle between the incident and scattered beam is called 2θ. If planes of atoms are separated by a distance d, then constructive interference occurs on satisfying Bragg's law [100],

$$n\lambda = 2d\sin\theta \tag{3.5}$$

where λ is the wavelength of the incident x-ray, θ is the scattering angle and n is an integer (n=1,2,3..). Thus interatomic distances govern the diffraction peak and the atoms themselves and their position influence the intensity of the diffraction peaks obtained. By comparing the obtained x-ray diffraction peaks occurring at specific angles against existing online databases, we identify the material and its crystalline phase.

We use grazing incidence technique where the angle between the incident beam and the sample surface is kept small in order to probe the surface of the thin film and reduce the influence of the substrate. Using Cu-Kα radiation in Bruker D8 diffractometer (Bruker, USA), the X-ray diffraction (XRD) data are collected in the 2θ range from 20 to 60° which covers the characteristics peaks of ZnO. The ICDD Pdfcards used to determine the crystalline phases for the various ALD grown materials in this study are as follows: Si(04-007-2062) ZnO (00-036-1451)[101], MgO (00-004-0829), SnO_2(00-041-1445) [102], SnO(04-005-4540) [90], Zn_2SnO_4 (00-024-1470), $ZnSnO_3$ (04-015-9628).

3.2.6 X-ray Reflectometry

X-ray reflectivity combines the techniques of x-ray diffraction and ellipsometry. XRR replaces the linearly polarized light in ellipsometry with x-rays. The x-rays reflected by the sample is compared with the reflections predicted by Fresnel equations and the deviations in reflections are used to determine the thickness and density profile of the material. XRR of our samples is performed using PANalytical X'Pert Pro diffractometer (PANalytical) with Cu-Kα radiation and fitting of the XRR data is done using GenX [103].

The densities obtained are: 3.127 g/cm^3(0.0467 AU/$\mathring{A}^3$) for MgO films, 5.33

g/cm^3 (0.0395 AU/$Å^3$) ZnO and 6.456 g/cm^3 for SnO_x. The values are in close agreement with densities reported in literature 3.07 g/cm^3 for MgO and 5.61g/cm^3 for ZnO [104].

3.2.7 X-ray Photoelectron Spectroscopy

X-ray photoelectron spectroscopy (XPS) is an ultrahigh vacuum technique used to determine the chemical and elemental states present at the surface of a material. In XPS, a beam of x-rays is irradiated on the surface of the material causing light-matter interaction between the incident x-ray photons and atoms and molecules present at the surface of the material. Electrons emitted out of the x-ray-matter interaction have characteristic kinetic energy. This characteristic energy of emitted electrons is used to identify the elements, the chemical states of the atoms and their respective binding energies. The binding energy carries the elemental and orbital information of the emitted electrons By etching the material with ion beam, through depth profiling, XPS can analyse the bulk of a material.

X-ray photoelectron spectra are acquired using a Kratos Axis Ultra-DLD photoelectron spectrometer with a monochromatic Al Kα source at an energy of 1486.6 eV and power of 150W with a 700 $\times$ 300 μm spot size. Survey spectra are acquired using a pass energy of 160 eV, whereas high resolution spectra of the Au 4f, Zn 2p, Mg 1s, C 1s and O 1s regions were collected with a pass energy of 40 eV. The binding energies are referenced to the adventitious carbon at 285.0 eV. The shape of a reference spectrum acquired on a sputter-clean gold foil was used to fit the metallic Au 4f component. All other components were reconstructed using Gaussian–Lorentzian peaks after removing a Shirley type background. For the depth profile, Ar^+ ions at an energy of 2kV are used to etch an area around 3mm x 3mm.

3.2.8 Secondary Ion Mass Spectrometry

Secondary-ion mass spectrometry (SIMS) technique involves using focused ion beam to sputter the surface of the material to be analysed. The ejected secondary ions are collected and analysed to obtain the composition at the surface of the material. A mass spectrometer is used to analyse the mass and charge ratios of the secondary ions collected hence leading to the name, secondary-ion mass spectrometry. This gives the elemental composition at the surface up to a depth of 1 to 2nm, sputtering further helps with depth profiling of the sample.

The SIMS method is used in depth profiling mode performed in CAMECA

SC-Ultra instrument using a Cs^+ beam with an impact energy of 1 keV and a beam intensity of 1.5 nA. The secondary positive ions are collected from an area 63 μm in diameter scanned from the center of 250X250 μm^2 region in MCs_x^+ mode (where M: element of interest and x =1 or 2) at low mass resolution of 400.

3.2.9 Transmission Electron Microscopy

Transmission electron microscopy (TEM)"is similar to SEM in the use of focused electron beam, however the difference lies in the fact that SEM uses back-scattered and reflected electrons while TEM uses electrons transmitted through the sample to form images giving in-depth information about the morphology and crystalline structure of the material. TEM akin to SEM uses combination of lenses and apertures to focus and generate images. In order to focus the beam transmitted out of the samples, an objective lens is used and an objective aperture is places in the back focal plane of the objective lens. The objective aperture is used to select the transmitted beam of electrons, a small objective aperture is used to select only the direct transmitted beam of electrons forming bright field images. Dark field images are formed when the objective aperture is used to select scattered electrons passing through the sample [105].

The TEM investigations are carried out using JEOL-F200 Cold FEG TEM/STEM operating at 200 kV. The samples are prepared using focused ion beam (FIB). TEM bright field - dark field imaging and energy dispersive spectroscopy (EDS) mapping in STEM mode are performed

Chapter 4

Zinc Magnesium Oxide by ALD

4.1 Introduction

Zinc Magnesium Oxide or ZMO is a solid solution of ZnO and MgO. ZnO is a II-VI compound wide bandgap semiconductor with a wurzite type structure. ZnO has a direct bandgap of 3.37eV at room temperature with an exciton binding energy of 60meV and density of 5.6 g/cm^3; MgO has an indirect bandgap of 7.8 eV with a cubic structure and density of 3.07 g/cm^3 [104]. The growth of $Zn_{1-x}Mg_xO$ by atomic layer deposition follows a supercycle approach involving the binary oxides ZnO and MgO.

The goal is to understand the interaction and influence of the individual binary ALD processes of ZnO and MgO on the growth of ternary $Zn_{1-x}Mg_xO$, examine the optimal way of mixing Mg into ZnO and correlate the growth kinetics with the material properties. Also we aim to achieve accurate control of the optical bandgap by altering the process parameters and employ ALD grown ZMO films as buffer layers for chalcopyrite solar cells.

4.2 Growth kinetics of ZnO and MgO

Self-limited growth

First, we analyse the variation of growth per cycle (GPC) as a function of precursor pulse exposure time for both ZnO and MgO to confirm that this exposure time is sufficient enough for the entirety of the substrate surface to be saturated with absorbed precursor species. Increasing the exposure time further does not increase the GPC as the substrate surface has no more

room to absorb additional precursor species, hence this change in GPC versus pulse time is also termed as the saturation curve as it helps to determine the point of saturation for an ALD process with respect to the precursor pulse time. Figure 4.1 shows the saturation curve of ZnO at 130°C, while Fig. 4.2 displays the saturation curve for MgO at 130°C and 150°C. The saturation curve helps to choose appropriate pulse time to achieve the self-limited saturated characteristic of an ALD process; for a ZnO ALD process 200 ms is used as the pulse time and for an MgO ALD process it is set as 4 s to attain saturation during growth. The vast differences in pulse time required for saturation for ZnO and MgO ALD process is due to the different vapour pressures of the precursors used, as diethyl zinc has a vapour pressure of 121 hPa it only required 200ms to saturate the substrate surface. As the vapour pressure of $MgCp_2$ is lower at 0.042 hPa, a longer exposure time is required to saturate the surface.

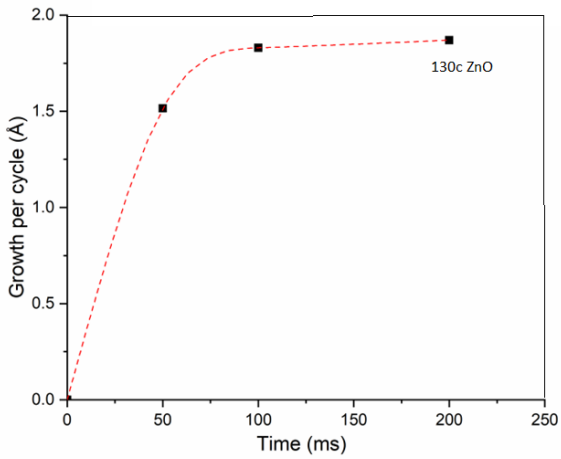

Figure 4.1: Saturation curve of ZnO ALD process at 130°C

ALD Temperature window

The other important parameter involved to attain saturation is the deposition temperature. Fig. 4.3 shows the variation of growth of ZnO with respect to the deposition temperature. Within the ALD temperature window, the growth of ZnO at first increases with increase in temperature from 1.95 Å/cycle at 130°C to the highest GPC of 2.05 Å/cycle at 150°C and falls with further increase in temperatures. At very high temperatures, the number of OH groups available likely decreases resulting in lower growth rates

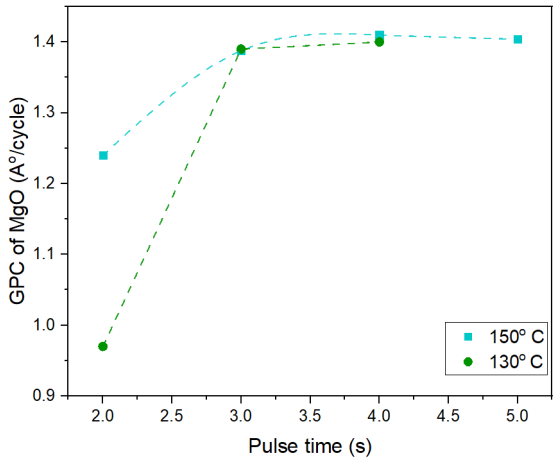

Figure 4.2: Saturation curve of MgO ALD process at 130°C and 150°C

[106]. On the other hand, the GPC of MgO remains constant with increase in temperature from 130°C to 150°C at 1.4 Å/cycle.

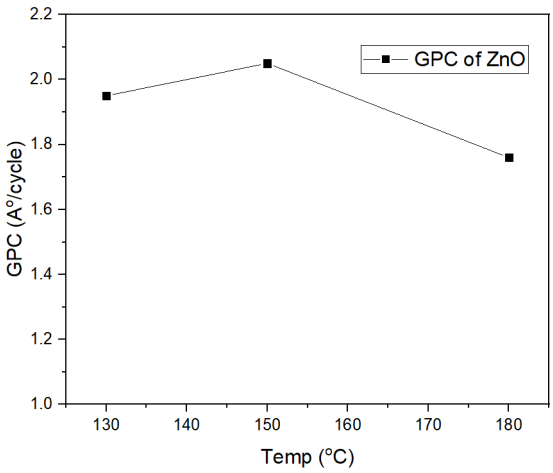

Figure 4.3: ZnO growth vs deposition temperature

Linearity

Another essential characteristics of an ALD process is the linearity which can be verified by plotting thicknesses as a function of number of ALD cycles or loops. $Zn_{1-x}Mg_xO$ (ZMO) films are grown at 130°C and 150°C using the supercycle approach based on the insofar optimized ZnO and MgO ALD processes with varying pusle ratios (PR) and bilayer period (BP). Fig. 4.4

shows the linearity of ZnO, MgO and $Zn_{1-x}Mg_xO$ (PR = 0.25). All the films deposited show a linear relationship between the number of ALD cycles and the thicknesses.

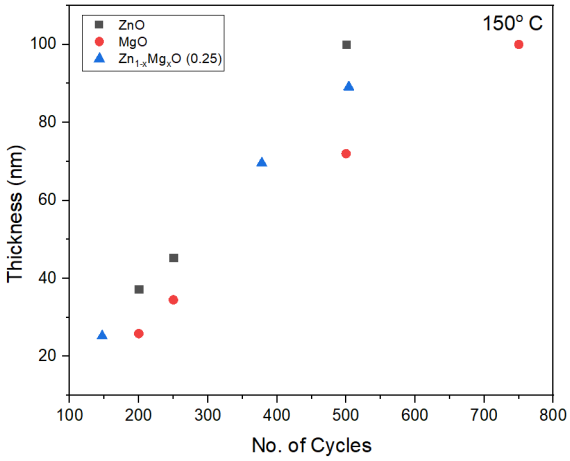

Figure 4.4: Thickness vs number of cycles of ZnO, MgO and ZMO (PR=0.25) films 150°C

4.3 Growth kinetics of ZMO

4.3.1 Effect of deposition temperature

At deposition temperatures 130°C and 150°C Fig. 4.5 shows that the GPC decreases with increase in pulse ratio. ZnO has a higher GPC than MgO, therefore the growth of ZMO is expected to fall with increase in pulse ratio and we observe the same in Fig. 4.5, the GPC of ZMO tends towards that of MgO with increase in pulse ratio i.e Mg pulses. Still, the growth of ZMO with varying pulse ratio is found to deviate from the expected linear combination of GPC valzes from ZnO and MgO calculated from (2.13).

The composition of our $Zn_{1-x}Mg_xO$ films is varied only up to x= 0.4 beyond which previous studies report a likely phase separation [36] [28]. Fig. 4.6 shows the variation of Mg composition with varying pulse ratios at deposition temperatures 130°C and 150°C. We find deviations from the expected values for the GPC as well as the composition. With decrease in temperature, an increase in Mg composition is predicted by (2.14), as a decrease in temperature causes ZnO GPC to decrease. The expected behaviour is observed so in Fig. 4.6 where Mg composition at 130°C is higher than at

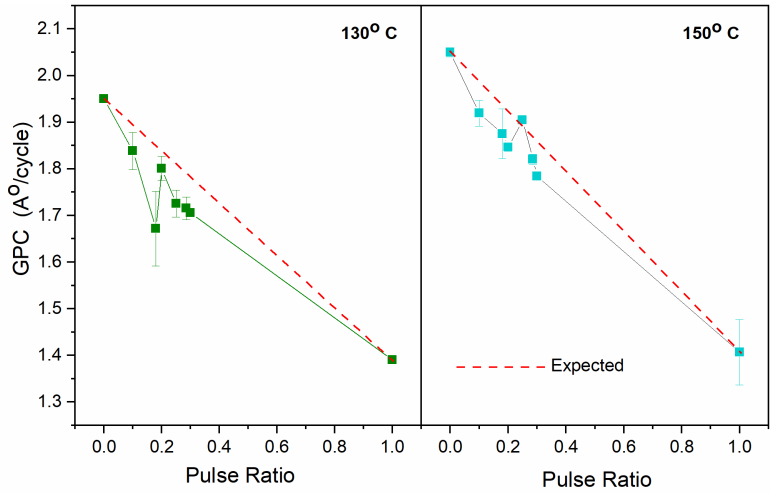

Figure 4.5: GPC of $Zn_{1-x}Mg_xO$ films deposited at various pulse ratios (BP=10) at temperatures, 130°C (a) and at 150°C (b). The expected GPC is shown by dashed line.

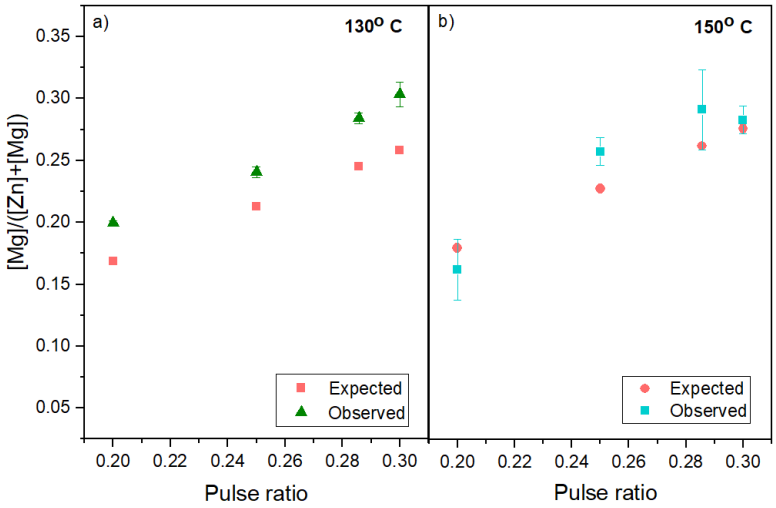

Figure 4.6: Mg composition in $Zn_{1-x}Mg_xO$ films for various pulse ratios (BP=10), deposited at (a) 130°C and (b) 150°C (b). The expected Mg composition is shown in red and is computed from (2.14)

150°C. Furthermore, a remarkably higher Mg content is observed within all the deposited ZMO films, higher than the expected Mg content. The high Mg content could be possible due to enhanced growth of MgO or retarded growth of ZnO during ZMO synthesis. To understand the interplay between ZnO and MgO processes and the possible reasons behind the increased Mg

incorporation, the influence of the bilayer period on the growth kinetics is examined.

4.3.2 Effect of bilayer period

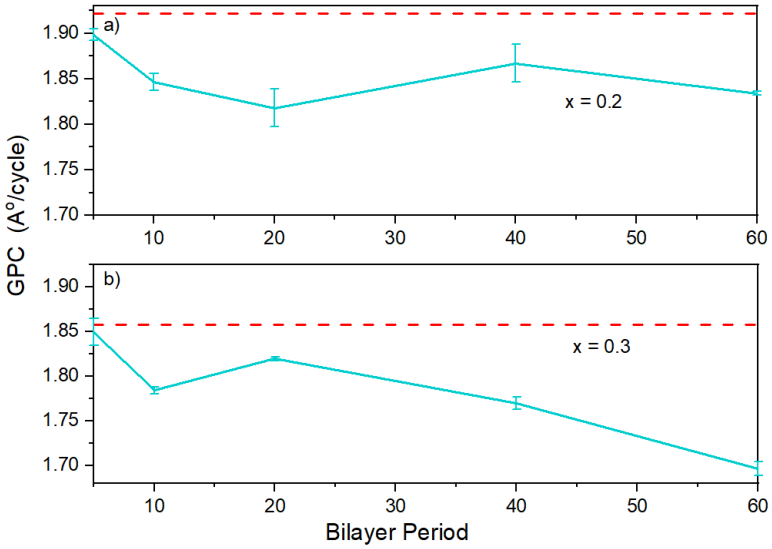

Figure 4.7: GPC of $Zn_{1-x}Mg_xO$ versus bilayer period for two different pulse ratios, (a) 0.2 and (b) 0.3 deposited at at 150°C. Expected GPC is indicated by red dashed lines.

As seen previously, the GPC of ZMO films with varying bilayer period at a given pulse ratio is found to be less than the expected GPC. We see the expected GPC in red in Fig. 4.7 and the GPC of ZMO films as a function of varying bilayer period are shown for two different pulse ratios 0.2 and 0.3. Furthermore, the GPC decreases with increase in bilayer period. The GPC is higher at the smallest bilayer period and falls with increase in bilayer period. This variation in GPC with bilayer period follows a trend similar to the substrate-enhanced growth described earlier depicted in Fig. 2.17. As bilayer period increases, the number of cycles per sublayer increases, i.e the number of ZnO and MgO cycles in succession within a supercycle increase, see Fig. 3.1. To understand whether this non-linear growth behaviour of ZMO films arises due to a substrate-enhanced growth behaviour of ZnO or MgO, the compositional variation of the ZMO films with respect to bilayer period is examined.

The variation of composition as a function of bilayer period is depicted in Fig. 4.8 for films deposited at temperatures 130 °C (a) and 150 °C (b) for

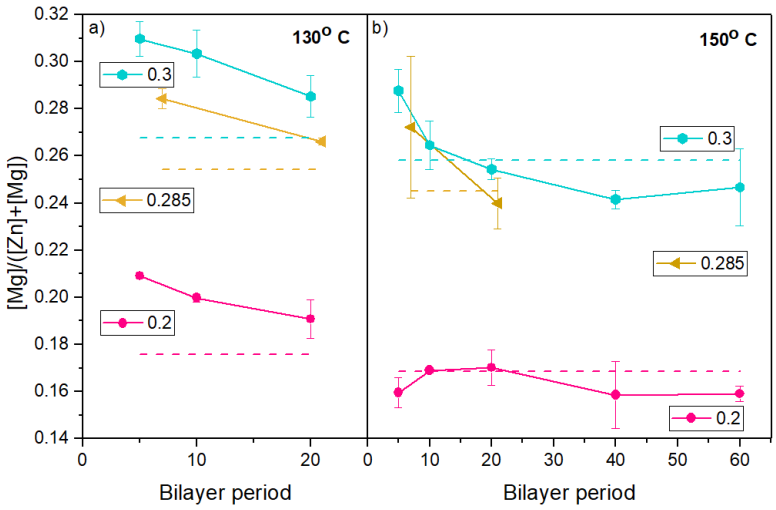

Figure 4.8: Composition of $Zn_{1-x}Mg_xO$ versus the bilayer period for films deposited at different temperatures, (a) 130 °C and (b) 150 °C , and for various pulse ratios indicated in the legends.

three different pulse ratios (PR=0.2, 0.285 and 0.3). In all the cases, we clearly observe a decrease in Mg content with increase in bilayer period. If it is substrate-enhanced growth of ZnO, it should result in a decreased Zn content with almost constant Mg content. But it is the Mg content which is observed to decrease with increase in bilayer period, and in fact it is the highest (in comparison with the expected composition) at the smallest bilayer period, indicating an enhanced growth of MgO. As the smallest bilayer period mixture involves MgO growing on ZnO surface more frequently rather than MgO on MgO, it can be said that MgO growth on ZnO surface follows a substrate-enhanced growth. Indeed one cycle of MgO is enough to incorporate Mg into the ZMO system and the growth of MgO is not disrupted by the preceding ot succeeding ZnO cycles. Only when MgO grows on MgO, the growth and composition decreases with successive MgO cycles on increase of bilayer period. Therefore in the synthesis of ZMO by ALD, ZnO layer enhances the growth of MgO.

This growth behavior of ZMO can be further explained by looking into the individual ALD growth kinetics of the binary oxides. In situ spectroscopic ellipsometry studies on atomic layer deposited MgO films on Si has shown that the growth of MgO is strongly dependent on the density of surface hydroxyl groups and the initial growth of MgO is nonlinear [107]. Furthermore, surface hydroxylation studies on MgO(100) indicate that surface hydroxylation enhanced by dissociative water adsorption only occurs at defect sites

[108]. Thus an MgO layer with less number of hydroxyl groups at its surface promotes neither the growth of subsequent MgO layer nor the growth of the next ZnO layer as it lacks reaction sites for the precursors half-reaction. On the other hand, the surface of ZnO layer is saturated with OH monolayer [109], with a better hydroxyl density it offers more reaction sites than an MgO layer. *The microstructure of the material could also influence the hydroxyl density, as the roughness of ZnO is higher compared to MgO* [27] [26].

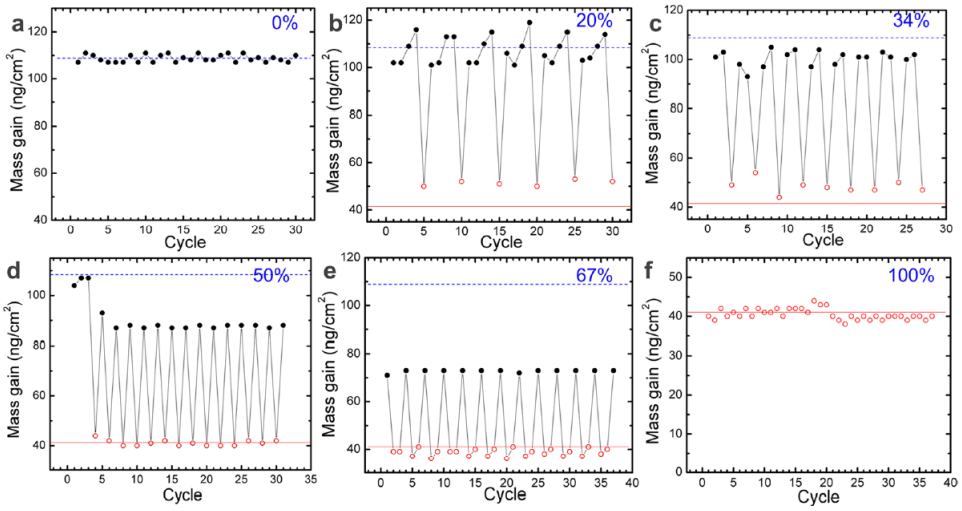

Figure 4.9: Growth rate resulted from in-situ QCM measurements at 120°C during ALD of $Zn_{1-x}Mg_xO$ films, including (a) ZnO, (b) $Zn_{1-x}Mg_xO$ (x=0.2), (c) $Zn_{1-x}Mg_xO$ (x=0.34), (d) $Zn_{1-x}Mg_xO$ (x=0.5), (e) $Zn_{1-x}Mg_xO$ (x=0.67), and (f) MgO. The horizontal dashed line and solid line are the average growth rates of steady-state ZnO and MgO ALD processes respectively [26].

In addition, we note that similar behaviour have been observed in QCM studies on atomic layer deposited ZMO supporting our conjecture that ZnO layer promotes the growth of MgO in ZMO synthesis. From Fig. 4.9 it can be seen that in the growth of ZMO at 120°C, the mass gain of MgO cycles (figures b and c) is higher than that of pure MgO (solid red line) [26]. On a much closer look, it can be found from Fig. 4.9 that a mass gain of an MgO cycle surpasses its steady-state value only when an MgO cycle follows two or more ZnO cycles (figures b and c). At 50% composition (d), the mass gain of MgO is similar to that of its steady-state value and even decreases further with consecutive MgO cycles at 67% composition (e). This corroborates our conclusion that an MgO layer neither promotes ZnO growth nor MgO

growth, evident from Fig. 4.9 (d and e) respectively, where mass gain of ZnO falls below its steady-state value. In fact, on comparison (figures b, c and d) it can be seen that one requires ZnO cycles in succession to counteract the effects of MgO cycle on the overall growth. Fig. 4.9 (b) where the mass gain of individual materials are higher than their respective steady-state mass gain, indicates on optimal mixing of 4:1 ZnO:MgO cycles to achieve effective growth rates. Therefore, for an effective mixing of MgO and ZnO in ZMO films, the bilayer period should be minimal. Moreover, comparing our results in Fig. 4.8 with the QCM studies, it can be further concluded that mixing one MgO cycle with three to four consecutive cycles of ZnO results in the most efficient incorporation of MgO.

In ALD based ternary material synthesis, mixing small number of ZnO cycles with MgO results in effective Mg incorporation into ZMO films, in contrast to zinc tin oxide where mixing small number of ZnO cycles into SnO_x results in deposition of less Sn [85] into the ZTO films. *Therefore by optimizing the bilayer period, good growth and high Mg content in ALD grown* $Zn_{1-x}Mg_xO$ *films can be achieved. We have also demonstrated that investigating the effect of bilayer period can be an easy, potential alternative tool to QCM studies in understanding the mixing and interplay of binary materials in the synthesis of ternaries by ALD* [27].

4.4 Structure-Property relationships

4.4.1 Structural properties

The structural properties of the ALD deposited ZMO films can be inferred from Fig. 4.10 which shows the x-ray diffractograms of ZnO, MgO and $Zn_{1-x}Mg_xO$ films deposited at 150°C. The XRD diffractograms of ZMO films of various bilayer periods (PR=0.2) are also portrayed. ALD deposited ZnO and MgO films are x-ray amorphous at 130°C. MgO remains x-ray amorphous even at higher deposition temperatures. The x-ray diffractorgrams of ZnO deposited at 150°C shows a wurzite structure. The ZMO films deposited at 150°C show a single phase structure similar to that of wurzite ZnO. We do not observe phase separation even with increase in Mg content. However, with increase in Mg content, the ZMO films exhibit amorphous structure beyond a pulse ratio of 0.25. Nevertheless, in this case of ZMO films at a pulse ratio of 0.2 shown in Fig. 4.10, the addition of Mg causes peak shift of 2θ to lower angles, in particular it causes (100) and (110) reflection peaks to shift to lower angles by 1.66°. Meanwhile, a change in bilayer period does not cause any peak shift but causes a change in relative peak intensity. At the smallest

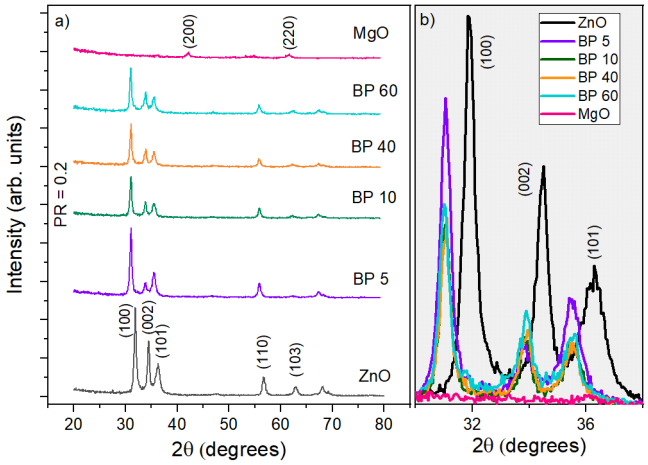

Figure 4.10: XRD diffractograms of ZnO, MgO and ZMO (PR = 0.2) deposited at 150°C with various bilayer periods (a), and zoom around the peaks corresponding to (100), (002) and (101) ZnO crystal planes (b), showing the peak shifts observed in ZMO films compared to pure ZnO [27].

bilayer period the intensity of (101)-reflection is higher than (002)-reflection but switches for larger bilayer period and is more akin to ZnO peak-reflection intensities. This behaviour can be attributed to the columnar growth of ZnO which is inhibited by small bilayer periods while promoted at larger bilayer periods. The lattice mismatch between ZnO and MgO causes tensile stress which we observe in our deposited ZMO films as positive strain. A positive strain of 1.32% is observed due to the increase in in-plane lattice constant $\boldsymbol{a}$ from 3.243 Å of pure ZnO to 3.286 ÅẆe found that annealing of films in air at 400°C for 15 minutes does not improve the crystallinity of the films.

4.4.2 Optical properties

Understanding the optical characteristics of the ZMO films is of utmost importance to achieve high-level of bandgap engineering and tailor the ZMO films to serve as effective buffer layers for solar cells and for different applications. The optical transmittance of ZMO films deposited on glass in the UV-Vis range is shown in Fig. 4.11(a) with the legend indicating the various pulse ratios. A blue shift in absorption edge is observed with the addition of Mg. The bandgap is determined from the Tauc plot, assuming a direct bandgap fit, for ZMO films of higher Mg composition (PR $>$ 0.3) the bandgap is limited by absorption from glass substrate.

The variation of the band-gap as a function of the observed Mg composition

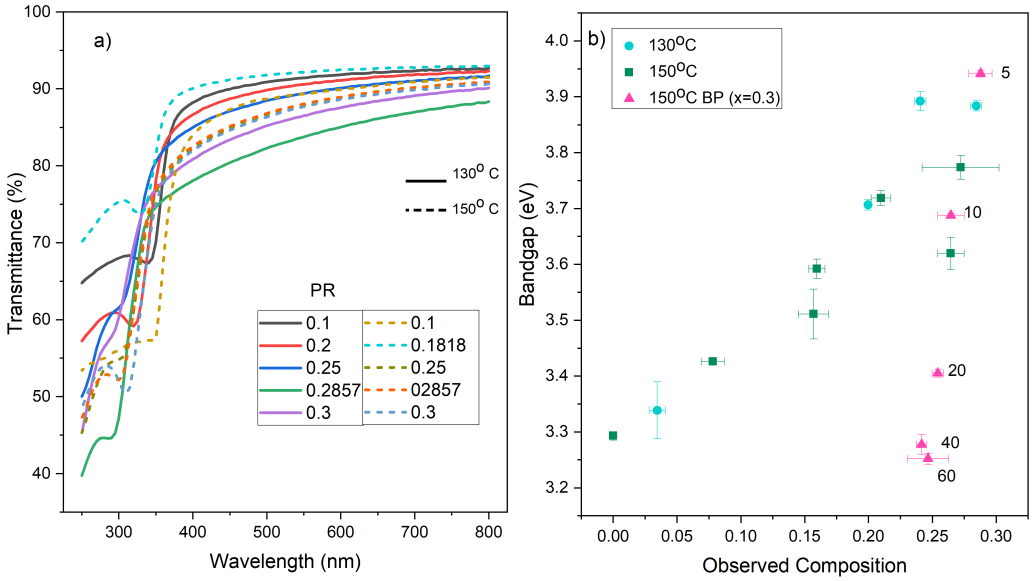

Figure 4.11: (a) Transmittance spectra of $Zn_{1-x}Mg_xO$ deposited at 130 °C (straight lines) and 150 °C (dashed lines) for different pulse ratios denoted by the legend. (b) Band-gap versus observed Mg composition of ZMO films(BP≃10) grown at 130 °C (green squares) and 150 °C (blue circles). The band-gap of films at different bilayer periods for ZMO (PR = 0.3) grown at 150°C is represented by the pink triangles, with their BP indicated inside the graph.

in our ZMO films grown at various temperatures can be seen in Fig. 4.11(b) as green squares and blue dots respectively. The band-gap of deposited ZMO films increases with increasing Mg content as the absorption edge shifts towards lower wavelengths. Fig. 4.11(b) shows that the bandgap is independent of the deposition temperature and is exclusively dependent on the composition of the Mg films. Thus, fine tuning of the band-gap by changing the Mg composition is possible through altering pulse ratios of the ALD processes during synthesis. The variation of bandgap of our ALD grown films with the addition of Mg is in agreement with previously reported trends in bandgap in other studies [26] [28].

The influence of the bilayer period over the optical properties of ZMO films can be seen in Fig. 4.11(b), with red triangles representing the band-gap of ZMO (PR = 0.3) at different bilayer periods grown at 150°C. Even though the Mg composition remains nearly constant, with increasing bilayer period, the bandgap of ZMO (PR = 0.3) films decrease to values of ZnO (3.29 eV). At larger bilayer periods around 40 and 60, the band-gap is almost equivalent

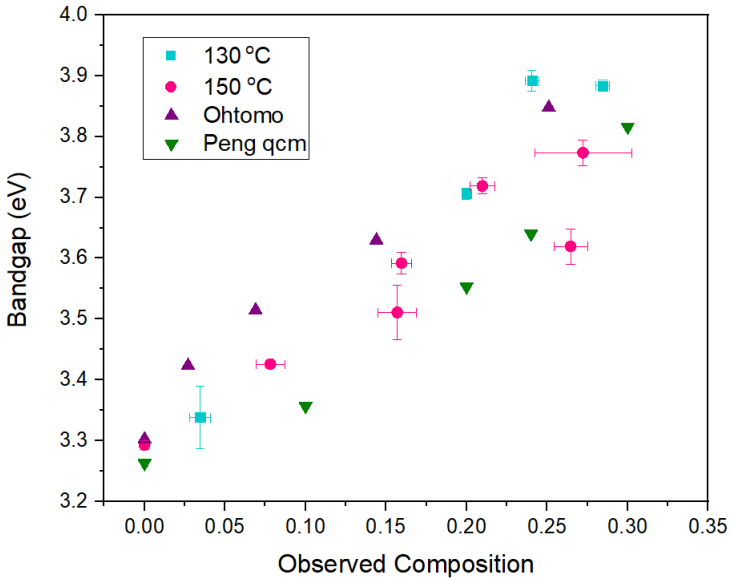

Figure 4.12: Variation of bandgap as a function of observed composition of our ZMO films at 130°C(blue) and 150°C(pink) in comparison with the bandgaps from [26] [28].

to ZnO, indicating that the optical properties of ZMO films is dominated by the ZnO.

Plotting the variation of bandgap as a function of bilayer period, Fig. 4.13 helps further understand the strong effect that bilayer period has over the optical properties. For a given pulse ratio, ZMO films show the highest bandgaps at the smallest bilayer periods where one MgO layer is mixed with few ZnO cycles. However, the bandgap starts decreasing with increase in the bilayer period where fine mixture of ZnO and MgO cycles is no longer present. This indicates a weak inter-diffusion of MgO into ZnO at bilayer periods ranging from 10 to 20.

In terms of length scale, ZnO with an electron effective mass of $0.27m_0$ and a dielectric constant $\epsilon = 8.5$ (as reported for ZnO single crystals in [110]) has an excitonic Bohr radius a_B of 1.87 nm computed from (2.6) [111]. Within a supercycle, the thickness of ZnO layer varies with bilayer period, for e.g. going from a bilayer period of 10 to 20, ZnO thickness varies from 1.6 nm to 3.2 nm for a PR of 0.2. Electrons in the ZMO thin films experience a mixed material, when the thickness of the ZnO layer is below the Bohr radius (i.e. <1.8 nm) which is the case for small bilayer periods. As the bilayer period increases, ZnO layer thickness increases and the electrons encounter more

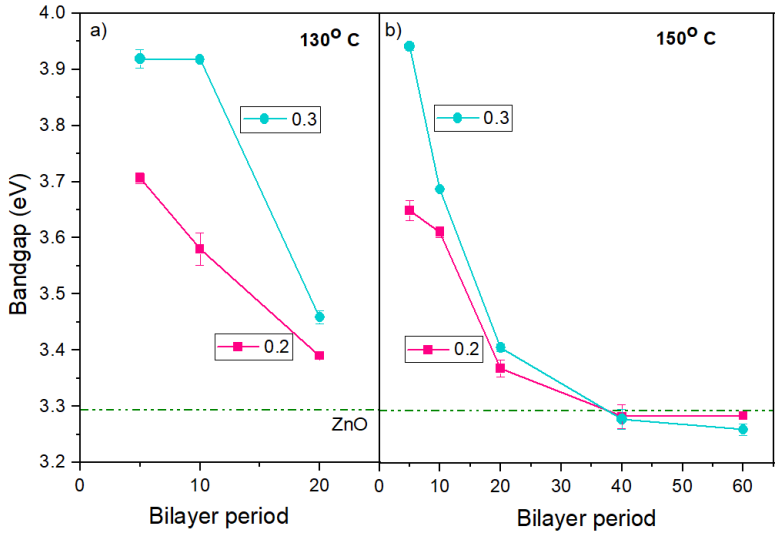

Figure 4.13: Band-gap of $Zn_{1-x}Mg_xO$ as a function of the bilayer period for two deposition temperatures, 130 °C (left) and 150 °C (right), and for two different pulse ratios 0.2 and 0.3, as indicated in the legends. The horizontal dotted-dashed line is the measured band-gap for pure ZnO deposited by ALD.

of one material rather than a finely mixed material. When the ZnO layer thickness becomes greater than the bohr radius, *the influence of ZnO on the carriers dominates* [27].

Therefore, when the bilayer period is small, we obtain well-mixed ZMO thin films, when the bilayer period increases, we see more of a multilayer behaviour of ZMO films with the optical properties dominated by ZnO. A transition from mixed to multilayer material occurs and this is observed for bilayer period greater than 10. This indicates for Mg to diffuse well into the ZnO host and form well-mixed ZMO films, the bilayer period should be less than 10. At these pulse ratios, typically 7 to 8 ZnO monolayers are present which can be regarded as the limit of penetration of Mg into ZnO. Additionally, as the bandgap continues to vary up until a bilayer period of 20, this can be used to tune the optical properties making bilayer period another important supercycle parameter next to pulse ratio.

4.4.3 Electrical properties

In analysing the structural properties, we found that the ZMO films deposited at 130°C and ZMO films of higher Mg content (PR 0.25 and above) showed amorphous structure, a similar trend is observed with electrical properties

wherein they exhibit high resistivity. Only ZMO films deposited at 150°C showed finite conductivity and especially those with higher bilayer period exhibited better conductivity (BP of 10 and above). We observe conductivities of 1.445 S/cm and 0.266 S/cm for ZMO films of pulse ratio 0.1 (9 ZnO + 1 MgO) and 0.2 (8 ZnO + 2 MgO) respectively; the conductivity of films with PR of 0.2857 and 0.3 is non-measurable [27]. It can be inferred that conductivity of ZMO films is dependent on composition, conductivity decreases with increase in Mg content. As MgO films deposited at 150°C are highly resistive, increase in the number of MgO cycles with increasing pulse ratio makes the films more resistive. Therefore, any conductivity observed in ZMO films should be due to ZnO. The role of ZnO layer over the electrical properties of the ZMO films can be further understood from the effect of bilayer period on the conductivity.

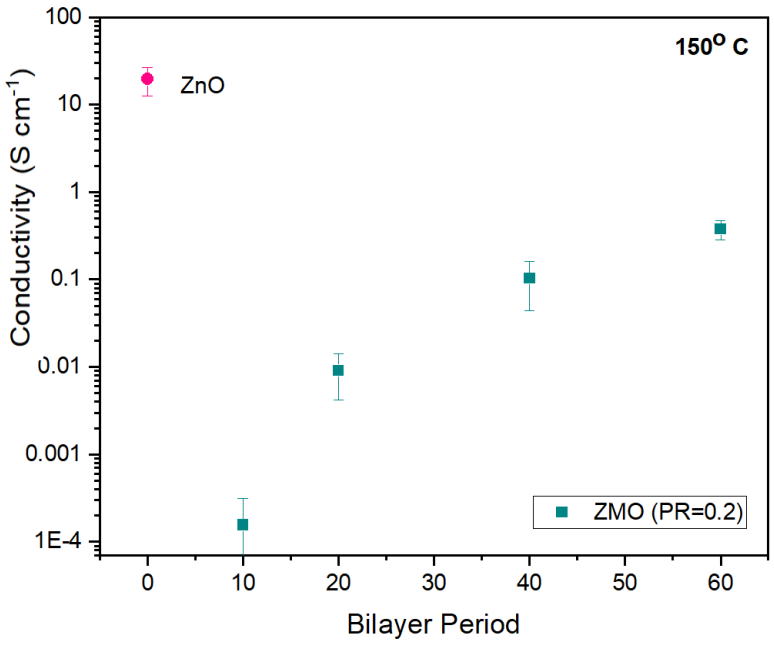

Figure 4.14: Variation in conductivity of ZMO films grown at various bilayer periods at a pulse ratio of 0.2. Conductivity of ZnO film in pink is shown for comparison. All the films grown at 150°C.

As conductivity is poor at higher pulse ratios, we demonstrate the change in conductivity with respect to change in bilayer period for ZMO films with low Mg content (PR=0.2) at 150°C in Fig. 4.14. The conductivity of the ZMO films is nil at at lower bilayer periods (BP$\leq$10) and increases with increase in bilayer period. Starting from bilayer period of 10 and up until 20 the ZMO

films exhibit low conductivity, beyond the bilayer period of 20 (BP≥20), the conductivity improves. As the number of successive ZnO cycles within a supercycle increases with increase in bilayer period, the improvement in conductivity can be ascribed to thicker ZnO layers reaffirming the important role of ZnO over the electrical conductivity of ZMO films. While at lower bilayer periods, the ZMO films behave as well-mixed materials, at larger bilayer periods (BP≥40), a multilayer like behaviour is observed with ZnO dominating over the electrical properties of the ZMO films. However, unlike the optical characteristics, the electrical properties do not show clear transition between these mixed to multilayer behaviour with increase in bilayer period.

4.5 ZMO as Buffer layers for Chalcopyrite Solar Cells

We deposit $Zn_{1-x}Mg_xO$ buffer layers by ALD for selenium-free $Cu(In, Ga)S_2$ solar cells as an alternative to the traditional CdS buffer layer. To reduce interface recombination and provide a suitable band alignment with the $Cu(In, Ga)S_2$ absorber of bandgap ∼1.6eV we deposit $Zn_{1-x}Mg_xO$ films of pulse ratios between 0.25 and 0.4. Relevant pulse ratio and the bilayer period are chosen based on the growth kinetics and optical properties observed. In particular ALD grown $Zn_{1-x}Mg_xO$ films with x= 0.27, 0.30 and 0.37 with a measured bandgap of 3.8, 3.9 and 4.6 eV respectively are used. All the ZMO films involved at least two successive MgO cycles such that the bilayer periods are close to 10, for 0.27 (5 ZnO+ 1 MgO), for 0.3 (7 ZnO +3 MgO) and 0.37 (3 ZnO + 2 MgO). Buffer layer x=0.27 and 0.37 were deposited at 150 °C and x=0.3 at 130 °C. Post buffer deposition, we determined the compositions of deposited ZMO buffers to be 0.266 for x=0.27, 0.291 for x=0.3 and 0.40 for x=0.37. Increase in composition increases the bandgap as discussed in section 4.4.2 which implies a shift in conduction band minimum(CBM) to higher energies. As mentioned in the background, a higher CBM than the absorber creates a positive conduction band offset (CBO) which increases the efficiency, however a large positive CBO results in an electrical barrier leading to QFL losses. The same is observed in Fig. 4.15 [29] where efficiency, fill-factor and interface V_{OC} are plotted with respect to the Mg content of the ALD deposited ZMO buffer films. For an in-depth understanding, refer [29].

The best $Cu(In, Ga)S_2$ device with the optimized ALD ZMO buffer composition at x=0.27 and a sputter deposited Al:(Zn,Mg)O i-layer combination, showed 14% efficiency, with an open-circuit voltage of 943 mV [29].

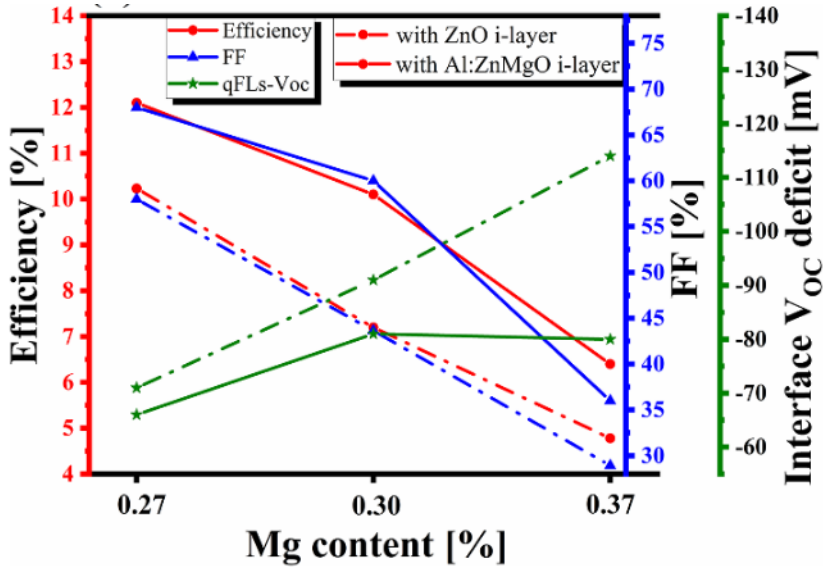

Figure 4.15: Variation of PCE (left axis), FF (right axis), and interface V_{OC} (second right axis) with varying Mg content in ZMO buffer layers [29].

4.6 Conclusion

We thus developed a reliable and reproducible thermal ZMO ALD process, investigated the interface kinetics of ZnO and MgO ALD process in ALD grown ZMO showing MgO growth is enhanced by ZnO surface and demonstrated that with bilayer period, one can probe the growth kinetics making it a great alternative to QCM studies. Through our studies, we show the effective way to incorporate Mg into the ZnO host, and by analysing the changes in material properties of ZMO films with addition of Mg, we discover a strong dependence of the optical properties on the bilayer period. We explore possible mechanisms for such dependence and identify that the mixed nature of the ZMO films changes with bilayer period, leading to confinement effects at smaller bilayer periods and ZnO dominance at larger bilayer periods over the material properties. We establish a consistent process-structure-property relationship and reveal not only the pulse ratio but also the bilayer period can be used as an effective supercycle parameter to control the material properties and validate the same by applying ALD-deposited ZMO films as buffer layers for chalcopyrite solar cells.

Chapter 5

Structural transitions in Zinc Magnesium Oxide by ALD

5.1 Introduction

Nanolaminates are multilayers consisting of nanometer thick films. In the growth of ternary films by ALD, with the supercycle approach we can obtain a range of different phases from doped material, well-mixed material and multilayers. With a large bilayer period, we obtain a multilayer material as shown in Fig. 5.1 (right) and for a small bilayer period a well-mixed material is deposited (Fig. 5.1 (left)). The bilayer period as a process control parameter takes a crucial role over the mixing of the material. Therefore, understanding the structural variations becomes necessary to achieve desired mixture of the material: a well-mixed material or a multilayered material. Moreover, the transition from a multilayered material into a well-mixed material becomes significant to engineer films depending on the type of application.

5.2 Nanolaminated growth regime

It becomes quite evident that a large bilayer period produces ternary multilayer films. In the synthesis of ZMO, as bilayer period 60 and above employ more than 20 successive ZnO cycles, each ZnO layer with thickness of 5nm and above forms a layered structure sandwiched between MgO layers. In ZMO film of BP 60, the supercycles of period 60 are repeated for 7 cycles to deposit film of thickness close to 100 nm. Fig. 5.2 shows XRR diffractogram of ZMO film of large bilayer period (BP=60) deposited at 150° (PR=0.3).

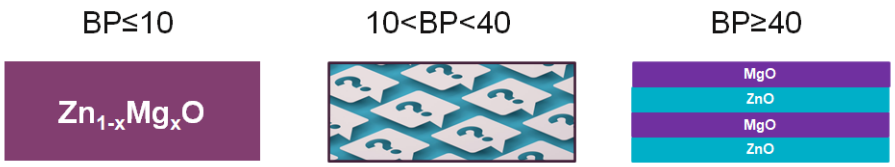

Figure 5.1: Structural transition of $Zn_{1-x}Mg_xO$ from mixed material to layered material. In the left, the well-mixed phase of $Zn_{1-x}Mg_xO$ is obtained for bilayer period (BP≤10) and the far-right depicts a multilayered material for larger bilayer period. This chapter deals with the understanding of the transition between the regime denoted by the material in the middle.

A peak in XRR gives a plane separation, the first peak corresponds to the interface between the substrate and the film also known as the density edge. The thickness can be determined from the periodicity of the oscillations, the smaller oscillations occurring frequently (at angles 0.6 to 1 and from 1.2 to 1.7 and so on) denote the thick ZnO layer. The large peaks (at 1.1, 1.8 and 2.7) represent the interface between ZnO and MgO denotes the MgO layer. From the XRR spectra we clearly see a multilayered structure with peaks and oscillations corresponding to each layers.

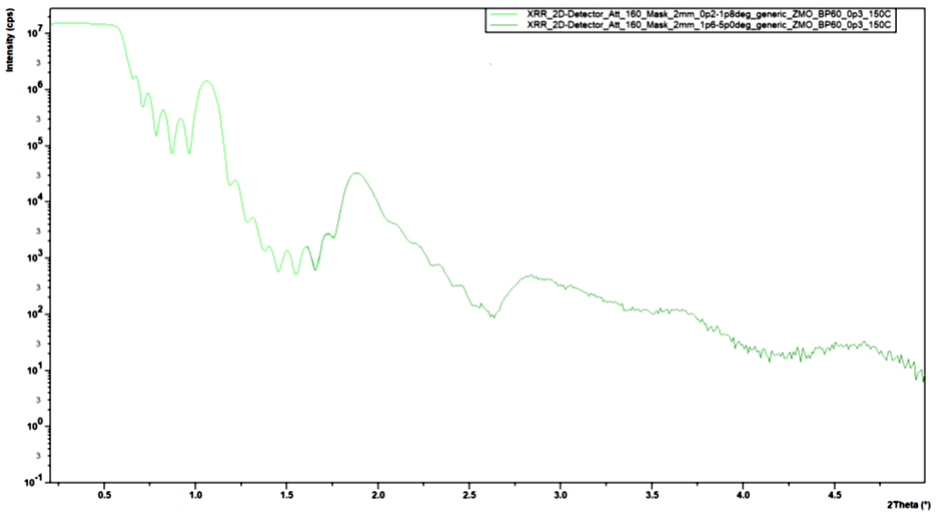

Figure 5.2: XRR Spectra of Multilayered ZMO, ZMO with 7 multilayers, the peaks after the density peak correspond to a multilayer

This multilayer stack is further confirmed by XPS depth profiles. Fig. 5.3

shows the XPS depth profile of ZMO film (BP=60). Zn, Mg, O elemental spectra are represented in blue, black and red respectively. The peaks of the spectra alternate with respect to sputtering time which corresponds to the depth of the film. From the XPS spectra, we see seven distinct peaks corresponding to 7 multilayers starting from the MgO layer on top, followed by ZnO and MgO peaking again and so on. The blue line representing the ZnO layer, peaks high as MgO peaks fall indicating a clear alternating structure. The fluctuating oxygen profile might indicate the varied amount of oxygen present in ZnO layer versus an MgO layer. As we do not observe O-rich ZnO or O-poor MgO in the XPS of the individual binary materials, we attribute it to ion-beam induced artifacts. We find the intensity of the peaks to attenuate with sputtering times in the depth profile i.e from the surface of the film towards the substrate. It becomes relevant to understand whether the attenuation of the elemental peaks in the multilayer arises out of sputtering-induced roughness or from the multilayered films themselves. Ion-beam induced artifacts such as atomic mixing, structural disorder, increased roughness etc. are more common with the use of Ar^+ [112]. Therefore, to analyse the multilayer structure further and resolve the influence of these artifacts, we perform a SIMS analysis.

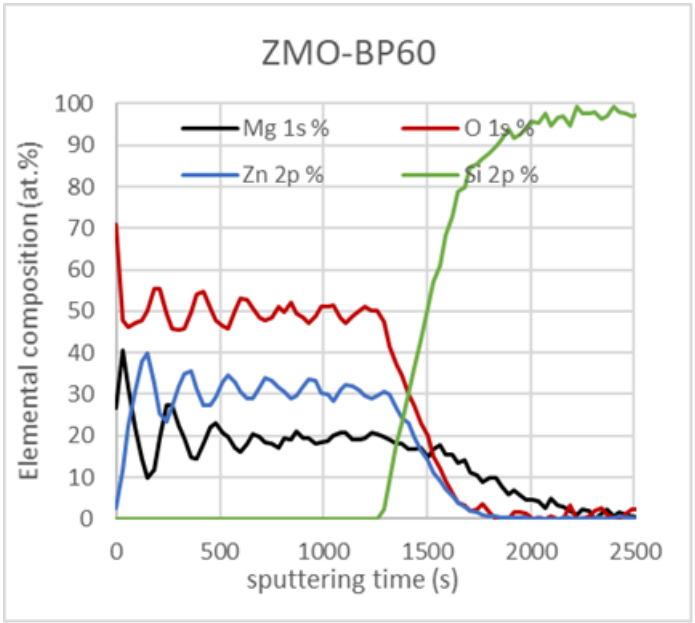

Figure 5.3: XPS depth profile starting from the surface of the thin film moving towards the substrate with depth. Hence increased Si peak with depth once substrate is reached. Zn, Mg, O elemental spectra are represented in blue, black and red respectively

SIMS characterisation employs Cs^+ ions at 1kV as opposed to the 2kV Ar^+ ions in XPS. It has been reported that depth profiling with 1kV Cs^+ ion offers better resolution due to lower sputtering-induced roughness and lower atomic-mixing length in the study of polycrystalline Ni/Cu multilayered thin films [113]. Fig. 5.4 shows SIMS depth profile, herein the elemental spectra Zn, Mg and O are represented in red, green and blue correspondingly. Moreover, we do not observe strong attenuation of the oscillations with respect to the depth profiles similar to Fig. 5.3, we still see a slight variation in the intensities of the peak. Initially the peak intensities are high, they get smaller with depth however they become more pronounced again with increasing depth. The variation in elemental peaks in XPS and SIMS profile show opposite trends, in the former the oscillations in the XPS spectra are ascribed to the sputtering-induced roughness and mixing which is negligible in SIMS. Therefore, oscillations in SIMS spectra depict the morphology of the deposited films pointing towards a defined ZnO/MgO interface close to the substrate of the film and a more mixed interface closer to the surface. To confirm the SIMS findings and to thoroughly investigate the roughness and interface effects between the layers, we perform STEM-EDS mapping.

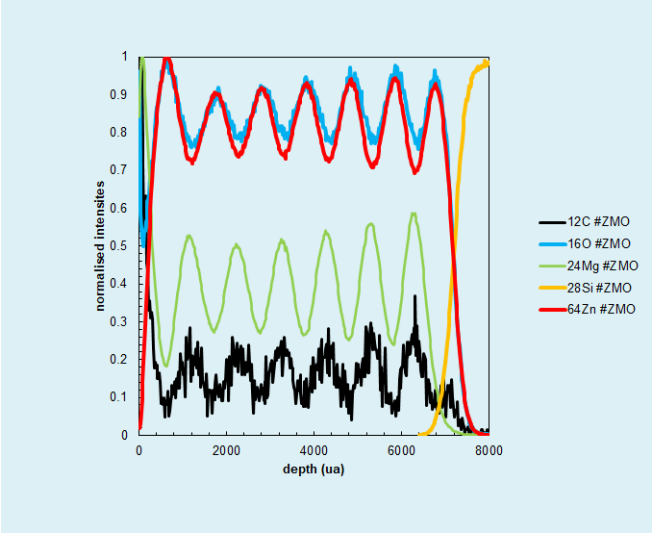

Figure 5.4: SIMS depth profile with normalized intensities moving from the top of the ZMO surface towards the substrate with depth.

The STEM-EDS profile is provided in Fig. 5.5, Zn, Mg and O peaks are indicated by blue, green and red respectively and the substrate is at distance 0 and the surface of the film is at 90 nm. With a high resolution TEM, oxygen is detected across both ZnO and MgO layers similarly and a constant oxy-

gen profile can be seen across the multilayered structure. This emphasizes that the oscillations of the O content in XPS and SIMS is due to variable etching rates and artifacts rather than real variation in O content. We see a high Zn peak alternates with distance and against the red Mg peaks. As the film is deposited on Si starting with ZnO, a high Zn peak is observed at the beginning of the growth which alternates with Mg as an MgO cycle is deposited after. The 7 peaks correspond to the 7 alternating supercycles which end with MgO cycle at the top, corresponding Mg peak at 90 nm. Similar to SIMS, we find that the elemental peaks have high intensity at

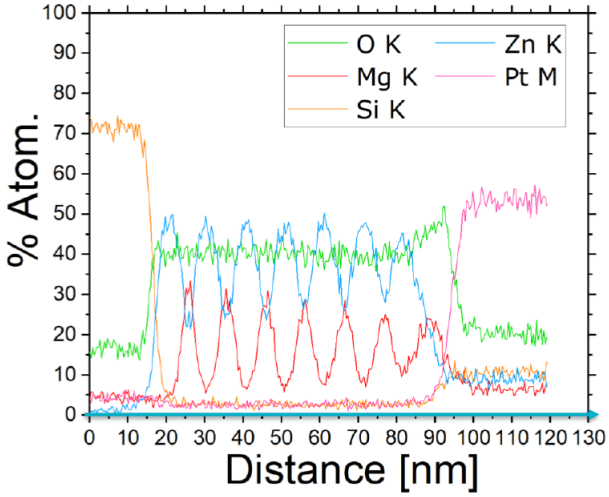

Figure 5.5: TEM EDS profile moves from the substrate (left, at 0) to the ZMO thin film surface (90nm on the right). Note that this EDS profile is inverted compared to the XPS and SIMS composition profiles.

the staring of the growth closer to the silicon substrate and the intensities begin to decrease as we move away from the substrate. This indicates an increase in roughness and/or an increased mixing of the two materials of the ZMO films with increasing number of cycles during the deposition. This behaviour is becomes clearer with TEM imaging. In Fig. 5.6, the bright-field images of the ZMO film of bilayer period 60, clearly shows distinct layers. The bright layers correspond to MgO while the grayed layers correspond to ZnO. Starting from the top, the silicon wafer, followed by a thin bright layer which indicates native oxide, we observe a thick gray layer corresponding to the first 40 successive cycles of ZnO followed by a bright layer corresponding to MgO. We observe a $\sim$ 7 nm thick ZnO layer and 2 nm thick MgO layer against thicknesses of 8.65nm for ZnO and 2.52 nm for MgO calculated respectively from the GPC of the materials. 7 distinct ZnO layers can be

observed corresponding to the 7 supercycle repetitions.

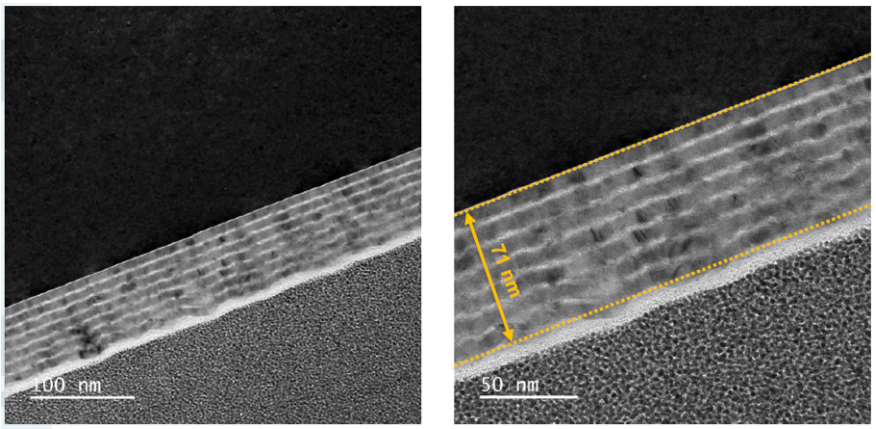

Figure 5.6: Bright-field TEM Micrographs of ZMO films of bilayer period 60. The bright layer corresponds to MgO and the dark layer denotes ZnO. The initial bright layer marks native oxide on silicon surface.

From the TEM micrographs, it can be clearly seen that at the beginning the ZnO layer and MgO layers are clearly distinct but as the film grows, the interface between ZnO and MgO becomes less distinct and precise. The roughness of MgO layer and in turn a ZnO+MgO multilayer increases with each additional layer. With increase in bilayer period, the ZnO leans towards a columnar growth which is interrupted by MgO layer and the local grains become prominent and the multilayer loses its smooth and distinct nature as more and more layers are stacked. This explains the nature of decreasing peak intensities away from the substrate observed in both SIMS and TEM elemental depth profiles.

5.3 Mixed growth regime

At small bilayer periods, BP below 10, the ternary films are well-mixed. The elemental XPS depth profiles clearly show a homogeneous film and no layered structure as can be seen from Fig. 5.7. The Zn elemental peaks are higher than Mg as expected from the pulse ratio of 0.3. All the spectra of Zn, Mg and O appear constant throughout the depth profile indicating a mixed layer as there are no distinct peaks. If roughness exists between the interfaces of the layers, the sputter-induced roughness might futher enhance it. TEM micrographs are used to analyse the mixed nature of the material further.

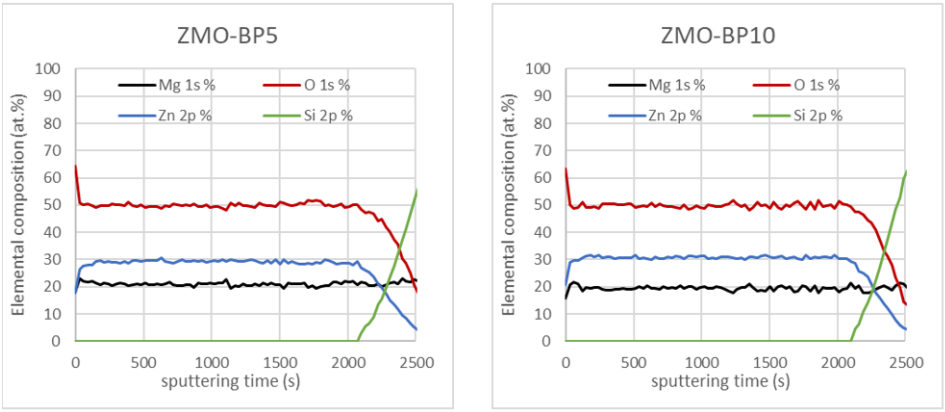

Figure 5.7: XPS depth profile of ZMO films of pulse ratio 0.3, bilayer periods 5 and 10

The TEM imaging of ZMO films with bilayer period 10 is shown in Fig. 5.8. No distinct ZnO and MgO layers can be seen from Fig. 5.8. This shows at bilayer period of 10 already, the material becomes well-mixed. Bilayer period of 10 and below result in a well-mixed homogeneous ternary material. Furthermore, we see columnar grains in the bright-field images. As a thin layer of MgO is not sufficient enough to limit the columnar growth of ZnO at small bilayer periods, we see [100] oriented grains within the mixed phase. Indeed in the XRD diffractograms of the ZMO films, we observe an increase in (100) peak intensities with decrease in bilayer period (see Fig. 4.10).

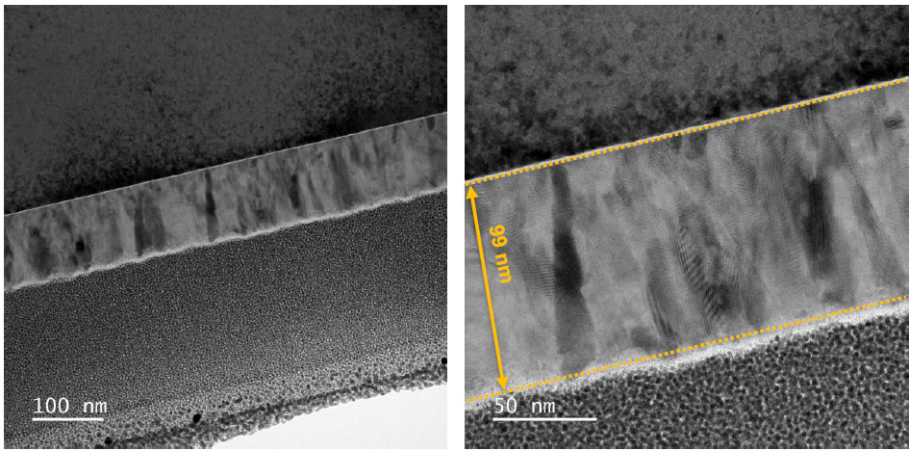

Figure 5.8: Bright-field TEM images of ZMO film of pulse ratio 0.3, bilayer period 10

From the structural variations of the films discussed in so far and from the material properties discussed in the previous chapter, at bilayer period 40 and above, the ALD grown ternary material forms layered stacks, while at bilayer periods 10 and below a well-mixed material is deposited. The interest over the transition between the nanolaminate regime to the mixed regime naturally occurs, as well as the origin of the surface roughening in the nanolaminate regime, leading to a more detailed investigation of the intermediate regime ($10 \geq BP \leq 40$).

5.4 Structural transition in ALD grown ZMO

We look into the dark-field TEM images of ZMO films of bilayer period 20 shown in Fig. 5.9, so as to investigate the structural transitions in intermediate bilayer period regime. Clearly we see distinct dark and bright layer in Fig. 5.9, where the dark and bright layers correspond to MgO and ZnO respectively.

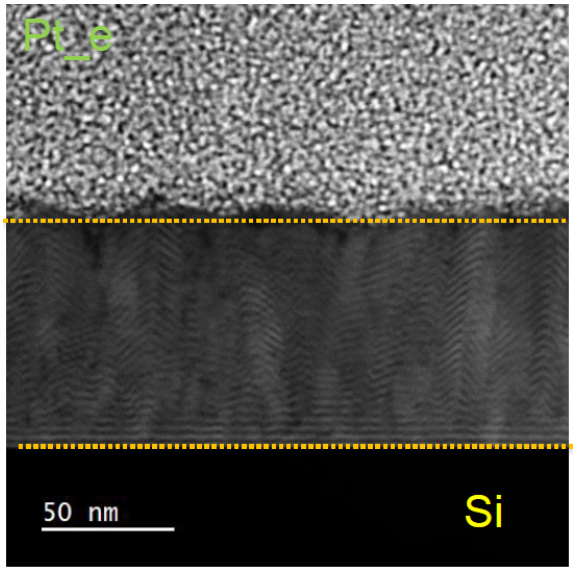

Figure 5.9: Dark-field TEM images of ZMO film of pulse ratio 0.3, bilayer period 20

Although distinct layers of ZnO and MgO can be seen, these layers are rough and exhibit columnar growth pattern across the films. Indeed we find from the high-resolution TEM micrographs, only the first three layers are parallel to the substrate and with successive cycles the layers are no longer parallel

to the substrate as can be seen in Fig. 5.10. At bilayer period 20, 6 cycles of MgO constitute a thickness of around 0.84 nm. An MgO layer of such a small thickness becomes unable to suppress the columnar growth of ZnO. Although it fails to suppress the columnar growth in the entirety of the film, it does however suppress local grain formation similar to bilayer period 10 preventing the mixture of the ZnO and MgO layers. This results in a nanolaminate film with distinguishable layers with large roughness owing to ZnO growth orientation. We can identify 24 distinct layers in the TEM image which roughly corresponds to the 26 supercycle repetitions performed during the growth of the ZMO ternary films of BP 20.

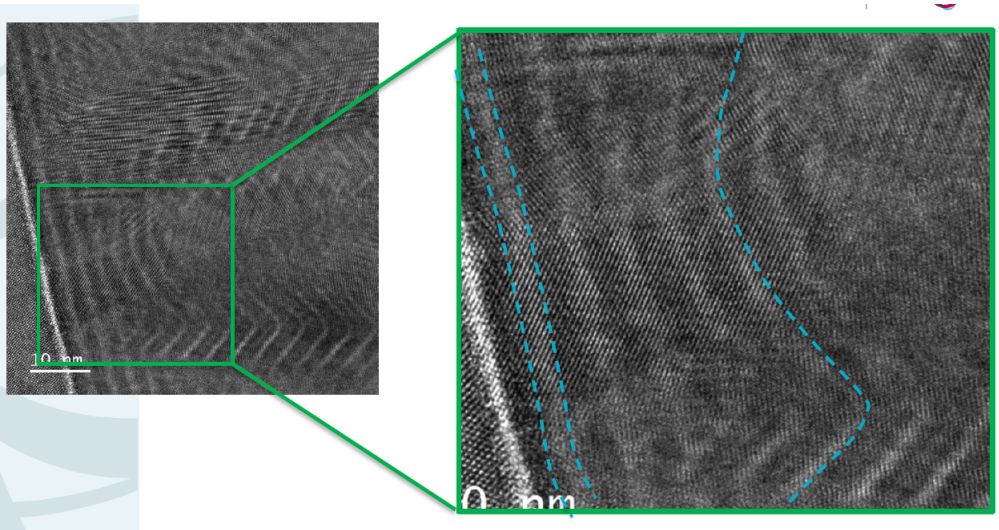

Figure 5.10: HRTEM images of ZMO film of pulse ratio 0.3, bilayer period 20

Indeed, columnar growth of ZnO leading to a rough interface layer is common and has been observed in ZnO/MgO superlattices grown by molecular beam epitaxy as shown in Fig. 5.11 [30]. A more distinct layer of MgO/ZnO can be seen in the image which is attributed to the deposition technique resulting in crystalline films and also the thickness of the MgO layer which is closer to 1 nm while in our ALD grown films it is less than 1 nm.

The intermediate bilayer periods depositing materials at the transition point between a mixed and multilayered structures, which are similar to MBE grown superlattices, can pave way towards growth of poly crystalline-amorphous superlattice structures by ALD [114].

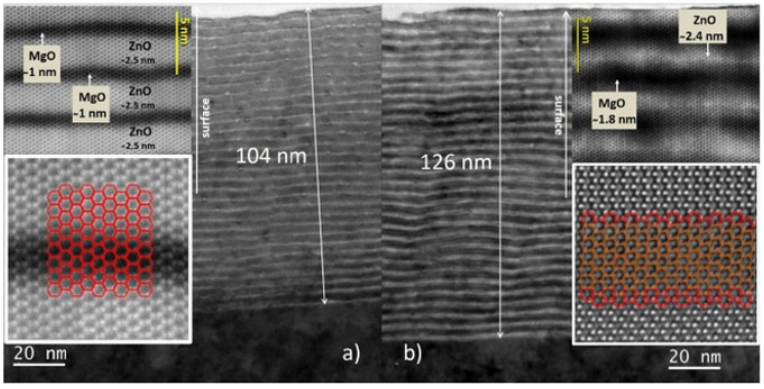

Figure 5.11: ZnO/MgO superlattices grown by MBE [30]

5.5 Conclusion

We have shown the effect of supercycle parameters on the structural variations of ALD grown ZMO thin films using surface sensitive techniques such as XPS, SIMS and TEM and confirm the change in mixed nature of the material with bilayer period proposed in the previous chapter. We have compared the resolution in depth-profiling accessible through the various techniques employed and conclude that TEM and SIMS techniques offer better insights into the structural variations of the ALD grown ternary material. We have determined that the ALD grown ternary ZMO exhibit nanolaminated structure for bilayer period 40 and above and well-mixed material forms at bilayer period 10 and below. In addition, we have identified an intermediate regime between bilayer period 10 and 40, where a structural transition occurs between the nanolaminate regime and the mixed regime.

Chapter 6

Zinc Tin Oxide by ALD

6.1 Introduction

Zinc Tin Oxide or ZTO is a wide bandgap semiconductor which has three intermediate crystalline phases, the stable zinc orthostannate Zn_2SnO_4, the metastable zinc stannate $ZnSnO_3$ which can forms either a perovskite or ilmenite structure. SnO_x ($1 \leq x \leq 2$) has rutile structure with a bandgap of 3.6 eV at room temperature [115]. Atomic layer deposition of the ternary films of $Zn_{1-x}Sn_xO_y$ uses a supercycle approach with ZnO and SnO_x binary processes.

The goal of this chapter is to understand the growth kinetics of the ALD grown ZTO films to find the optimal intermixing sequence of the respective binary materials, investigate the influence of process parameters such as deposition temperature, supercycle pulse ratio, bilayer period on the structural, optical and electrical properties of the ALD grown ZTO films. By correlating the growth kinetics with the material properties in detail, this chapter aims to develop a reliable and accurate tuning of the material properties to suit different applications.

6.2 Growth kinetics of SnO_x

Self-limited growth

Fig. 6.1 shows the growth per cycle (GPC) versus precursor dosage time for SnO_x across three different points of a 12-inch Si monitor to ensure uniformity; the different points are: one closer to the inlet of the gas, another at

the center of the Si wafer and the last one closer to the gas outlet. Saturation is achieved for the SnO_x binary ALD process at 1s TDMASn pulse and 200ms pulse of H_2O for a deposition temperature of 150 °C resulting in a uniform binary film across the 12-inch Si monitor as inferred from the Fig. 6.1. At shorter pulse time of the tin precursor, we observe a non-uniform film with varied thickness from the inlet to the outlet, which implies that the precursor dosage time is not enough to cover and saturate the whole wafer with absorbed species.

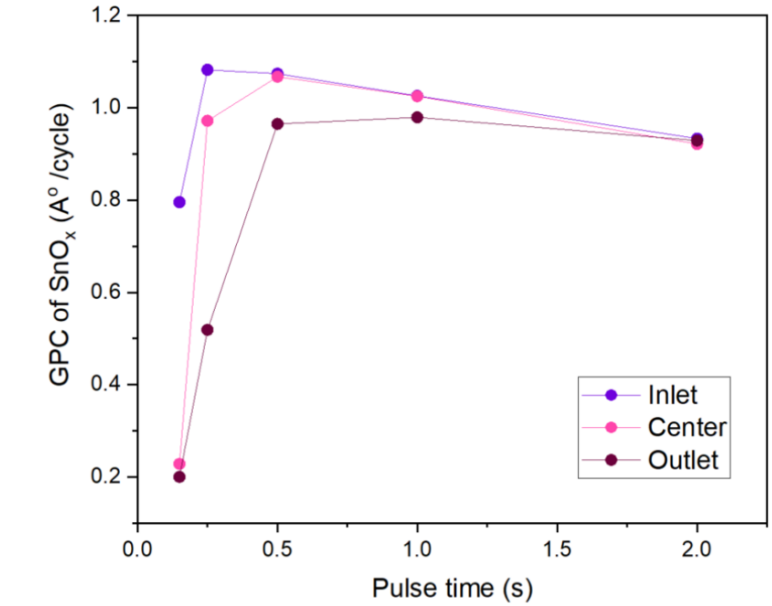

Figure 6.1: Variation of GPC versus precursor dosage time for SnO_x ALD process at 150 °C at three different positions of a 12-inch Si wafer: **inlet** - point closer to the inlet of the gas, **center** - point at the center of the Si wafer and the last position closer to the gas **outlet**.

ALD Temperature Window

With the binary ALD process of SnO_x, we find the growth of SnO_x to be highly sensitive to temperature. The growth-per-cycle (GPC) of SnO_x decreases with increase in temperature as shown in Fig. 6.2, irrespective of the carrier gas flow rate. The GPC decreases by ∼0.0122 Å/cycle for every 1°C rise in temperature. This decreasing trend of the GPC with temperature has been previously reported [116]. The binary ALD process of SnO_x shows good linearity of thickness with varying number of ALD cycles across all the deposition temperatures.

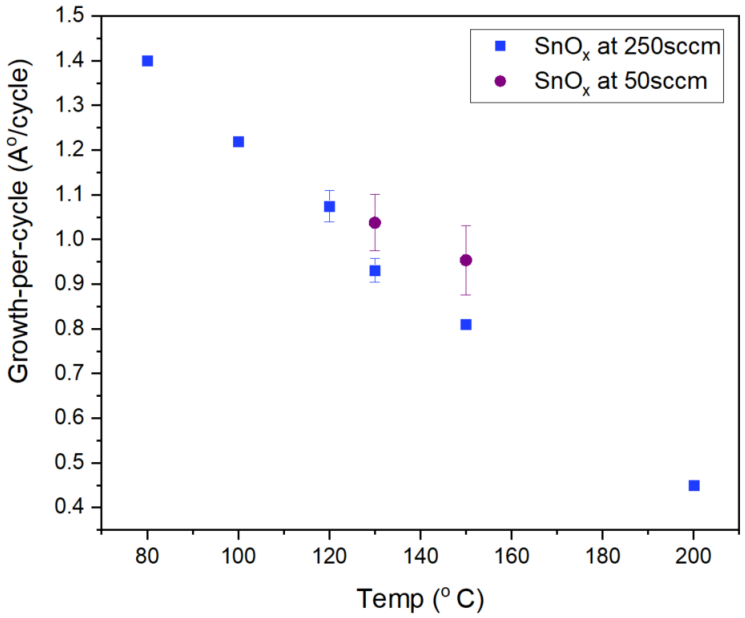

Figure 6.2: SnO_x growth vs deposition temperature for two different carrier gas flow rates (see legends).

6.3 Growth kinetics of ZTO

6.3.1 Effect of deposition temperature

The strong influence of the deposition temperature on the growth of SnO_x extends to the growth of ZTO as well. Fig. 6.3 shows the variation of GPC with deposition temperature for ALD grown pure ZnO films, SnO_x and ZTO films(PR=0.25) along with the expected GPC calculated from Eq. (2.13). We find that for a given SnO_x pulse ratio of 0.25, the GPC of ZTO films increases with temperature and then decreases beyond 130 °C in Fig. 6.3. Furthermore, the overall GPC of ZTO is less than the GPC computed after the individual binary GPC of ZnO and SnO_x based on Eq.(2.13). The GPC of ZTO is lower than the GPC of ZnO and SnO_x at 80 °C. The GPC remains lower than ZnO but is higher than SnO_x for all the temperatures. The overall trend of GPC increases until 130 °C and then decreases again at 150 °C. It is evident that in the growth of ZTO both ZnO and SnO_x cycles compete, the growth is always less than expected values, still until 130 °C the growth increases. Tanskanen et. al., investigated by DFT calculations the binding of TDMASn on -OH terminated ZnO surfaces and have shown that in the growth of ZTO, SnO_x cycle on ZnO reduces the -OH reaction site density [86]

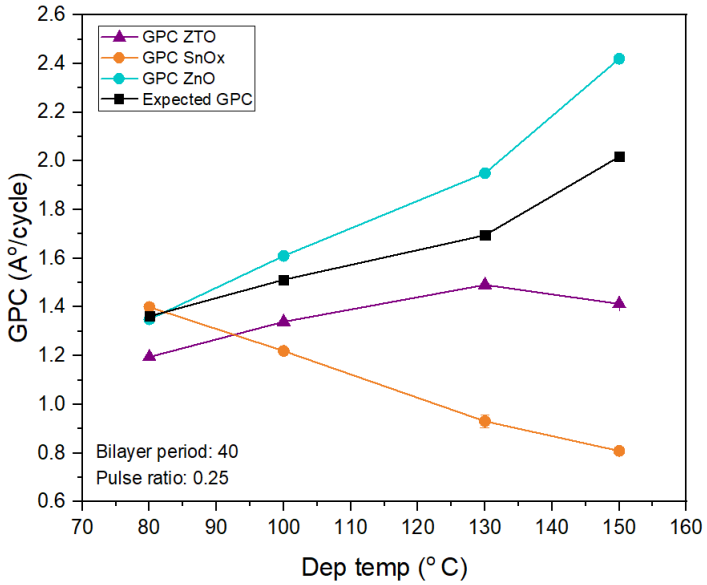

Figure 6.3: ZTO GPC vs deposition temperature for pulse ratio 0.25 at bilayer period 40 i.e pulsing sequence of 30 ZnO and 10 SnO_x. The GPC of ZnO, SnO_x, an expected GPC from Eq. (2.13) are indicated for reference.

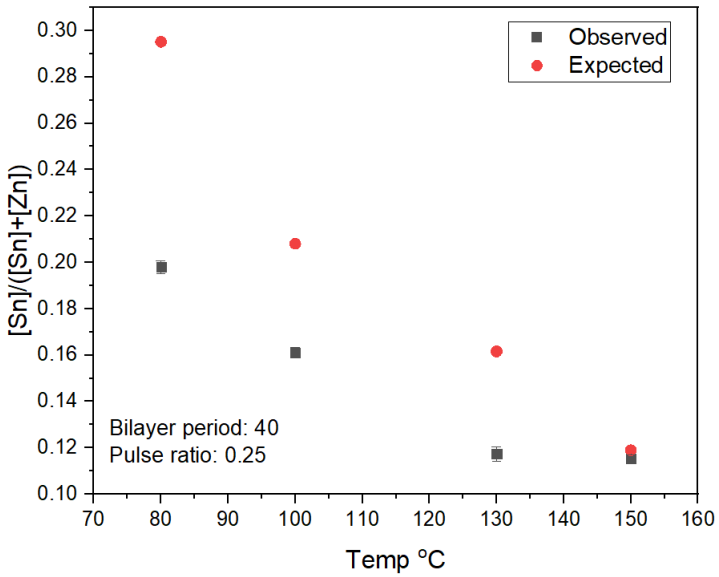

Figure 6.4: Composition vs deposition temperature of ZTO films for pulse ratio 0.25 at bilayer period 40 i.e pulsing sequence of 30 ZnO and 10 SnO_x. Expected composition determined based on Eq. (2.14).

for the chemisorption of next precursor (DEZ mostly) and is the main reason that the growth is always lower than expected values. In addition, st 150 °C there is a deviation of GPC in the observed trend.

This non-ideal growth behavior becomes apparent in the variation of composition of ZTO films deposited at different temperatures. In Fig. 6.4, we see that the Sn content decreases with increase in deposition temperature as expected qualitatively from the GPC of individual materials from (2.14). The Sn content imparted in the films is lower than the expected values determined from Eq. (2.14) until 130 °C, nonetheless it reaches the expected values at 150 °C. ZTO growth and composition as a function of deposition temperature affirms the competition of ZnO and SnO_x cycles. From Fig. 6.3 and 6.4, both the growth and composition of ZTO films are always less than the expected values until 130 °C. A complete turnaround of this behaviour occurs at 150 °C, the growth kinetics of ZTO films changes as the GPC of ZTO films fall below the expected and average values but the composition rises up to expected values. This indicates a change in the interplay between the ZnO and SnO_x cycles around 150 °C, which we investigate further by varying the pulse ratio of the ALD grown ZTO films at 150 °C.

6.3.2 Effect of varying pulse ratio

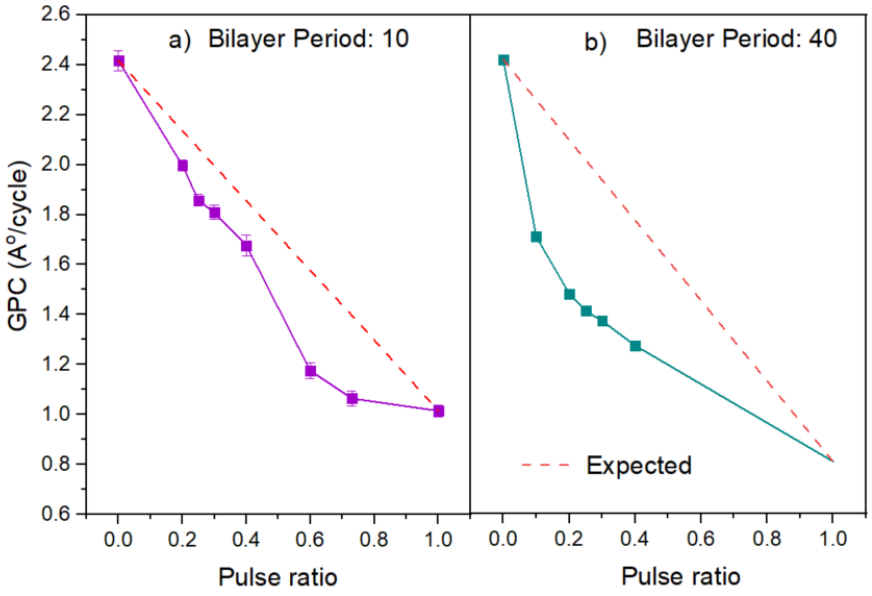

Figure 6.5: ZTO growth vs pulse ratio at 150 °C with bilayer periods (a) 10, (b) 40

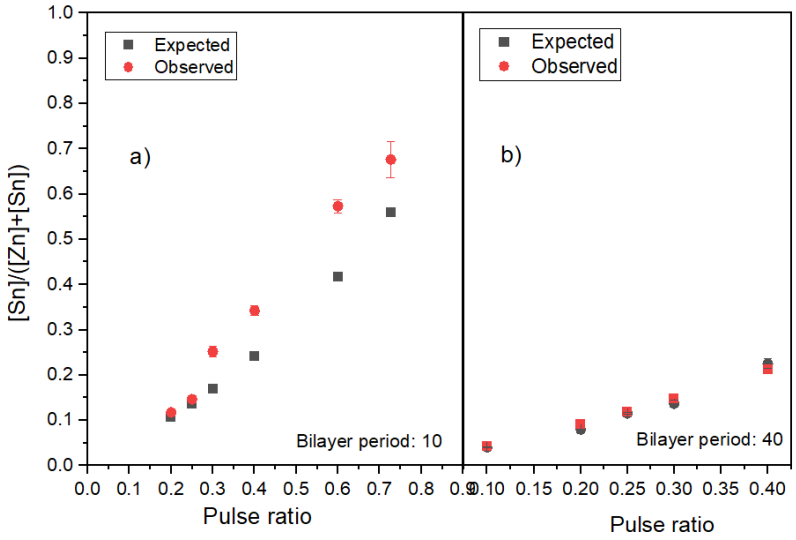

Figure 6.6: ZTO composition vs pulse ratio at 150 °C, at different bilayer periods (a) 10 (b) 40. The error bars come from measuring multiple samples of the same deposition. Note the error bars for bilayer period 40 are smaller than they symbols themselves.

We look into the growth at varying pulse ratios at 150 °C in Fig. 6.5 at two different bilayer periods (10 and 40). We observe the growth of ZTO films decreases with increasing pulse ratio as expected from (2.13), yet, the GPC of ZTO films are lower than the expected values. Now decrease of GPC with increasing pulse ratio suggests that GPC decreases with increase in number of SnO_x cycles which is expected due to the lower GPC of SnO_x and this trend remains the same across two different bilayer periods (10 and 40) in 6.5. The number of SnO_x cycles within a supercycle increases from bilayer period 10 to 40 thus leading to decreased growth in the latter compared to the former. Althouth the GPC of ZnO is higher than that of SnO_x, this higher growth of ZnO does not result in overall high GPC of ZTO. It has been suggested that reduced surface hydroxyl density as a likely cause of reduced ZTO growth [85]. To understand the competition in growth kinetics between ZnO and SnO_x, it becomes relevant to understand the compositional variation of the ZTO films with varying pulse ratios.

We plot the ZTO composition observed for varying pulse ratios for bilayer periods 10 and 40 in Fig. 6.6. At bilayer period 40, we observe Sn content exactly as expected from (2.14) same as the Sn incorporation observed as expected at the deposition temperature of 150 °C in 6.4. At lower bilayer

period of 20, the Sn composition is slightly higher than the expected values. These compositional trends point out that good Sn incorporation into ZTO films by SnO_x cycles occur at 150 °C. As the overall GPC of the ZTO films falls towards the GPC values of SnO_x with increase in pulse ratio and the Sn incorporation is favoured with increase in SnO_x cycles, in the interplay of ZnO and SnO_x cycles at 150 °C, we regard SnO_x cycles to equally compete if not outweigh the ZnO cycles over the growth. The competition between ZnO and SnO_x cycles cycles result in a non-linear growth behaviour of ZTO films, the origins of which are further explored by studying the effect of bilayer period.

6.3.3 Effect of bilayer period

ZTO growth as a function of bilayer period for different pulse ratios at 150 °C is plotted in Fig. 6.7. We find an initial rapid increase of GPC with increase in bilayer period to 10 and then the GPC slowly decreases and falls towards a more steady-state value. This growth behaviour of ZTO, as will be discussed below, can be explained in terms of the substrate-inhibited growth behaviour of type II depicted in Fig. 2.17(d).

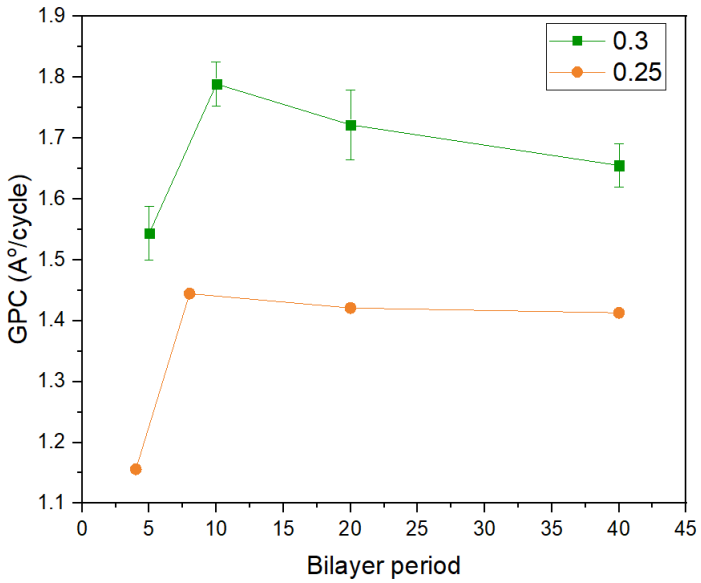

Figure 6.7: ZTO growth vs bilayer period for two pulse ratios 0.25 and 0.3 at 150 °C.

We analyse the trend in composition versus bilayer period in Fig. 6.8 to fur-

ther understand the possible substrate-inhibited growth behaviour of ZTO films. With increase in bilayer period, the Sn concentration decreases. Although at smaller bilayer periods, the Sn composition observed is higher than the expected values (BP≤20), the Sn composition falls towards expected values on further increase of bilayer period (BP=40).

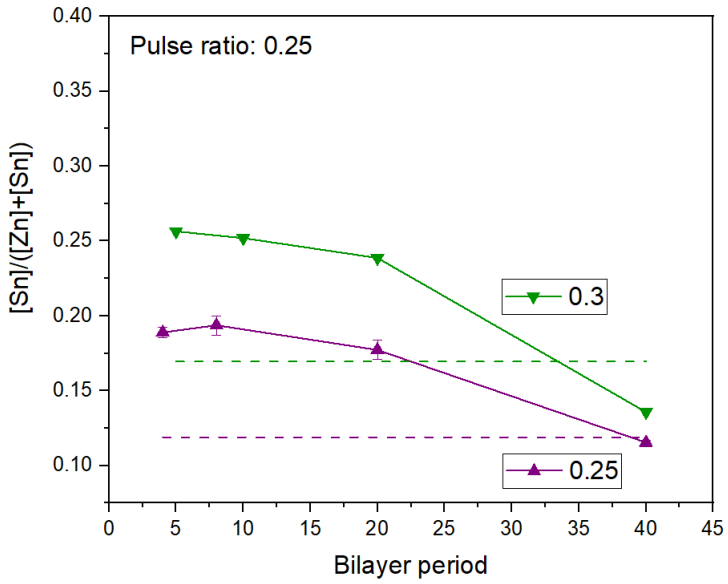

Figure 6.8: Sn composition vs bilayer period at 150 °C for pulse ratios 0.25 and 0.3

At the smallest bilayer period, the supercycle consists of only one SnO_x cycle and few ZnO cycles at pulse ratios 0.25 (3 ZnO + 1 SnO_x) and 0.3 (3 ZnO + 1 SnO_x + 3 ZnO + 1 SnO_x +1 ZnO + 1 SnO_x). The GPC is smallest at the smallest bilayer period, whereas the Sn composition is at the highest. If it was substrate-inhibited growth of SnO_x by ZnO, then the Sn content should have increased with increase in bilayer period as the number of successive SnOx cycles increase with less interruption from ZnO. However it doesn't seem to be the case as we find the Sn content to decrease with increase in bilayer period.

On the other hand, the number of successive cycles of ZnO increases with larger bilayer periods and so does the GPC of ZTO films. In fact, the GPC reaches its highest peak at a bilayer period of 10 where there is a minimum of 6 successive ZnO cycles within the supercycle. It has been reported that SnO_x retards the growth of ZnO and the GPC of ZnO is restored back to its original value after three consecutive cycles [85]. Therefore, it becomes

clear that in the growth of ZTO films, the SnO_x surface inhibits the growth of ZnO. With increasing bilayer period, disruption of ZnO growth by SnO_x cycle becomes less frequent, the consecutive cycles of ZnO will increase the reaction site density and restore the decreased growth after reduction of reaction site density by SnO_x cycle on ZnO [85] [86]. An increase in the global GPC of ZTO films is attributed to the growth of ZnO on ZnO which is observed until BP=10. For higher BP, as seen in Fig. 6.7, the global GPC decreases (for PR=0.3) and falls to a steady-state value (PR=0.25). Hagglund et al. suggested that the limited number of nucleation sites offered by SnO_x leads to a island-type growth mode of ZnO resulting in an overshooting in the GPC before reaching a steady-state value [37]. It has been shown that in the growth of SnO_x with TDMASn and H_2O, persisting DMA ligands are present on the surface and are completely eliminated only at 200°C [88]. The persisting ligands not only explain the inhibited growth of ZnO after SnO_x cycle, they can also result in retarded growth of SnO_x on SnO_x, leading to the decrease in GPC of ZTO with increase in bilayer period.

6.4 Structure-Property relationships

6.4.1 Structural properties

X-ray diffractograms of ZTO as a function of varying bilayer period is shown in Fig. 6.9 for a pulse ratio of 0.25. All the pure SnO_x films deposited exhibit an x-ray amorphous structure. In the mixing of SnO_x and ZnO into ZTO, the films with small bilayer periods are amorphous in nature similar to SnO_x. We observe ZTO films at BP 40 starts showing slight peaks and ZTO films of BP 80 shows a polycrystalline structure similar to the wurzite ZnO structure. We do not observe any peak shifts although we see a decrease in the intensity of the peaks. As the ZTO films at BP 40 starts exhibiting crystallinity, we investigate the x-ray diffractograms of ZTO films of various pulse ratios at BP 40 which are displayed in Fig. 6.10. With increasing pulse ratio, the ZTO films become x-ray amorphous. At PR of 0.1, the ZTO film shows crystalline peaks similar to wurzite ZnO, however with reduced intensity. The intensity of the peaks reduce as the pulse ratio increases. It can be inferred that as Sn composition increases with increase in pulse ratio, the ZTO films lose their crystalline nature. With addition of Sn, we see peak shift of (101) and (103) reflection by 2° towards lower angles. At PR=0.1, the (103) reflection shifts by 2° at first to a lower angle and the intensity reduces with further increase of pulse ratio finally vanishing at PR=0.3. In the same way, the (101) reflection peak shifts at PR=0.1, additional shift of

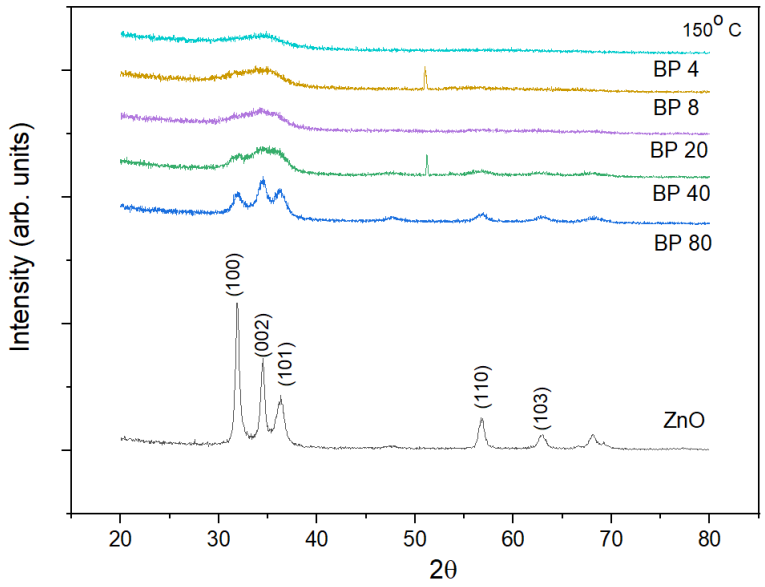

Figure 6.9: X-ray diffractograms of ZTO films with various bilayer periods for pulse ratio of 0.25 at 150 °C. ZnO diffractogram added for reference.

the peak towards lower angles occurs at PR=0.2 and with further increase in pulse ratio, finally the distinction between (002) and (101) reflection peaks is lost. Likewise with addition of Sn, the (100) reflection peak shifts to higher angles moving towards (002). We extend the analysis by looking into the peaks of ZTO films in Fig. 6.11 at PR=0.2 and 0.3. As the (101) reflection peak shifts towards (002), it matches the position of the (222) reflection peak of Zn_2SnO_4 phase and in the same manner the (100) reflection peak of ZnO is lost and the peak at 32° matches the position of the (104) reflection peak of $ZnSnO_3$ phase. We conclude that with addition of Sn, the ZTO films lose their wurzite crystalline structure and become amorphous. Although the diffractograms do not indicate any phase separation since no reflection peaks corresponding to the rutile phase of SnO_2, they do indicate presence of crystallites from ZTO mixed phases. Lindahl et al. reported presence of small ZnO(Sn) crystallites embedded into the amorphous matrix which increased in size with temperature [87]. The lack of narrow, intense peaks suggest incomplete crystallization therefore resulting in the presence of crystallites.

6.4.2 Optical properties

We correlate the bandgap of the ZTO films with the measured Sn content in Fig. 6.12. In particular, the figure depicts the variation of bandgap as a

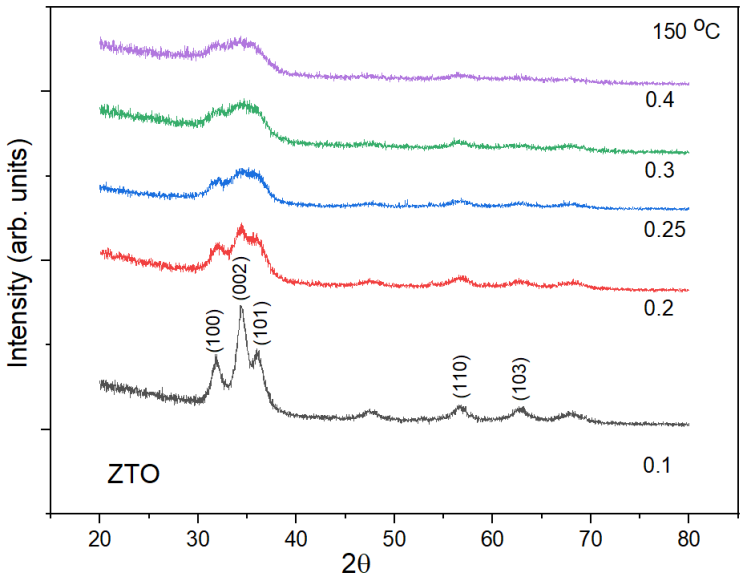

Figure 6.10: X-ray diffractograms of ZTO films at various pulse ratios from 0.1 to 0.4 at BP 40 grown at 150 °C.

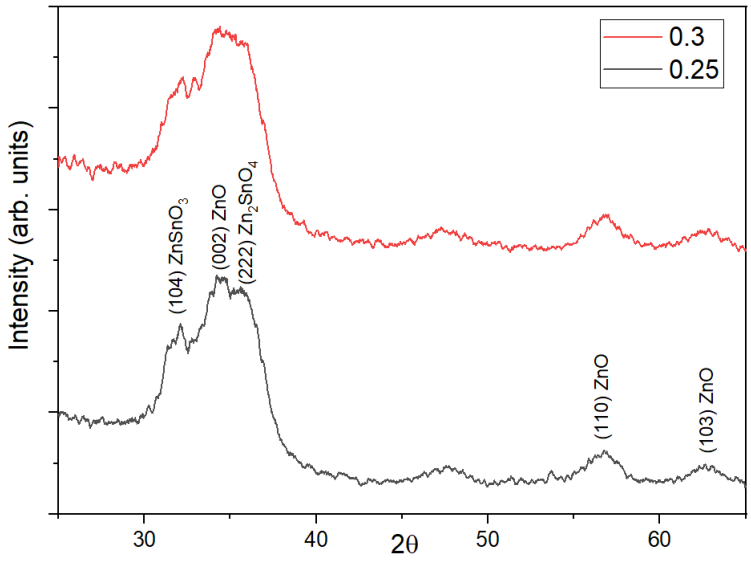

Figure 6.11: Zoomed in X-ray diffractograms of ZTO films at pulse ratios 0.25 and 0.3 at BP 40 grown at 150 °C.

function of deposition temperature and pulse ratio at bilayer period 40. We

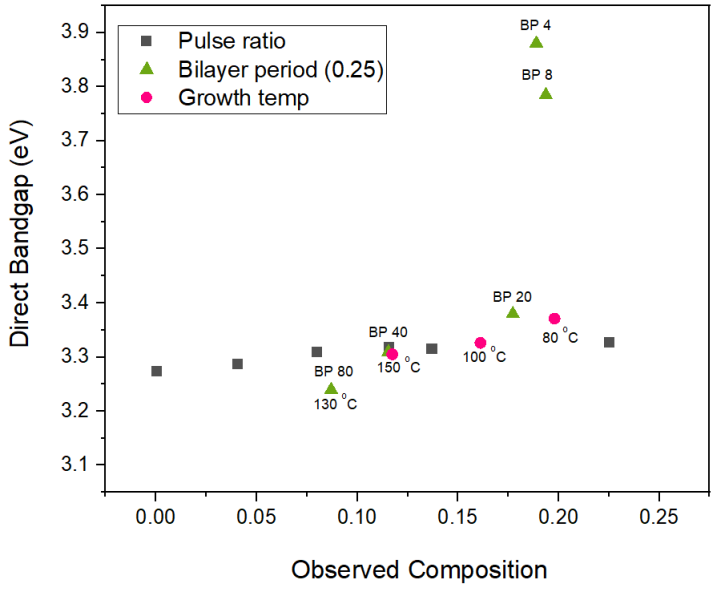

Figure 6.12: Optical bandgap vs Sn composition for various ZTO films deposited at bilayer period of 40. The black squares show variation in Sn composition as a result of the change in pulse ratio. The pink dots are the bandgap corresponding to the composition as a function of deposition temperature. The green triangles are the variation of bandgap with bilayer period.

observe bandgap widening with increasing in Sn content brought about by increase in pulse ratio. The initial increase in bandgap reduces at 15% Sn concentration and starts increasing again beyond a composition of 20% Sn. Interestingly, a similar behaviour was observed in the study of amorphous ZTO films by soft x-ray spectroscopy, where the increase in bandgap was attributed to the shift in conduction band edge and the reduction of bandgap with further addition of Sn occurred due to the shift of valence band towards higher energies [82]. Moreover, from Fig. 6.12 the variation of bandgap is found to be not directly dependent on the deposition temperature except for the ZTO film deposited at 80 °C.

The slight dependence of bandgap over the deposition temperature arises from the dependence of the composition with deposition temperature illustrated in Fig. 6.4. A decreasing trend of bandgap as a function of deposition temperature has been observed previously [87]. Presence of SnO_2 or Zn_2SnO_4 nanoparticles or crystallites embedded inside the films during growth at lower temperatures might lead to quantum confinement effects resulting in broad-

ening of the bandgap which reduces as crystallinity improves with deposition temperature [87]. A much clearer picture is obtained when we observe the variation in bandgap with Sn content for pulse ratio varying from 0.2 to 0.4 for two different bilayer period (10 and 40) in Fig. 6.13. At BP=10, we observe bandgap widening with increasing in Sn content brought about by increase in PR, meanwhile the films at BP=40 exhibit an entirely different trend with the bandgap almost constant and similar to that of pure ZnO.

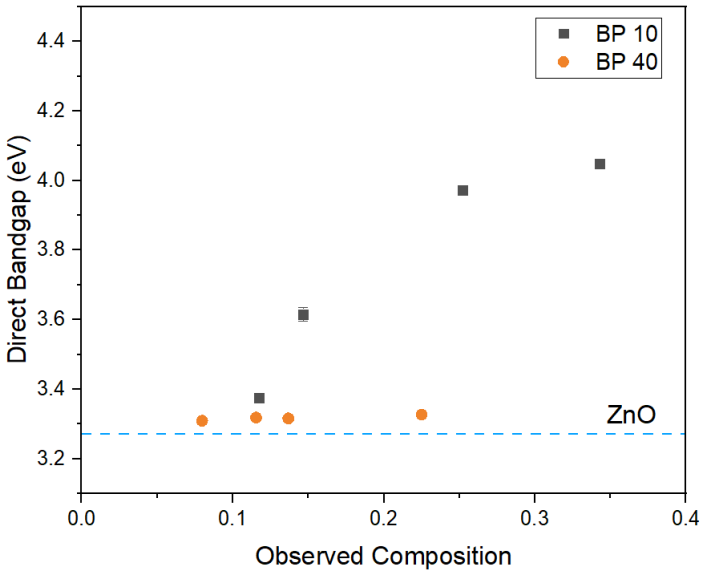

Figure 6.13: Optical bandgap vs Sn composition for PR 0.2 to 0.4 of ZTO films deposited at bilayer period 10 (black squares) and 40 (orange squares). The dashed line represents bandgap of pure ZnO films.

We observe the variation of bandgap with bilayer period is not simply due to change in composition. A better understanding of the material structure and its effect on optical properties can be gathered from Fig. 6.14 which shows the variation of bandgap as a function of bilayer period of ZTO films deposited at 150 °C.

The higher bandgap at smaller bilayer periods could possibly explained by the presence of crystallites of Zn_2SnO_4 or $ZnSnO_3$ into the amorphous structure of the material leading to quantum confinement effects [87]. Lindahl et al. observed that ZTO films consisted of small ZnO or ZnO(Sn) crystallites embedded in an amorphous matrix which increases in size with increasing zinc content and deposition temperature [87]. Fig. 6.9 clearly shows that films of smaller bilayer periods (BP$\leq$20) for PR=0.25 are x-ray amorphous.

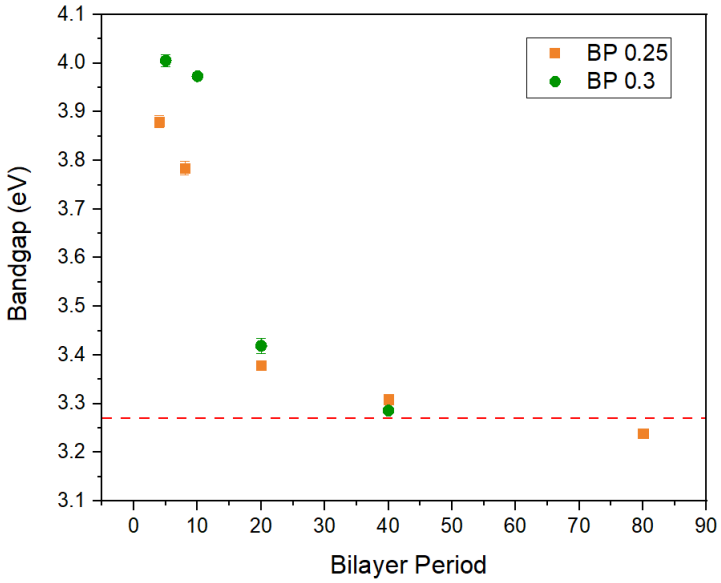

Figure 6.14: Optical bandgap vs bilayer period of ZTO films deposited at 150 °C for two different pulse ratios: 0.25(orange) and 0.3(green) with expected composition in Fig. 6.12 . The dashed red line denotes bandgap of ZnO reference.

The estimated bandgap vary from 4.3 eV for Zn_2SnO_4 nanocrystallites and 3.9 to 4.2 eV for $ZnSnO_3$[117] [118]. At smaller bilayer periods(BP≤10), the number of consecutive SnO_x cycles does not exceed 3 (for PR≤0.4). Any Sn or ZnO(Sn) based crystallite therefore should not exceed a size of ∼0.315 nm which is smaller than the Bohr radius of ZnO thus resulting in confinement from being embedded into the amorphous matrix. With increasing bilayer period, the thickness of ZnO layer and the Zn content increases (see Fig. 6.8) which can lead to an increase in crystallite size supported by Fig. 6.9 where ZTO films at BP 40 exhibit XRD peaks corresponding to different ZTO phases (the crystalline size estimated from Debye scherrer equation are *sim* 0.4 nm for BP=20 or 1.5 nm for BP=40). Another possible explanation for the bandgap variation with bilayer period is shift in conduction band edges. Higher Sn concentration causes moderate shift in conduction band edges towards higher energies [82], however this shift is suppressed by the decrease in Sn incorporation and increase in Zn content with increase in bilayer period. As in the case of ZMO, here too we conclude that BP 20 marks a transition from ZTO mixed material phase to a ZnO-dominant multilayered material.

6.4.3 Electrical properties

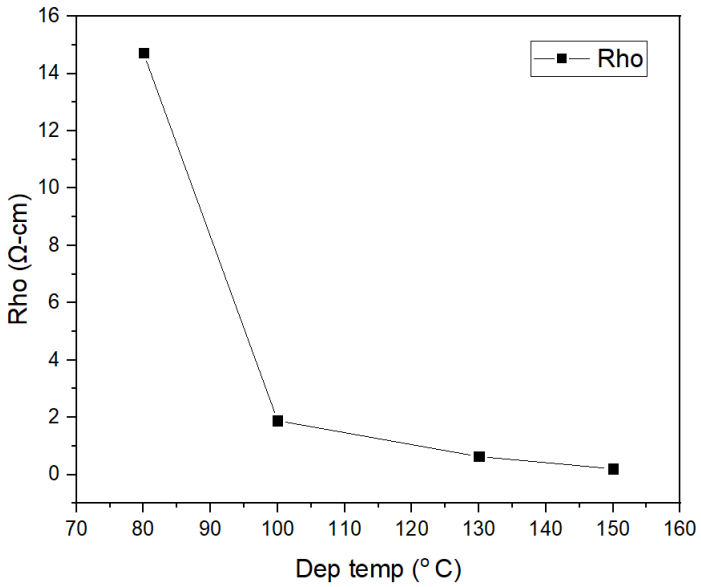

Figure 6.15: Resistivity vs Deposition temperature of ZTO films (PR=0.25, BP=40)

The electrical properties of ALD grown ZTO films are strongly dependent on the deposition temperature and the bilayer period. The change in resistivity of the ZTO films as a function of deposition temperature is shown in Fig. 6.15 where the resistivity of the films decrease with increase in process temperature. As grown ZnO thin films by ALD have high resistivity at lower deposition temperatures ($\leq$150 °C) because of their poor crystallinity. Combining this with SnO_x films that show amorphous nature at various deposition temperatures, the resulting ZTO films also show high resistivity at low deposition temperatures. As the crystallinity of the ZTO films improve with increase in deposition temperature, resistivity decreases and is lowest at 150 °C.

The other supercycle parameter that has a strong influence on the resistivity is the bilayer period, the trend of which is shown in Fig. 6.16 for ZTO films deposited at 150 °C for a PR of 0.25. With increase in bilayer period, the resistivity decreases similar to the optical bandgap. As the thickness of ZnO increases with increase in bilayer period, it provides a better conduction path for electrons, the improved crystallinity at higher bilayer period also aids.

In order to understand the influence of Sn content on the resistivity dependence over the bilayer period, we plot in Fig. 6.17 resistivity as a function

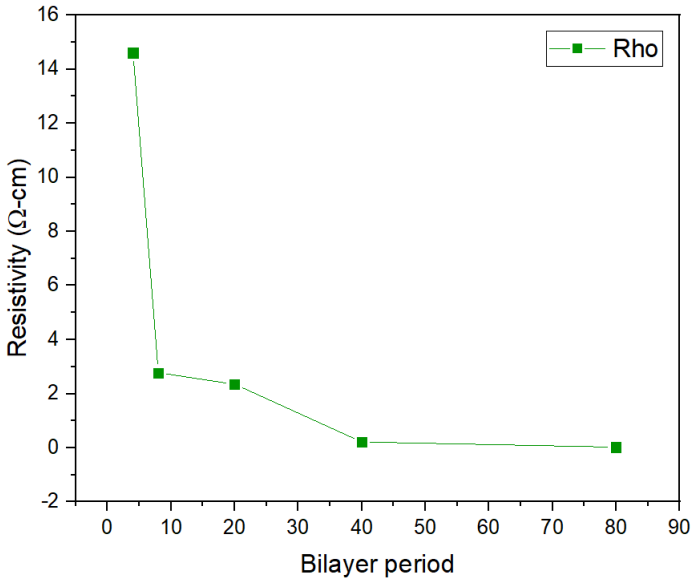

Figure 6.16: Resistivity vs Bilayer period of ZTO films (PR=0.25) grown at 150 °C

of composition for various pulse ratios and the bilayer period shown in Fig. 6.16. From Fig. 6.17, it is clear that the resistivity varies with change in Sn composition, i.e. just as the the proportion of ZnO varies. At lower composition, there is a higher proportion of ZnO present in the films which makes the films conductive as ZnO is more conductive, compared to amorphous SnO_x which is not as conductive. Another possible reason for the weak influence of pulse ratio over the resistivity could be due to the bilayer period at which the pulse ratio is varied. As at bilayer period 40, the ZTO films already behave more as a multilayered material observed from the optical properties, the increase in Sn content with pulse ratio does not have a strong influence on the resistivity since ZnO dominates the electrical properties in the multilayered structure. The mixed material observed as a result of lowering deposition temperature or smaller bilayer period shows high resistance to electrical conduction.

6.5 Conclusion

We developed a consistent and reliable thermal ZTO ALD process and used the bilayer period approach to probe the growth kinetics and confirmed that the growth of ZnO is inhibited by SnO_x surface. We performed a detailed

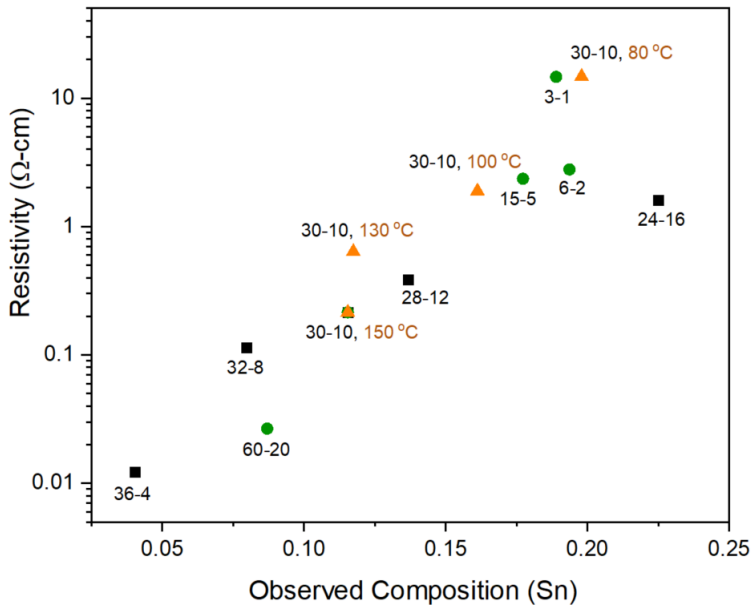

Figure 6.17: Resistivity vs Observed Sn composition, showing resistivity as a function of pulse ratio, deposition temperature and bilayer periods

analysis of the material properties with addition of Sn and the effect of mixing. We found a strong dependency of the optical properties of ZTO films over the bilayer period proving yet again the bilayer period can be used to effectively tune the material properties in ALD grown ternary films. We attribute the variation of bandgap with respect to bilayer period to the presence of ZTO nanocrystallites being embedded in the amorphous matrix of the well-mixed material at smaller bilayer periods, by examining the structural properties. Thus, we correlate the growth kinetics of the ALD grown ZTO films in detail with the structural and optical properties observed.

Chapter 7

Conclusion and Perspectives

We have established a reliable thermal ALD processes for ternary ZMO and ZTO and have verified the consistency of the process by growing the thin films under different conditions in part addressing the growing challenges of consistency and reproduceability in atomic layer deposition [119]. By probing the supercycle parameter - bilayer period, we examined the changes in growth of our thin films focusing on the first objective of this thesis - understanding the growth and mixing kinetics.

In ALD-grown ZMO thin films, through the influence of bilayer period we illuminate the interactions between ZnO and MgO interfaces and the resulting enhancement of MgO growth by ZnO surface. While in the case of ZTO films, we confirmed, again through the influence of bilayer period, that the ZnO growth is inhibited by SnO_x films. These observations support that bilayer period can be a good tool in studying the growth kinetics of ternary ALD process. In addition, with the effect of bilayer period, we determine the optimal way to mix one material with another. We found for an effective incorporation of Mg into ZnO system, interspersing one MgO cycle every 3 cycles of ZnO as necessary. On the contrary, optimal growth and Sn content of ZTO films is attained around BP=10, requiring a minimum of 6 consecutive ZnO cycles. Thus we have demonstrated the effective manner in which a metal oxide can be doped or alloyed with another metal oxide in a ternary ALD process and the use of bilayer period in understanding the mixing kinetics can be extended to other ternary ALD process. In addition, bilayer period can serve as a powerful too in understanding quarternary ALD processes where the interactions between the various ALD chemistries becomes even more complex [22].

To address the second objective, we have defined a consistent process-structure-property relationship for ALD grown ZMO and ZTO films. We have reported, for the first time, the strong dependency of the optical properties over the bilayer period and discuss possible causes. We find for both ternary ALD materials, the bandgap is highest at the smallest bilayer period suggesting the formation of a well-defined mixture of the ternary material. As the bilayer period increases (10<BP<40), the bandgap of ZMO and ZTO films decrease and for BP above 40, the bandgap values reduces to that of ZnO indicating ZnO dominance over the material properties of the ternary materials. We have suggested different mechanism for the change in bandgap with the bilayer period. In the case of ZMO, we argued the bandgap variation with bilayer period arises out of quantum confinement effects by comparing ZnO layer thickness with Bohr radius. While in the case of ZTO, we have attributed the high bandgap to formation of nanocrystallites of ZnO(Sn) or mixed phase ZTO embedded into the amorphous matrix of material. We have concluded, that as the bilayer period increases, these ternary films take on a multilayered structure with one material dominating over the other, usually ZnO in these films. Bilayer period can hence be used to tune optical properties without altering the composition of the ternary film. We have identified bilayer period as a significant supercycle parameter that can be purposed into a knob to control and design the material properties of ALD grown transparent metal oxides.

In order to understand the mixed phases of our ternary films that change with the bilayer peirod, we have explored the structural transitions in the ALD grown ZMO films using surface sensitive analytical techniques such as XPS, SIMS and TEM. With the aid of depth profiling accessible through these techniques, we have defined the various structural regimes corresponding to different bilayer periods and covered the objective of comprehending the mixing kinetics. For the smallest bilayer period, we observe a well-mixed material which defines the mixed growth regime. A nanolaminated regime occurs when distinct multi layers are grown above bilayer period 40. At an intermediate bilayer period of 20, a transitionary regime is observed where the material is neither well-mixed nor possesses a well-defined layered structure as a fine layer of MgO separates the ZnO layers although the columnar growth remains not suppressed. This transitional growth regime can pave way for new research paths through development of ALD grown superlattices [114].

We have applied ALD grown ZMO films as buffer layers for chalcopyrite solar cells by modifying their optical properties through pulse ratio, bilayer period and deposition temperature based on the process-structure-property relationships we defined. An analogous application of ZTO based buffer layers

by tuning the optical properties of the films through the various supercycle parameters explored in the thesis can be noteworthy, especially in developing graded doping profiles.

While we have delved into the optical properties, detailed investigations into the electrical properties of our ALD grown films remains open. In particular, the modulation of electrical properties using bilayer period can be interesting and their application as channel layers in TFT could provide new insights into understanding amorphous oxide semiconductors and improving device performance.

Bibliography

[1] "Market Research report." https://www.marketresearchfuture.com/reports/transparent-conductive-films-market-7642.

[2] H. Hosono and K. Ueda, "Transparent conductive oxides," *Springer Handbook of Electronic and Photonic Materials*, pp. 1–1, 2017.

[3] L. Honglin, L. Yingbo, L. Jinzhu, and Y. Ke, "First-principles study of p-type conductivity of n-al/ga/in co-doped zno," *Physica Scripta*, vol. 90, no. 2, p. 025803, 2015.

[4] A. Slassi, M. Hammi, Z. Oumekloul, A. Nid-bahami, M. Arejdal, Y. Ziat, and O. El Rhazouani, "Effect of halogens doping on transparent conducting properties of sno 2 rutile: An ab initio investigation," *Optical and Quantum Electronics*, vol. 50, pp. 1–13, 2018.

[5] A. Facchetti and T. J. Marks, "Transparent electronics," *From Synthesis to Applications*, 2010.

[6] C. Sanchez-Perez, S. C. Dixon, J. A. Darr, I. P. Parkin, and C. J. Carmalt, "Aerosol-assisted route to low-e transparent conductive gallium-doped zinc oxide coatings from pre-organized and halogen-free precursor," *Chemical Science*, vol. 11, no. 19, pp. 4980–4990, 2020.

[7] J. A. Nelson, *The physics of solar cells*. World Scientific Publishing Company, 2003.

[8] B. Orlowski, A. Pieniazek, K. Goscinski, and K. Kopalko, "Quasi fermi levels in semiconductor photovoltaic heterojunction," *Acta Physica Polonica A*, vol. 129, no. 1a, 2016.

[9] B. Salhi, "The photovoltaic cell based on cigs: principles and technologies," *Materials*, vol. 15, no. 5, p. 1908, 2022.

[10] K. Pal, K. B. Thapa, and A. Bhaduri, "A review on the current and future possibilities of copper-zinc tin sulfur thin film solar cell to in-

crease more than 20% efficiency," *Advanced Science, Engineering and Medicine*, vol. 10, no. 7-8, pp. 645–652, 2018.

[11] S. Sinha, D. K. Nandi, P. S. Pawar, S.-H. Kim, and J. Heo, "A review on atomic layer deposited buffer layers for cu (in, ga) se2 (cigs) thin film solar cells: Past, present, and future," *Solar Energy*, vol. 209, pp. 515–537, 2020.

[12] S. Hwang, L. Larina, H. Lee, S. Kim, K. S. Choi, C. Jeon, B. T. Ahn, and B. Shin, "Wet pretreatment-induced modification of cu (in, ga) se2/cd-free zntio buffer interface," *ACS applied materials & interfaces*, vol. 10, no. 24, pp. 20920–20928, 2018.

[13] S. Spiering, A. Nowitzki, F. Kessler, M. Igalson, and H. A. Maksoud, "Optimization of buffer-window layer system for cigs thin film devices with indium sulphide buffer by in-line evaporation," *Solar Energy Materials and Solar Cells*, vol. 144, pp. 544–550, 2016.

[14] C. Bugot, M. Bouttemy, N. Schneider, A. Etcheberry, D. Lincot, and F. Donsanti, "New insights on the chemistry of plasma-enhanced atomic layer deposition of indium oxysulfide thin films and their use as buffer layers in cu (in, ga) se2 thin film solar cell," *Journal of Vacuum Science & Technology A*, vol. 36, no. 6, 2018.

[15] J. Lindahl, J. Keller, O. Donzel-Gargand, P. Szaniawski, M. Edoff, and T. Törndahl, "Deposition temperature induced conduction band changes in zinc tin oxide buffer layers for cu (in, ga) se2 solar cells," *Solar Energy Materials and Solar Cells*, vol. 144, pp. 684–690, 2016.

[16] M. Nakamura, K. Yamaguchi, Y. Kimoto, Y. Yasaki, T. Kato, and H. Sugimoto, "Cd-free cu (in, ga)(se, s) 2 thin-film solar cell with record efficiency of 23.35%," *IEEE Journal of Photovoltaics*, vol. 9, no. 6, pp. 1863–1867, 2019.

[17] S. Ishizuka, J. Nishinaga, T. Koida, and H. Shibata, "An over 18%-efficient completely buffer-free cu (in, ga) se2 solar cell," *Applied Physics Express*, vol. 11, no. 7, p. 075502, 2018.

[18] W. Chen, X. Pan, H. Zhang, Z. Ye, P. Ding, S. Chen, J. Huang, and B. Lu, "Small valence band offsets of non-polar zno/zn1- xmgxo heterojunctions measured by x-ray photoelectron spectroscopy," *Physics Letters A*, vol. 378, no. 30-31, pp. 2312–2316, 2014.

[19] S. R. Thomas, P. Pattanasattayavong, and T. D. Anthopoulos, "Solution-processable metal oxide semiconductors for thin-film transis-

tor applications," *Chemical Society Reviews*, vol. 42, no. 16, pp. 6910–6923, 2013.

[20] W. Lu, Y. Dong, C. Li, Y. Xia, B. Liu, J. Xie, N. Li, and Y. Zhang, "Preparation of zno films with variable electric field-assisted atomic layer deposition technique," *Applied surface science*, vol. 303, pp. 111–117, 2014.

[21] R. L. Puurunen, "Surface chemistry of atomic layer deposition: A case study for the trimethylaluminum/water process," *Journal of applied physics*, vol. 97, no. 12, p. 9, 2005.

[22] A. J. Mackus, J. R. Schneider, C. MacIsaac, J. G. Baker, and S. F. Bent, "Synthesis of doped, ternary, and quaternary materials by atomic layer deposition: a review," *Chemistry of Materials*, vol. 31, no. 4, pp. 1142–1183, 2018.

[23] H. Tompkins and J. Hilfiker, *Spectroscopic Ellipsometry: Practical Application to Thin Film Characterization*. Momentum Press, 2015.

[24] M. Ezzahmouly, A. Elmoutaouakkil, M. Ed-Dhahraouy, H. Khallok, A. Elouahli, A. Mazurier, A. ElAlbani, and Z. Hatim, "Micro-computed tomographic and sem study of porous bioceramics using an adaptive method based on the mathematical morphological operations," *Heliyon*, vol. 5, no. 12, 2019.

[25] R. H. Bube, *Electrons in solids: an introductory survey*. Academic press, 1992.

[26] Q. Peng, A. U. Mane, and J. W. Elam, "Nanometer-thick mg x zn (1–x) o ternary films for photovoltaics," *ACS Applied Nano Materials*, vol. 3, no. 8, pp. 7732–7742, 2020.

[27] P. Gnanasambandan, N. Adjeroud, and R. Leturcq, "Role of zno and mgo interfaces on the growth and optoelectronic properties of atomic layer deposited zn1- x mgxo films," *Journal of Vacuum Science & Technology A: Vacuum, Surfaces, and Films*, vol. 40, no. 6, p. 062413, 2022.

[28] A. Ohtomo, M. Kawasaki, T. Koida, K. Masubuchi, H. Koinuma, Y. Sakurai, Y. Yoshida, T. Yasuda, and Y. Segawa, "Mg x zn 1- x o as a ii–vi widegap semiconductor alloy," *Applied physics letters*, vol. 72, no. 19, pp. 2466–2468, 1998.

[29] M. Sood, P. nasambandan, D. Adeleye, S. Shukla, N. Adjeroud, R. Leturcq, and S. Siebentritt, "Electrical barriers and their elimination by tuning (zn, mg) o buffer composition in cu (in, ga) s2 solar cells:

systematic approach to achieve over 14% power conversion efficiency," *Journal of Physics: Energy*, vol. 4, no. 4, p. 045005, 2022.

[30] M. Stachowicz, A. Wierzbicka, J. Sajkowski, M. Pietrzyk, P. Dłużewski, E. Dynowska, J. Dyczewski, K. Morawiec, S. Kryvyi, S. Magalhães, *et al.*, "Structural analysis of the zno/mgo superlattices on a-polar zno substrates grown by mbe," *Applied Surface Science*, vol. 587, p. 152830, 2022.

[31] B. Macco and W. Kessels, "Atomic layer deposition of conductive and semiconductive oxides," *Applied Physics Reviews*, vol. 9, no. 4, 2022.

[32] J.-L. Yang, K.-W. Liu, and D.-Z. Shen, "Recent progress of znmgo ultraviolet photodetector," *Chinese Physics B*, vol. 26, no. 4, p. 047308, 2017.

[33] D. Hariskos, B. Fuchs, R. Menner, N. Naghavi, C. Hubert, D. Lincot, and M. Powalla, "The zn (s, o, oh)/znmgo buffer in thin-film cu (in, ga)(se, s) 2-based solar cells part ii: magnetron sputtering of the znmgo buffer layer for in-line co-evaporated cu (in, ga) se2 solar cells," *Progress in Photovoltaics: Research and Applications*, vol. 17, no. 7, pp. 479–488, 2009.

[34] J. Seo and H. Yoo, "Zinc–tin oxide film as an earth-abundant material and its versatile applications to electronic and energy materials," *Membranes*, vol. 12, no. 5, p. 485, 2022.

[35] N. Naghavi, D. Abou-Ras, N. Allsop, N. Barreau, S. Bücheler, A. Ennaoui, C.-H. Fischer, C. Guillen, D. Hariskos, J. Herrero, *et al.*, "Buffer layers and transparent conducting oxides for chalcopyrite cu (in, ga)(s, se) 2 based thin film photovoltaics: present status and current developments," *Progress in Photovoltaics: Research and Applications*, vol. 18, no. 6, pp. 411–433, 2010.

[36] T. Törndahl, C. Platzer-Björkman, J. Kessler, and M. Edoff, "Atomic layer deposition of zn1- xmgxo buffer layers for cu (in, ga) se2 solar cells," *Progress in Photovoltaics: Research and applications*, vol. 15, no. 3, pp. 225–235, 2007.

[37] C. Hägglund, T. Grehl, J. T. Tanskanen, Y. S. Yee, M. N. Mullings, A. J. Mackus, C. MacIsaac, B. M. Clemens, H. H. Brongersma, and S. F. Bent, "Growth, intermixing, and surface phase formation for zinc tin oxide nanolaminates produced by atomic layer deposition," *Journal of Vacuum Science & Technology A*, vol. 34, no. 2, 2016.

[38] K. Badeker, "Über die elektrische leitfahigkeit und die thermoelektrische kraft einiger schwermetallverbindungen," *Annalen der Physik*, vol. 327, no. 4, pp. 749–766, 1907.

[39] H. Deng, K. J. Leedle, Y. Miao, D. S. Black, K. E. Urbanek, J. McNeur, M. Kozák, A. Ceballos, P. Hommelhoff, O. Solgaard, *et al.*, "Gallium oxide for high-power optical applications," *Advanced Optical Materials*, vol. 8, no. 7, p. 1901522, 2020.

[40] A. N. Fioretti and M. Morales-Masis, "Bridging the p-type transparent conductive materials gap: synthesis approaches for disperse valence band materials," *Journal of Photonics for Energy*, vol. 10, no. 4, pp. 042002–042002, 2020.

[41] S. M. Sze, Y. Li, and K. K. Ng, *Physics of semiconductor devices*. John wiley & sons, 2021.

[42] R. F. Pierret and G. W. Neudeck, *Advanced semiconductor fundamentals*, vol. 6. Addison-Wesley Reading, MA, 1987.

[43] J. Bellingham, W. Phillips, and C. Adkins, "Electrical and optical properties of amorphous indium oxide," *Journal of Physics: Condensed Matter*, vol. 2, no. 28, p. 6207, 1990.

[44] M. Grundmann, H. Frenzel, A. Lajn, M. Lorenz, F. Schein, and H. Von Wenckstern, "Transparent semiconducting oxides: Materials and devices," *Physica status solidi (a)*, vol. 207, no. 6, pp. 1437–1449, 2010.

[45] E. Burstein, "Anomalous optical absorption limit in insb," *Physical review*, vol. 93, no. 3, p. 632, 1954.

[46] T. S. Moss, "The interpretation of the properties of indium antimonide," *Proceedings of the Physical Society. Section B*, vol. 67, p. 775, oct 1954.

[47] K. Chopra, S. Major, and D. Pandya, "Transparent conductors—a status review," *Thin solid films*, vol. 102, no. 1, pp. 1–46, 1983.

[48] L.-N. Bai, J.-S. Lian, and Q. Jiang, "Optical and electronic properties of wurtzite structure zn1- xmgxo alloys," *Chinese Physics Letters*, vol. 28, no. 11, p. 117101, 2011.

[49] N. W. Ashcroft and N. D. Mermin, *Solid state physics*. Cengage Learning, 2022.

[50] M. Powalla, S. Paetel, D. Hariskos, R. Wuerz, F. Kessler, P. Lechner, W. Wischmann, and T. M. Friedlmeier, "Advances in cost-efficient thin-film photovoltaics based on cu (in, ga) se2," *Engineering*, vol. 3, no. 4, pp. 445–451, 2017.

[51] B. Kim and B. K. Min, "Strategies toward highly efficient cigse thin-film solar cells fabricated by sequential process," *Sustainable Energy & Fuels*, vol. 2, no. 8, pp. 1671–1685, 2018.

[52] S. Siebentritt and T. Weiss, "Chalcopyrite solar cells—state-of-the-art and options for improvement," *Science China Physics, Mechanics & Astronomy*, vol. 66, no. 1, p. 217301, 2023.

[53] M. A. Green, E. D. Dunlop, M. Yoshita, N. Kopidakis, K. Bothe, G. Siefer, and X. Hao, "Solar cell efficiency tables (version 62)," tech. rep., National Renewable Energy Laboratory (NREL), Golden, CO (United States), 2023.

[54] B. Tell, J. Shay, and H. Kasper, "Electrical properties, optical properties, and band structure of cuga s 2 and cuin s 2," *Physical review B*, vol. 4, no. 8, p. 2463, 1971.

[55] T. Tinoco, C. Rincón, M. Quintero, and G. S. Pérez, "Phase diagram and optical energy gaps for cuinyga1- yse2 alloys," *physica status solidi (a)*, vol. 124, no. 2, pp. 427–434, 1991.

[56] M. Kemell, M. Ritala, and M. Leskelä, "Thin film deposition methods for cuinse 2 solar cells," *Critical Reviews in Solid State and Materials Sciences*, vol. 30, no. 1, pp. 1–31, 2005.

[57] P. Jackson, R. Wuerz, D. Hariskos, E. Lotter, W. Witte, and M. Powalla, "Effects of heavy alkali elements in cu (in, ga) se2 solar cells with efficiencies up to 22.6%," *physica status solidi (RRL)–Rapid Research Letters*, vol. 10, no. 8, pp. 583–586, 2016.

[58] R. Carron, S. Nishiwaki, T. Feurer, R. Hertwig, E. Avancini, J. Löckinger, S.-C. Yang, S. Buecheler, and A. N. Tiwari, "Advanced alkali treatments for high-efficiency cu (in, ga) se2 solar cells on flexible substrates," *Advanced Energy Materials*, vol. 9, no. 24, p. 1900408, 2019.

[59] R. Scheer and H.-W. Schock, *Chalcogenide photovoltaics: physics, technologies, and thin film devices*. John Wiley & Sons, 2011.

[60] M. Sood, J. Bombsch, A. Lomuscio, S. Shukla, C. Hartmann, J. Frisch, W. Bremsteller, S. Ueda, R. G. Wilks, M. Bar, *et al.*, "Origin of in-

terface limitation in zn (o, s)/cuins2-based solar cells," *ACS Applied Materials & Interfaces*, vol. 14, no. 7, pp. 9676–9684, 2022.

[61] E. Yousfi, T. Asikainen, V. Pietu, P. Cowache, M. Powalla, and D. Lincot, "Cadmium-free buffer layers deposited by atomic later epitaxy for copper indium diselenide solar cells," *Thin Solid Films*, vol. 361, pp. 183–186, 2000.

[62] T. Minemoto, H. Takakura, Y. Hamakawa, Y. Hashimoto, S. Nishiwaki, and T. Negami, "Highly efficient cd-free cu (in, ga) se2 solar cells using novel window layer of (zn, mg) o films," in *Proceedings of the 28th European Photovoltaic Solar Energy Conference, Paris*, vol. 1, pp. 686–689, 2000.

[63] T. Glatzel, S. Roon, S. Sadewasser, R. Klenk, A. Jäger-Waldau, and M. Lux-Steiner, "(zn,mg)o as window layer for cd-free chalcopyrite solar cells," 10 2001.

[64] T. Glatzel, S. von Roon, S. Sadewasser, R. Klenk, A. Jäger-Waldau, and M. C. Lux-Steiner, "O as window layer for cd-free chalcopyrite solar cells," in *Proceedings of the 17th European Photovoltaic Solar Energy Conference and Exhibition, Munich*, pp. 1151–1154, 2001.

[65] C.-H. Fischer, M. Bär, T. Glatzel, I. Lauermann, and M. Lux-Steiner, "Interface engineering in chalcopyrite thin film solar devices," *Solar energy materials and solar cells*, vol. 90, no. 10, pp. 1471–1485, 2006.

[66] J. Pettersson, C. Platzer-Björkman, and M. Edoff, "Temperature-dependent current-voltage and lightsoaking measurements on cu (in, ga) se2 solar cells with ald-zn1-xmgxo buffer layers," *Progress in Photovoltaics: Research and Applications*, vol. 17, no. 7, pp. 460–469, 2009.

[67] C. Platzer-Björkman, T. Törndahl, A. Hultqvist, J. Kessler, and M. Edoff, "Optimization of ald-(zn, mg) o buffer layers and (zn, mg) o/cu (in, ga) se2 interfaces for thin film solar cells," *Thin Solid Films*, vol. 515, no. 15, pp. 6024–6027, 2007.

[68] S. Kim, C.-S. Lee, S. Kim, R. Chalapathy, E. A. Al-Ammar, and B. T. Ahn, "Understanding the light soaking effect of znmgo buffer in cigs solar cells," *Physical Chemistry Chemical Physics*, vol. 17, no. 29, pp. 19222–19229, 2015.

[69] R. Hertwig, S. Nishiwaki, M. Ochoa, S.-C. Yang, T. Feurer, E. Gilshtein, A. N. Tiwari, and R. Carron, "Ald-znmgo and absorber

surface modifications to substitute cds buffer layers in co-evaporated cigse solar cells," *EPJ Photovoltaics*, vol. 11, p. 12, 2020.

[70] J. Heo, S. Bok Kim, and R. G. Gordon, "Atomic layer deposited zinc tin oxide channel for amorphous oxide thin film transistors," *Applied Physics Letters*, vol. 101, no. 11, 2012.

[71] B. D. Ahn, D.-w. Choi, C. Choi, and J.-S. Park, "The effect of the annealing temperature on the transition from conductor to semiconductor behavior in zinc tin oxide deposited atomic layer deposition," *Applied Physics Letters*, vol. 105, no. 9, 2014.

[72] C. R. Allemang, T. H. Cho, O. Trejo, S. Ravan, R. E. Rodríguez, N. P. Dasgupta, and R. L. Peterson, "High-performance zinc tin oxide tfts with active layers deposited by atomic layer deposition," *Advanced Electronic Materials*, vol. 6, no. 7, p. 2000195, 2020.

[73] C. R. Allemang, T. H. Cho, N. P. Dasgupta, and R. L. Peterson, "Robustness of passivated ald zinc tin oxide tfts to aging and bias stress," *IEEE Transactions on Electron Devices*, vol. 69, no. 12, pp. 6776–6782, 2022.

[74] T. L. Newsom, C. R. Allemang, T. H. Cho, N. P. Dasgupta, and R. L. Peterson, "59.9 mv· dec subthreshold swing achieved in zinc tin oxide tfts with in situ atomic layer deposited alo gate insulator," *IEEE Electron Device Letters*, vol. 44, no. 1, pp. 72–75, 2022.

[75] J. S. Kim, Y. Jang, S. Kang, Y. Lee, K. Kim, W. Kim, W. Lee, and C. S. Hwang, "Substrate-dependent growth behavior of atomic-layer-deposited zinc oxide and zinc tin oxide thin films for thin-film transistor applications," *The Journal of Physical Chemistry C*, vol. 124, no. 49, pp. 26780–26792, 2020.

[76] T. Törndahl, E. Coronel, A. Hultqvist, C. Platzer-Björkman, K. Leifer, and M. Edoff, "The effect of zn1-xmgxo buffer layer deposition temperature on cu (in, ga) se2 solar cells: A study of the buffer/absorber interface," *Progress in Photovoltaics: Research and Applications*, vol. 17, no. 2, pp. 115–125, 2009.

[77] G. Luka, B. Witkowski, L. Wachnicki, K. Goscinski, R. Jakiela, E. Guziewicz, M. Godlewski, E. Zielony, P. Bieganski, E. Placzek-Popko, *et al.*, "Atomic layer deposition of zn 1- x mg x o: Al transparent conducting films," *Journal of Materials Science*, vol. 49, pp. 1512–1518, 2014.

[78] I. Cora, Z. Baji, Z. Fogarassy, Z. Szabó, and B. Pécz, "Structural study of mgo and mg-doped zno thin films grown by atomic layer deposition," *Materials Science in Semiconductor Processing*, vol. 93, pp. 6–11, 2019.

[79] M. Werner, J. W. Roberts, R. J. Potter, K. Dawson, and P. R. Chalker, "Elucidation of ald mgzno deposition processes using low energy ion scattering," *Journal of Vacuum Science & Technology A*, vol. 36, no. 2, 2018.

[80] W.-S. Choi, "Preparation of zinc-tin-oxide thin film by using an atomic layer deposition methodology," *Journal of the Korean Physical Society*, vol. 57, no. 6, pp. 1472–1476, 2010.

[81] Y. S. Lee, J. Heo, S. C. Siah, J. P. Mailoa, R. E. Brandt, S. B. Kim, R. G. Gordon, and T. Buonassisi, "Ultrathin amorphous zinc-tin-oxide buffer layer for enhancing heterojunction interface quality in metal-oxide solar cells," *Energy & Environmental Science*, vol. 6, no. 7, pp. 2112–2118, 2013.

[82] M. Kapilashrami, C. X. Kronawitter, T. Törndahl, J. Lindahl, A. Hultqvist, W.-C. Wang, C.-L. Chang, S. S. Mao, and J. Guo, "Soft x-ray characterization of zn 1- x sn x o y electronic structure for thin film photovoltaics," *Physical chemistry chemical physics*, vol. 14, no. 29, pp. 10154–10159, 2012.

[83] A. Hultqvist, M. Edoff, and T. Törndahl, "Evaluation of znó snó o buffer layers for cuin0. 5ga0. 5se2 solar cells," *Progress in Photovoltaics: Research and Applications*, vol. 19, no. 4, pp. 478–481, 2011.

[84] A. Hultqvist, C. Platzer-Björkman, U. Zimmermann, M. Edoff, and T. Törndahl, "Growth kinetics, properties, performance, and stability of atomic layer deposition zn–sn–o buffer layers for cu (in, ga) se2 solar cells," *Progress in Photovoltaics: Research and Applications*, vol. 20, no. 7, pp. 883–891, 2012.

[85] M. N. Mullings, C. Hägglund, J. T. Tanskanen, Y. Yee, S. Geyer, and S. F. Bent, "Thin film characterization of zinc tin oxide deposited by thermal atomic layer deposition," *Thin Solid Films*, vol. 556, pp. 186–194, 2014.

[86] J. T. Tanskanen, C. Hagglund, and S. F. Bent, "Correlating growth characteristics in atomic layer deposition with precursor molecular structure: The case of zinc tin oxide," *Chemistry of Materials*, vol. 26, no. 9, pp. 2795–2802, 2014.

[87] J. Lindahl, C. Hägglund, J. T. Wätjen, M. Edoff, and T. Törndahl, "The effect of substrate temperature on atomic layer deposited zinc tin oxide," *Thin Solid Films*, vol. 586, pp. 82–87, 2015.

[88] A. J. Mackus, C. MacIsaac, W.-H. Kim, and S. F. Bent, "Incomplete elimination of precursor ligands during atomic layer deposition of zinc-oxide, tin-oxide, and zinc-tin-oxide," *The Journal of Chemical Physics*, vol. 146, no. 5, 2017.

[89] Y. Gu, J.-J. Tao, T. Wang, Y.-H. Liu, B.-F. Peng, L.-Y. Zhu, and H.-L. Lu, "Nonlinear growth of zinc tin oxide thin films prepared by atomic layer deposition," *Ceramics International*, vol. 47, no. 16, pp. 22760–22767, 2021.

[90] F. Izumi, "Pattern-fitting structure refinement of tin (ii) oxide," *Journal of Solid State Chemistry*, vol. 38, no. 3, pp. 381–385, 1981.

[91] E. J. Warner, F. Johnson, S. A. Campbell, and W. L. Gladfelter, "Atomic layer deposition of tin oxide and zinc tin oxide using tetraethyltin and ozone," *Journal of Vacuum Science & Technology A*, vol. 33, no. 2, 2015.

[92] J. H. Han, B. K. Lee, E. A. Jung, H.-S. Kim, S. J. Kim, C. G. Kim, T.-M. Chung, and K.-S. An, "Growth of amorphous zinc tin oxide films using plasma-enhanced atomic layer deposition from bis (1-dimethylamino-2-methyl-2propoxy) tin, diethylzinc, and oxygen plasma," *Applied Surface Science*, vol. 357, pp. 672–677, 2015.

[93] J. Zeng, M. Xin, K. Li, H. Wang, H. Yan, and W. Zhang, "Transformation process and photocatalytic activities of hydrothermally synthesized zn2sno4 nanocrystals," *The Journal of Physical Chemistry C*, vol. 112, no. 11, pp. 4159–4167, 2008.

[94] O. Trejo, T. H. Cho, S. Sainio, and N. P. Dasgupta, "Xanes studies of zinc tin oxide films deposited by atomic layer deposition: Revealing process-structure relationships for amorphous oxide semiconductors," *The Journal of Physical Chemistry C*, vol. 127, no. 1, pp. 338–349, 2022.

[95] S. Jeon, S. Bang, S. Lee, S. Kwon, W. Jeong, H. Jeon, H. J. Chang, and H.-H. Park, "Structural and electrical properties of zno thin films deposited by atomic layer deposition at low temperatures," *Journal of the Electrochemical Society*, vol. 155, no. 10, p. H738, 2008.

[96] S. Vangelista, R. Mantovan, A. Lamperti, G. Tallarida, B. Kutrzeba-Kotowska, S. Spiga, and M. Fanciulli, "Low-temperature atomic layer deposition of mgo thin films on si," *Journal of Physics D: Applied Physics*, vol. 46, no. 48, p. 485304, 2013.

[97] M. Putkonen, T. Sajavaara, and L. Niinistö, "Enhanced growth rate in atomic layer epitaxy deposition of magnesium oxide thin films," *Journal of Materials Chemistry*, vol. 10, no. 8, pp. 1857–1861, 2000.

[98] R. Azzam, "Ellipsometry and polarized light; azzam, rma and bashara, nm, eds," 1977.

[99] J. I. Pankove, *Optical processes in semiconductors*. Courier Corporation, 1975.

[100] W. H. Bragg, "Ix. bakerian lecture.—x-rays and crystal structure," *Philosophical Transactions of the Royal Society of London. Series A, Containing Papers of a Mathematical or Physical Character*, vol. 215, no. 523-537, pp. 253–274, 1915.

[101] H. McMurdie, M. Morris, E. Evans, B. Paretzkin, W. Wong-Ng, L. Ettlinger, and C. Hubbart, "Zno reference for bragg peak position and net constants," *Powder Diffraction*, vol. 1, no. 2, p. 76, 1986.

[102] G. J. McCarthy and J. M. Welton, "X-ray diffraction data for sno2. an illustration of the new powder data evaluation methods," *Powder Diffraction*, vol. 4, no. 3, pp. 156–159, 1989.

[103] M. Björck and G. Andersson, "*GenX*: an extensible X-ray reflectivity refinement program utilizing differential evolution," *Journal of Applied Crystallography*, vol. 40, pp. 1174–1178, Dec 2007.

[104] B. Burton, D. Goldstein, and S. George, "Atomic layer deposition of mgo using bis (ethylcyclopentadienyl) magnesium and h2o," *The Journal of Physical Chemistry C*, vol. 113, no. 5, pp. 1939–1946, 2009.

[105] C. B. Carter and D. B. Williams, *Transmission electron microscopy: Diffraction, imaging, and spectrometry*. Springer, 2016.

[106] Z. Baji, Z. Labadi, Z. E. Horvath, G. Molnaér, J. Volk, I. Bársony, and P. Barna, "Nucleation and growth modes of ald zno," *Crystal growth & design*, vol. 12, no. 11, pp. 5615–5620, 2012.

[107] H. Wang and K. Fu, "Nucleation and growth of mgo atomic layer deposition: A real-time spectroscopic ellipsometry study," *Journal of Vac-*

uum Science & Technology A: Vacuum, Surfaces, and Films, vol. 31, no. 6, p. 06F101, 2013.

[108] J. T. Newberg, D. E. Starr, S. Yamamoto, S. Kaya, T. Kendelewicz, E. R. Mysak, S. Porsgaard, M. B. Salmeron, G. E. Brown Jr, A. Nilsson, *et al.*, "Autocatalytic surface hydroxylation of mgo (100) terrace sites observed under ambient conditions," *The Journal of Physical Chemistry C*, vol. 115, no. 26, pp. 12864–12872, 2011.

[109] J. T. Newberg, C. Goodwin, C. Arble, Y. Khalifa, J. A. Boscoboinik, and S. Rani, "Zno (1010) surface hydroxylation under ambient water vapor," *The Journal of Physical Chemistry B*, vol. 122, no. 2, pp. 472–478, 2018.

[110] A. R. Hutson, "Hall effect studies of doped zinc oxide single crystals," *Physical review*, vol. 108, no. 2, p. 222, 1957.

[111] C. F. Klingshirn, A. Waag, A. Hoffmann, and J. Geurts, *Zinc oxide: from fundamental properties towards novel applications*. Springer Science & Business Media, 2010.

[112] G. Greczynski and L. Hultman, "A step-by-step guide to perform x-ray photoelectron spectroscopy," *Journal of Applied Physics*, vol. 132, no. 1, 2022.

[113] X. Yan, M. Duvenhage, J. Wang, H. Swart, and J. Terblans, "Evaluation of sputtering induced surface roughness development of ni/cu multilayers thin films by time-of-flight secondary ion mass spectrometry depth profiling with different energies o2+ ion bombardment," *Thin Solid Films*, vol. 669, pp. 188–197, 2019.

[114] W. Lee, X. Chen, Q. Shao, S.-I. Baik, S. Kim, D. Seidman, M. Bedzyk, V. Dravid, J. B. Ketterson, J. Medvedeva, *et al.*, "Realizing the heteromorphic superlattice: Repeated heterolayers of amorphous insulator and polycrystalline semiconductor with minimal interface defects," *Advanced Materials*, vol. 35, no. 19, p. 2207927, 2023.

[115] W. Zhou, Y. Liu, Y. Yang, and P. Wu, "Band gap engineering of sno2 by epitaxial strain: experimental and theoretical investigations," *The Journal of Physical Chemistry C*, vol. 118, no. 12, pp. 6448–6453, 2014.

[116] M. N. Mullings, C. Hägglund, and S. F. Bent, "Tin oxide atomic layer deposition from tetrakis (dimethylamino) tin and water," *Journal of Vacuum Science & Technology A: Vacuum, Surfaces, and Films*, vol. 31, no. 6, p. 061503, 2013.

[117] F. Lu and Q. Liu, "Structure and optical band gap of inverse spinel zn 2 sno 4 epitaxial films," *Journal of Low Temperature Physics*, vol. 200, pp. 142–151, 2020.

[118] H. Zhu, J. Liu, R. Chen, B. Feng, C. Luan, J. Ma, and H. Xiao, "High-quality and single-crystal znsno3 thin films: Fabrication and properties," *Vacuum*, vol. 197, p. 110811, 2022.

[119] H. H. Sønsteby, A. Yanguas-Gil, and J. W. Elam, "Consistency and reproducibility in atomic layer deposition," *Journal of Vacuum Science & Technology A*, vol. 38, no. 2, 2020.